Australian Government
Bureau of Meteorology

The Centre for Australian Weather and Climate Research
A partnership between CSIRO and the Bureau of Meteorology

CSIRO

The Pasha Bulker east coast low of 8 June 2007

Graham A. Mills, Rob Webb, Noel E. Davidson, Jeffrey Kepert, Alan Seed, and Deborah Abbs

CAWCR Technical Report No. 023

June 2010

www.cawcr.gov.au

The Pasha Bulker east coast low of 8 June 2007

Graham A. Mills[1], Rob Webb[2], Noel E. Davidson[1], Jeffrey Kepert[1],
Alan Seed[1], and Deborah Abbs[1]

[1]*Centre for Australian Weather and Climate Research*

[2]*NSW Regional Forecast Centre, Bureau of Meteorology*

CAWCR Technical Report No. 023

June 2010

ISSN: 1835-9884

National Library of Australia Cataloguing-in-Publication entry

Title: The Pasha Bulker east coast low of 8 June 2007 / Graham A. Mills ... [et al.].

ISBN: 978-1-921605-77-2 (pdf)

Series: CAWCR technical report; No. 23

Notes: Included bibliography references and index.

Subjects: Meteorology--Research. Climatic changes--Research.

Other Authors/Contributors: Mills, G. A. (Graham Alan), 1946-

Dewey Number: 551.50994

Enquiries should be addressed to:
Graham Mills
Centre for Australian Weather & Climate Research
GPO Box 1289 Melbourne
Victoria 3001, Australia

g.mill@bom.gov.au

Copyright and Disclaimer

CONTENTS

LIST OF FIGURES

ABSTRACT

On the night of 7-8 June 2007 an intense extra-tropical low pressure system caused havoc on the central New South Wales (NSW) coastline near Newcastle. While the storm was well-predicted by medium range global forecast models some days in advance, and the NSW Regional Forecast Centre of the Australian Bureau of Meteorology issued emphatic press releases warning of the impending storm, a number of challenging forecast issues emerged. These included estimating the location along the coast, and the intensity, of the region of maximum winds and rainfall and how these related to the position of the developing low, the reasons for the modulation of rainfall rates and patterns that occurred on quite short time-scales and which thus posed significant challenges in flood warnings, and the wave-structures seen in the radar echoes that also seemed related to changes in rainfall intensity. One of these waves crossed the coastline close to Newcastle as a small low-pressure system with an eye-like structure evident in radar imagery.

The atmospheric dynamics that led to these forecast challenges are described and explained at scales from global down to fine mesoscale using observations, satellite and radar remote sensing, and a range of numerical weather prediction model data.

1 INTRODUCTION

On the night of 7-8 June 2007 an intense extra-tropical low pressure system caused havoc on the central New South Wales (NSW) coastline near Newcastle (32.93ºS, 151.79º E). (Figure 1 shows the location of places referred to in this document.) Some of the adverse impacts of this low were:

- Nine deaths.
- The Pasha Bulker bulk coal carrier grounded on the Newcastle beach.
- Major flash flooding, with rainfall of 466 mm at Mangrove Mountain, and over 350 mm in the suburbs of Newcastle over a 36-hour period.
- Mean winds on the coast exceeded 45 knots with gusts over 55 knots for most of an 18-hour period, with the peak recorded mean wind and gust speeds greater than 60 and 70 knots respectively.
- Massive seas caused major coastal erosion. At the Sydney wave-rider buoy (33.8S 151.4E) significant/maximum wave heights of 6.4/14.1 m were recorded.
- Over $1.5b in damage costs.

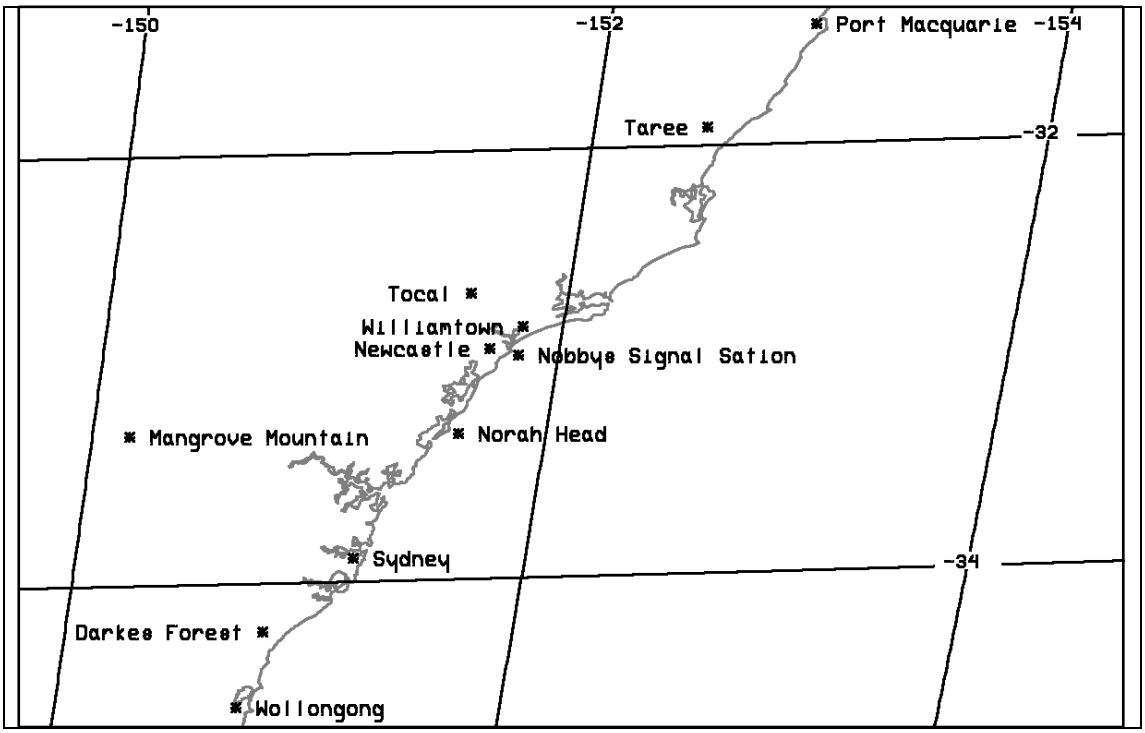

Fig. 1 Locality diagram.

East coast lows cause major socioeconomic damage, due to their rapid development and the intense winds, heavy rainfall, and high seas they generate. They have been associated with a number of shipping disasters from as early as 1857 (the loss of the Dunbar with over 120 lives),

through the famous "Sygna storm" of 1974, to the grounding of the bulk coal carrier, the Pasha Bulker, in June 2007. Significant coastal erosion, hazard to recreational and commercial boating, and flooding and wind damage in coastal towns are also major effects of these systems. Their impact is not purely negative, though, as many of the major inflows to metropolitan water storages are associated with the rainfall from east coast lows.

While the 8 June storm was well-predicted by medium range global forecast models some days in advance, and the NSW Regional Forecast Centre (RFC) of the Australian Bureau of Meteorology (the Bureau) issued emphatic press releases warning of the impending storm, a number of challenging forecast issues emerged. These included estimating the location along the coast and the intensity of the region of maximum winds and rainfall, how these related to the centre of the developing low, the reasons for the modulation of rainfall rates and patterns that occurred on quite short time-scales and which thus posed significant challenges in flood warnings, and the wave-structures seen in the radar echoes that also seemed related to changes in rainfall intensity. One of these waves culminated in an eye-like structure in the radar imagery as a small low-pressure system crossed the coastline close to Newcastle between 1500 and 1530 UTC 8 June 2007.

A workshop was organised in the NSW Regional Office of the Bureau in August 2008 to discuss these and broader issues associated with the forecasting of, and the weather associated with, east coast lows. At that meeting many aspects of the event were discussed, including those listed in the previous paragraph. As many of these features had not previously been documented, and their relationship to previously published studies of east coast lows was unclear, this report attempts to redress some of these issues, and to indicate further directions for research.

We first describe in the broadest terms the weather experienced on the central coast of NSW on 8 June 2007, and briefly describe some of the features that will be discussed in greater detail in this report. We then describe the larger-scale long-wave patterns that led up to the surface low development on 7-8 June 2007, and compare this upper-tropospheric sequence with that occurring during a number of other damaging east coast low events. This is followed by a closer look at the relationship between the developing upper-tropospheric cut-off low over eastern Australia and the development of the surface low, using a combination of Isentropic Potential Vorticity (IPV) analyses and geostationary satellite 6.7μm "water vapour channel" (WV) imagery. Then, decreasing in scale and using satellite data, radar data, and mesoscale NWP fields the relationships between synoptic-scale forcing and the upper-and lower tropospheric thermal anomalies that lead to the asymmetric wind structure around the low, the varying rain rates observed during the night of 8-9 June, and the wave structures seen in the radar echoes will be described.

2 DATA SETS USED

Observations from the Bureau's Automatic Weather Station (AWS) network, satellite and radar imagery saved in real time by the NSW RFC, and MSLP analyses from the Bureau's National Meteorological and Oceanographic Centre (NMOC) are used to provide the overview of the meteorology of the day. A variety of sources of rainfall observations were used, including gridded analyses from the Bureau's National Climate Centre, AWS station rainfall observations, and data provided by Hunter Water from their rainfall observing network over Newcastle.

Diagnostic descriptions are based on a range of NWP products. For the large-scale synoptic evolution the 6-hourly operational LAPS (Puri et al. 1998) analyses, and for events prior to 2000 the ERA40 reanalysis data sets (Kallberg et al. 2005) are used. As the scales being diagnosed become smaller and more focussed, and to benefit from their temporal consistency, mesoscale NWP simulations are used. Operational meso-LAPS 0.125^o latitude/longitude grid simulations are used to bridge the gap between the synoptic-scale analyses and the smaller-scale structures, but two special after-the event mesoscale simulations were prepared for this study to examine the smaller spatial and temporal scale fluctuations in the low's structure, and these are used extensively in the diagnostic analyses later in this report.

The first of these is a 0.05^o grid meso-LAPS based simulation, configured over a much larger (45^o-25^{o}S, 142^o-162^{o}E) grid than the operational Sydney region 0.05^o meso-LAPS model, and which included a sophisticated initialisation phase designed for tropical cyclone studies. In the first phase of the initialisation objective analyses are generated each six hours during the 24 hours prior to the base time of the simulation using observations from the standard observing network. Background error covariances and observational errors are tuned for the high-resolution analysis. From 24 hours prior to the base time of the simulation, the forecast model is run and weakly nudged towards the 6-hourly analyses. During the 24 hours of nudging initialization the model develops consistent boundary layer, vertical motion, and secondary circulation structures, and the mass-wind balance evolves to the model's dynamics. During this period infrared satellite cloud imagery is used to define the cloud distribution, and the effects of these clouds are incorporated by the imposition of convective heating profiles at those locations where deep convection is observed by the satellite. The insertion of these heating profiles causes the model to generate upward motion and adiabatic cooling to offset the imposed heating. In this way the vertical motion field is re-defined to be consistent with the satellite imagery (Davidson and Weber 2000). After initialization, the modelled mesoscale systems are (a) embedded in a large-scale environment obtained from data assimilation procedures, (b) have primary circulations defined by high-resolution data assimilation techniques, (c) have secondary circulations and boundary layer structure defined from the model dynamics and physics, (d) contain a vertical motion field consistent with the satellite-observed distribution of deep convection at the initial time of the simulation, and (e) are in mass-wind balance defined by the model's dynamics and physics.

The second hindcast prepared is a multiply-nested RAMS (Cotton et al. 1988) non-hydrostatic model simulation with a set of two-way nested grids of 12, 3, and 1 km. This simulation was initialised from, and its outer mesh nested within, a 0.1^o grid MA-LAPS (Vincent et al. 2008) after-the-event data assimilation and forecast of the event, and this RAMS simulation was used to support hypotheses developed based on the 0.05^o meso-LAPS hindcast.

3 SYNOPTIC AND WEATHER OVERVIEW

Figure 2 shows a 12-hourly sequence of synoptic-scale MSLP analyses from 0000 UTC 6 to 1200 UTC 9 June 2007. At the first time (Fig. 2a), there is a large, intense anticyclone in the Bight, with a ridge into the Tasman Sea. An incipient trough extends from just off the Queensland coast (the 1014 hPa low marked in the analysis) southwestwards into central NSW. This trough slowly deepens through the 36 hours to 1200 UTC 7 June (Fig. 2d), with at least two low centres being analysed offshore, and another implicit over northern NSW. The low

centre off the northern NSW coast moves slowly southwards and deepens by some 10 hPa over the next 24 hours (Figs 2e,f), and with the development of a ridge of high pressure to its south a very strong pressure gradient has developed on its southern flank. The low remained close to the central NSW coast through the next 12 hours (although as will be shown later, with considerable mesoscale structure), before moving southeastwards into the Tasman Sea between 0000 and 1200 UTC on 9 June (Figs 2g,h).

The large-scale Australian Water Availability Project (AWAP, Jones et al. 2009) rainfall analysis for the three days to 0900 EST 9 June 2007 shows (Fig. 3) rainfall extending along almost the entire east coast of Australia, but the most intense area is in a narrow (on a continental scale) band extending inland from near Newcastle, with maximum (grid-average) values above 300 mm near the coast.

Meteograms of AWS observations from Nobbys Head Signal Station at Newcastle, Mangrove Mountain, Williamtown, and Norah Head are shown in Figs 4 and 5. First focussing on observations from Nobbys Head Signal Station (Fig. 4a-c) southeasterly winds increased to reach some 40-45 knots overnight on 7 through to the morning of the 8 June, before shifting westerly and weakening around 1300 EST. Around 1900 EST the wind shifted back to the southeast and increased, with mean speeds exceeding 50 knots, and the highest gust of 67 knots was recorded around 0130 EST on 9 June, albeit with some significant fluctuations. Immediately following this time there was an abrupt wind shift through north to the west, and speeds dropped markedly, although there were further wind shifts to gale force southeasterlies, and back to the west with decreased speeds during the afternoon of 9 and early morning of 10 June. Notably, and to be discussed further in subsequent sections of this report, speeds at stations north of Williamtown (e.g. Tocal, Taree, Port Macquarie) were substantially lower. The accumulated rainfall time series (Fig. 4c) shows an abrupt increase in rain-rate at around 1530 EST, with nearly 60 mm accumulating in the next hour. There was then a lessening of the rain-rate until a little after 1800 EST, after which there was another rapid increase with a further 61 mm accumulating until 1930 EST, another short respite, a short surge, and then after 2045 EST a marked lowering of the rain-rate. By midnight the rainfall had essentially ceased at this station.

The meteograms at Mangrove Mountain (Figs 4d-f), Williamtown (Figs 5a-d), and Norah Head (Figs 5e-h), show not dissimilar evolutions, although with time variations due to their displacement north or south of Nobbys Head, and with the slightly more inland stations having lower wind speeds than the exposed coastal stations of Nobbys Head and Norah Head. Williamtown's pressure trace (Fig. 5d) shows considerable fluctuation between 0900 and 2100 EST on 8 June, with several sharp drops of around 3 hPa, but the abrupt drop of some 8 hPa between 2230 and 0100 EST, and a recovery nearly as rapid, is quite spectacular. Similar pressure fluctuations were also recorded at Norah Head (Fig. 5h).

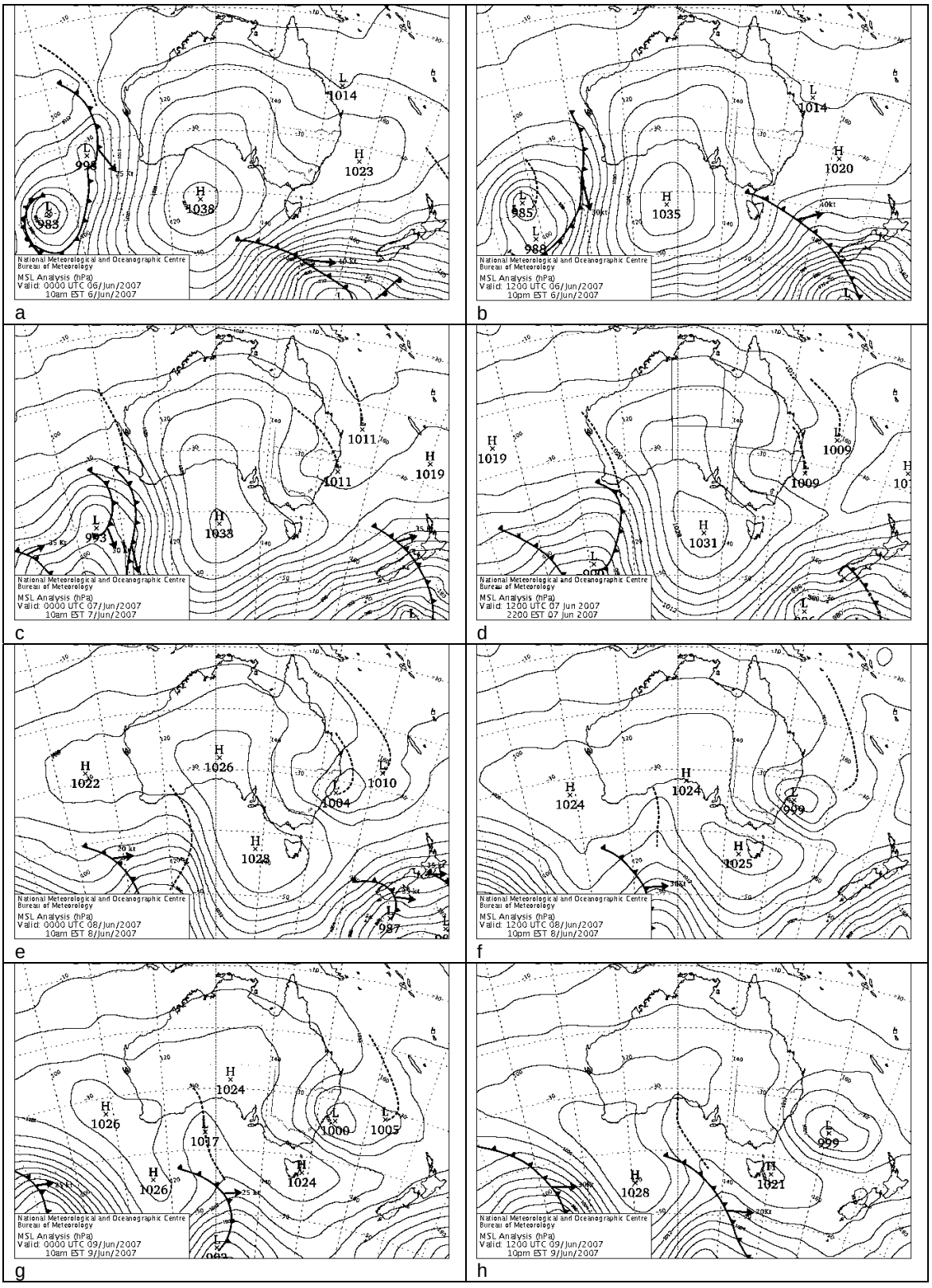

Fig. 2 MSLP analyses from the National Meteorological and Oceanographic Centre at 12-hour intervals from 0000 UTC 6 June 2007 (a) to 1200 UTC 9 June 2007 (h).

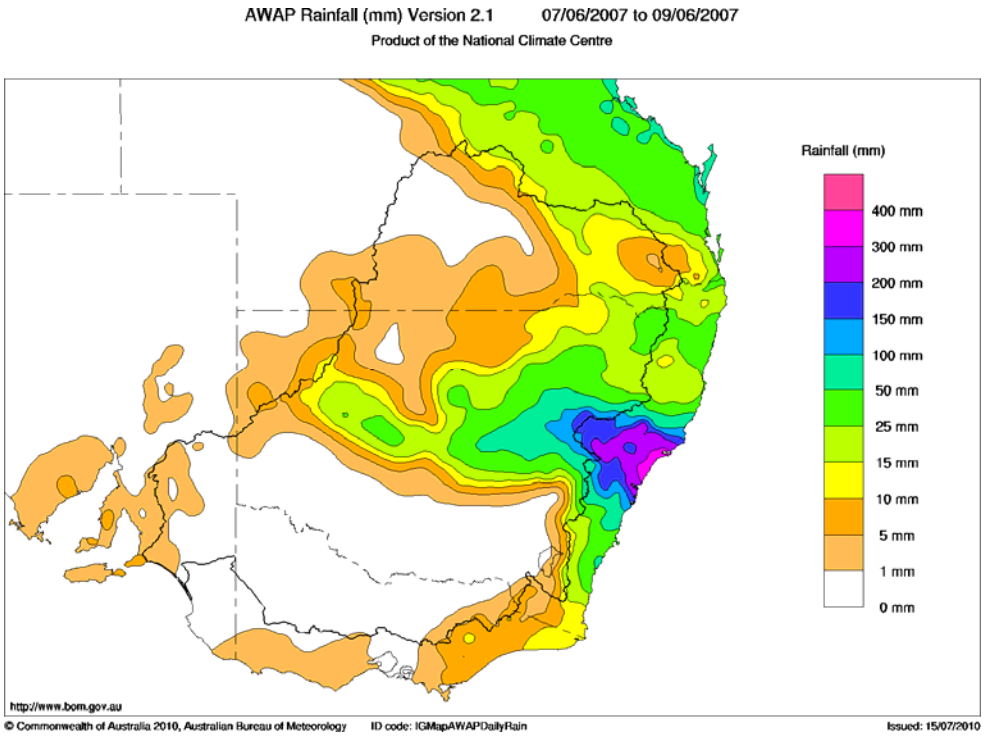

Fig. 3 Three-day rainfall to 0900 EST 9 June 2007 from the Australian Water Availability Project rainfall analyses.

The spatial distribution of rainfall over the immediate Newcastle area (Fig. 6) shows a narrow tongue of rainfall over 350 mm in the 24-hour period from midnight to midnight on 8 June, with a much wider area receiving more than 150 mm. The hourly totals for a number of the stations used in constructing these isohyets are presented in Fig. 7, and show that at most of these stations the rainfall rate increased abruptly around 1600 EST, and declined again after 2100 EST.

Three-hourly sequences of Infra-Red (IR) and WV satellite imagery from 2330 UTC 7 June are shown in Fig. 8. The key features at the first two times (Figs 8a-d) are first, a broad area of cloud aligned WNW/ESE through NSW and across the coast, seen in both the IR and the WV images, and second, a very marked dry slot extending from the northwest in the WV imagery. Important is the band of convective clouds (arrowed) at 0230 UTC that appear to be forming at the southern edge of the driest air in the WV imagery. This band of convective cloud moved southward and developed rapidly, and by 0830 UTC had essentially merged with the southern cloud band to form the dominant cloud feature, which had become significantly more convective in character. This is the period of the two major rainfall accumulations recorded at Nobbys Head (Fig. 4c). After around 1200 UTC the convective nature of the cloud over the central NSW coastline weakened, and the cloud mass and became more stratiform in appearance, coinciding with the weakening of the rainfall rates seen in Figs 4 and 5. From 1130 to 2030 UTC the cloud band rotates cyclonically, and particularly on its northern edge shows distinct waves, seen clearly in the WV imagery.

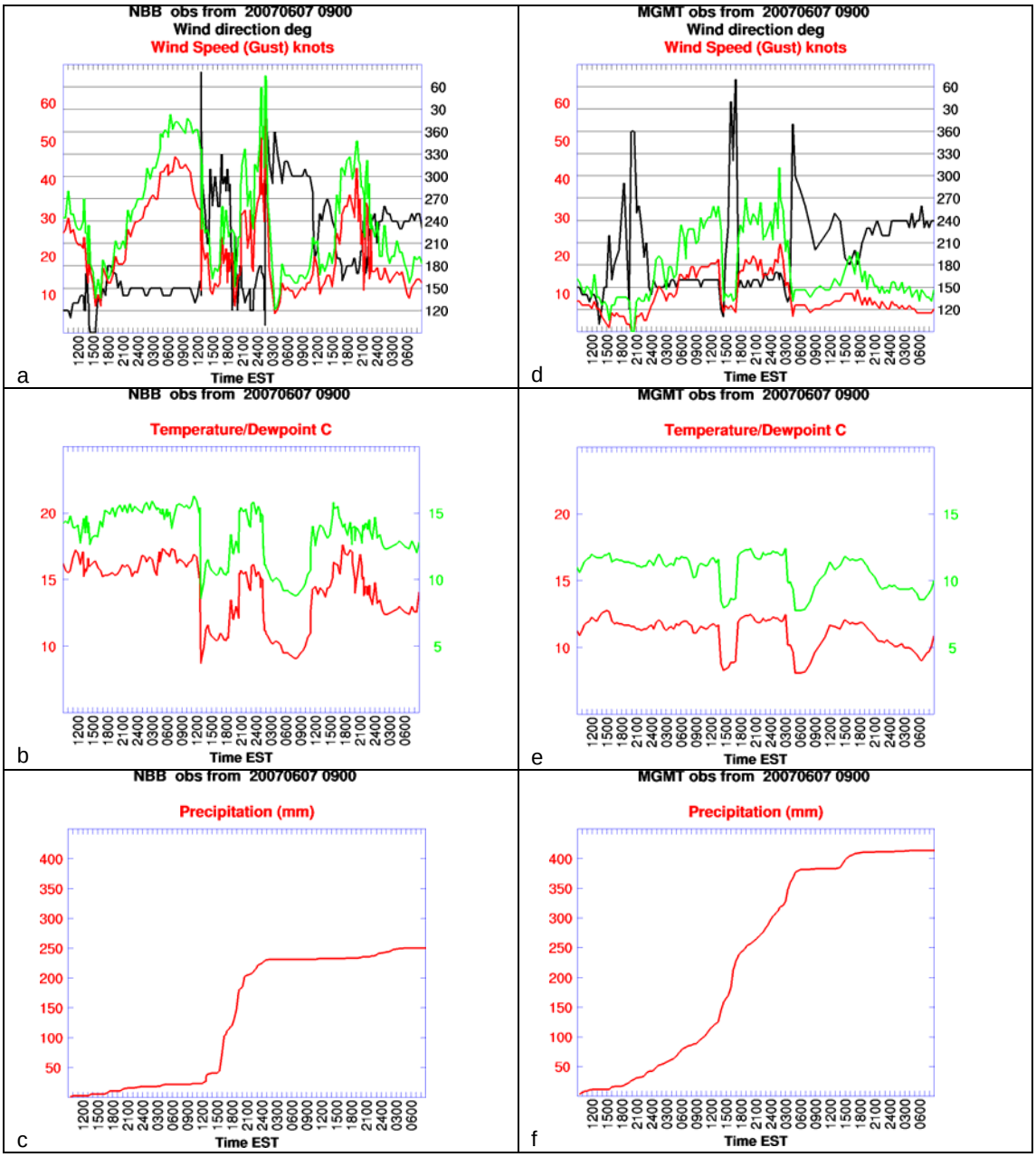

Fig. 4 Seventy-two hour meteograms starting at 0900 EST 7 June 2007 from Nobbys Head Signal Station (left) and Mangrove Mountain (right). Upper panels are wind direction (black), and mean (red) and gust (green) wind speed. Middle panels show temperature (red) and dewpoint (green), while the lower panels show accumulated precipitation.

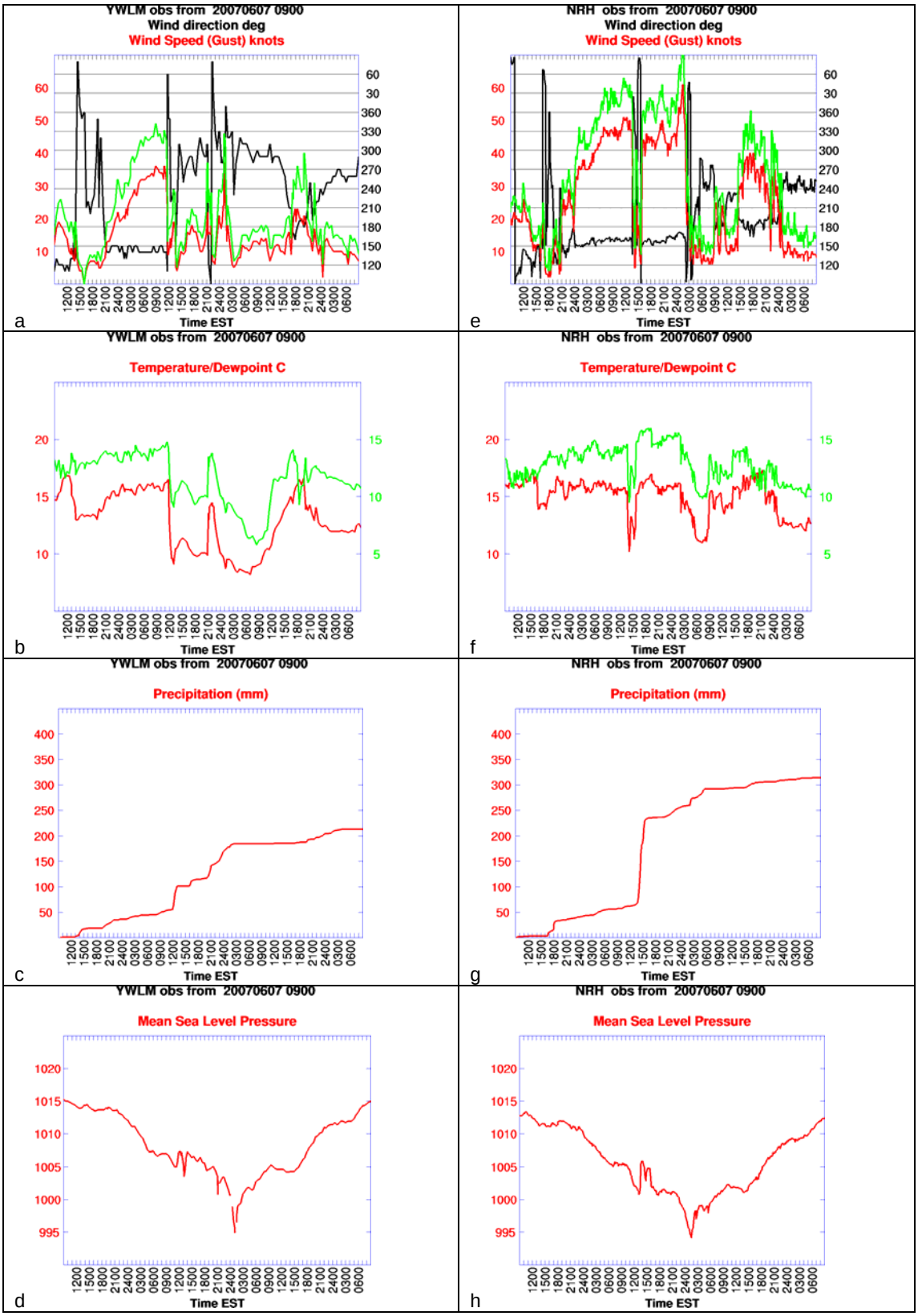

Fig. 5 Seventy-two hour meteograms starting at 0900 EST 7 June 2007 from Williamtown (left) and Norah Head (right). Upper panels are wind direction (black), and mean (red) and gust (green) wind speed. Second row: temperature (red) and dewpoint (green). The third row shows accumulated precipitation while the lower panels show the MSLP time series.

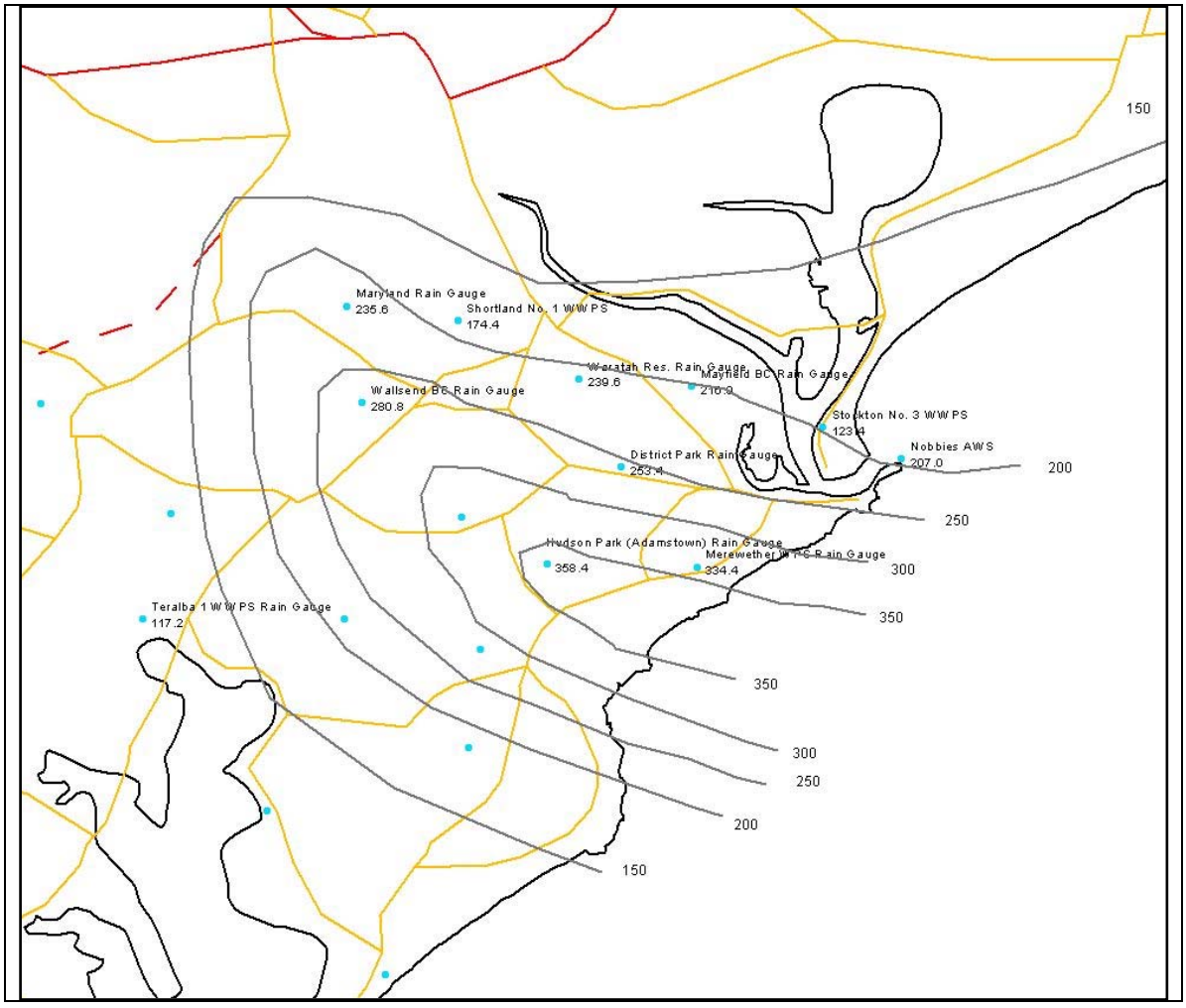

Fig. 6 Isohyets of 24-hour rainfall from midnight 7 to midnight 8 June 2007 from the Hunter Water rain gauge network over Newcastle.

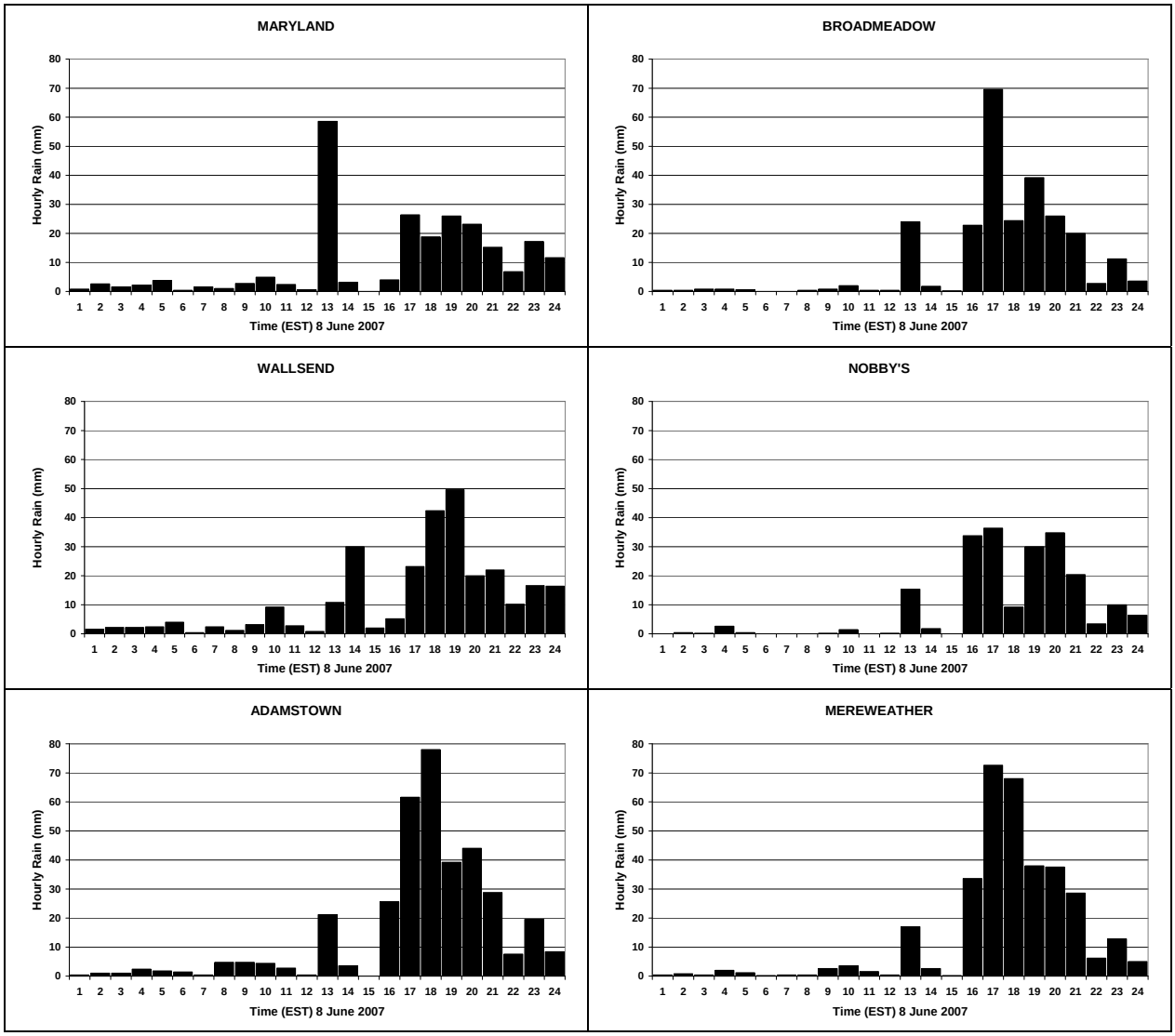

Fig. 7 Histograms of hourly rainfall (mm) at 6 stations used to construct the isohyets in Fig. 6 for hourly accumulations to the hour (EST) shown in the abscissa.

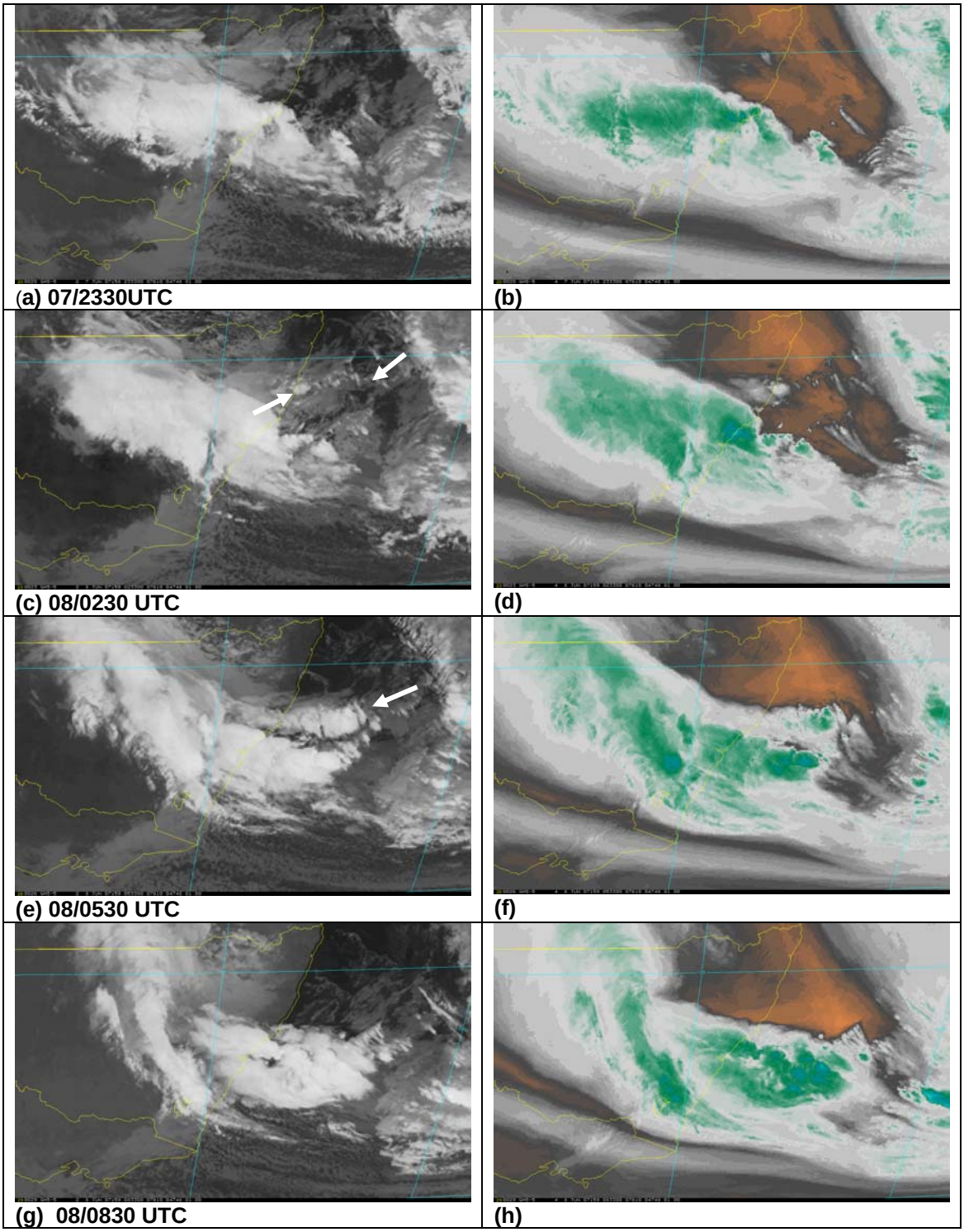

Fig. 8 Infra-red (left) and Water-Vapour imagery at 3-hourly intervals from 2330 UTC 7 June to 0830 UTC 8 June 2007.

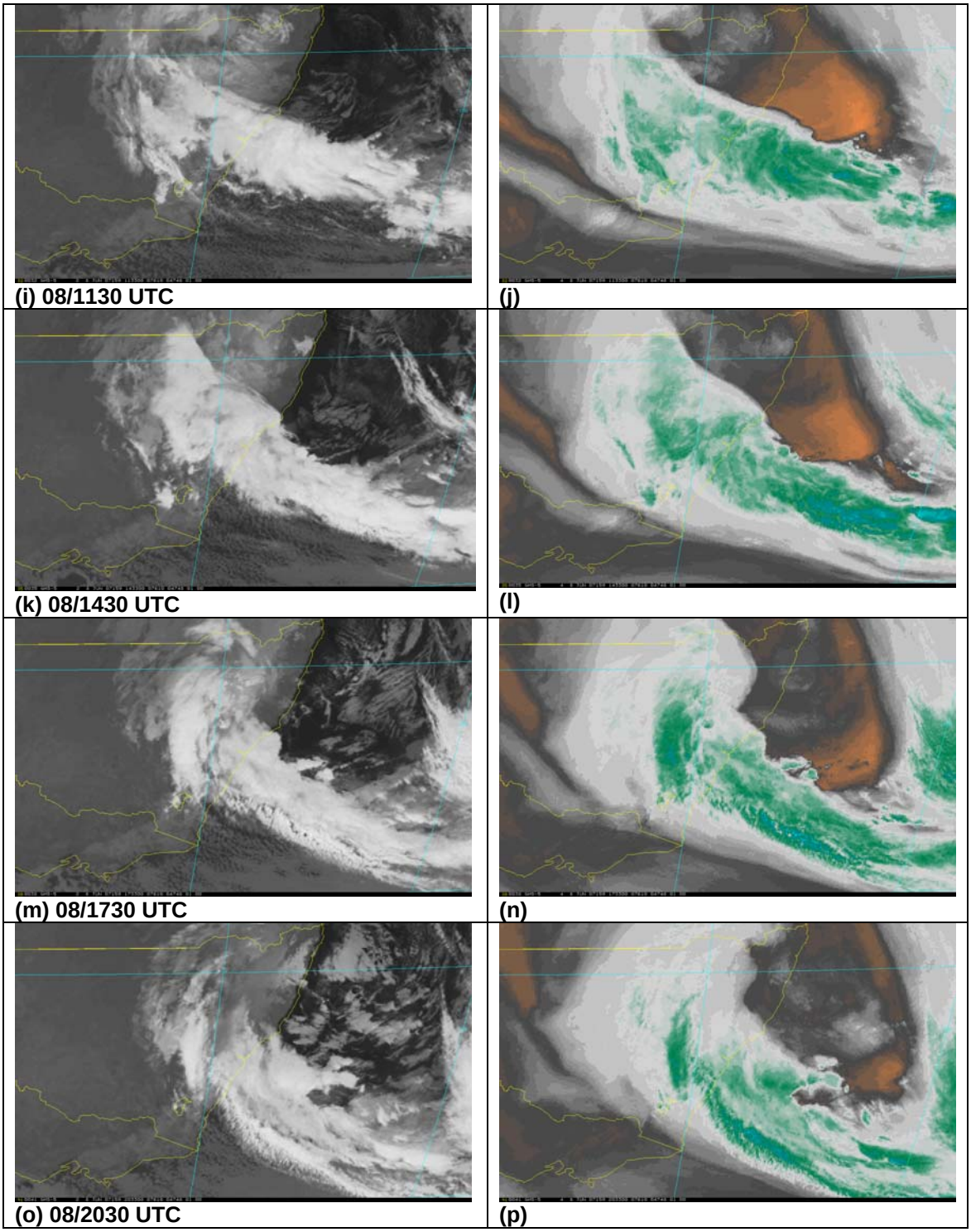

Fig 8 (cont). Infra-red (left) and Water-Vapour imagery at 3-hourly intervals from 1130 UTC to 2030 UTC 8 June 2007.

Figure 9 shows the radar imagery at 1-hour intervals from 0530 UTC through 1630 UTC. In the first period (Figs 9a,b) there is a cluster of convection aligned along the coast, but by 0730 UTC (Fig. 9c) the convection is aligned rather more east-west, and when these images are looped at 10 min intervals appear to show cells moving along the line of convection and impacting the same region of the coastline. The change from scattered to linear convection occurs with the

arrival of the convective cloud feature from the north (seen in the satellite imagery in Fig. 8), and also with the first period of intense rain at Nobbys Head, while the second period of heavy rain at Nobbys Head coincides with the westward movement of cells along the line of convection. From 0930 UTC (Fig. 9e) the relatively straight band of intense convection shows a tendency to develop waves, or arcs of convection, with cusps in between, and after 1030 UTC (Fig. 9f) the intense convection weakens and the rainfall appears to be more stratiform in nature. This period coincides with the decrease in rainfall rate in the Nobbys Head pluviogram (Fig. 4c), with the change in cloud morphology seen in the satellite images, and also with the commencement of rotation of orientation of the cloud band. Finally, at 1130 UTC, and more clearly at 1230 UTC (Figs 9g,h) an apparent vortex can be seen some 130 km southeast of the radar, and this moves northwestwards and crosses the coast as an "eye-like" feature close to 1500 UTC (Figs 9j,k). Note the minimum surface pressure at Williamtown was reported at 1510 UTC (Fig. 5d).

Several of the features in the meteograms (Figs 4,5) appear to correspond to some of these remotely sensed patterns of radar reflectivity or satellite imagery. However, in real time the problem is to anticipate how these remotely sensed patterns are likely to be manifest at particular locations so that appropriate warnings can be issued. The remainder of this report studies the evolution of the atmospheric dynamics and kinematics that drove the development of this low, and on the mesoscale structures that led to the majority of the significant (negative) impacts of the storm. The intention is to increase the understanding of the relationships between the remotely sensed features and the NWP model predictions, to provide conceptual models that might be applied in future forecasting practice, and to indicate fruitful areas of future research.

The primary diagnostic tools used are regional and mesoscale NWP data, since these provide dynamically and temporally consistent data sets that are amenable to diagnosis. We will commence by describing the large scale environments within which the low developed, and then steadily focus closer on the central NSW coast, using progressively finer-scale NWP models as we approach the scale of the mesoscale weather features seen in the satellite and radar data in Figs 8 and 9.

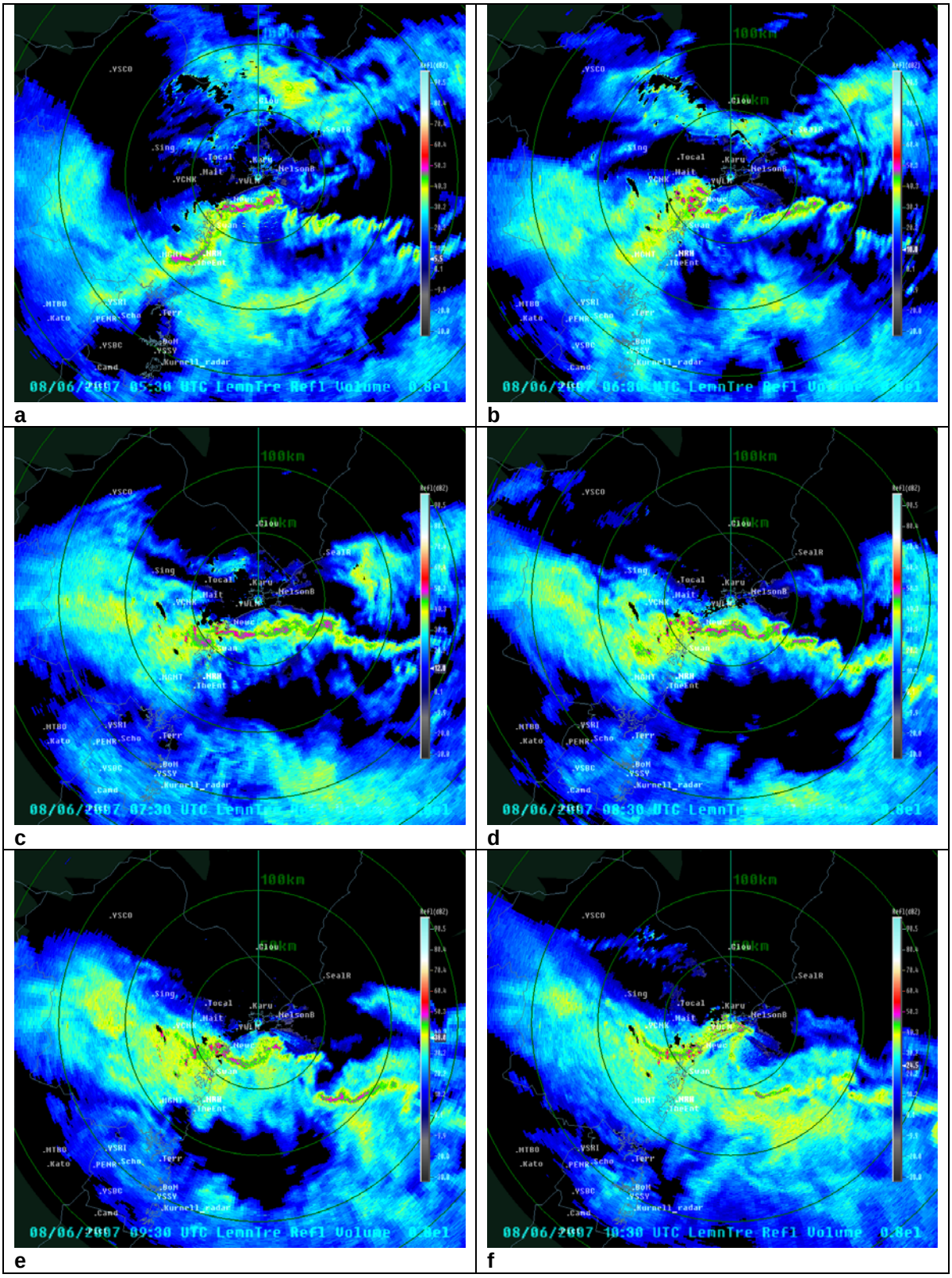

Fig. 9 a-f. Newcastle radar imagery at hourly intervals from 0530 to 1030 UTC 8 June 2007.

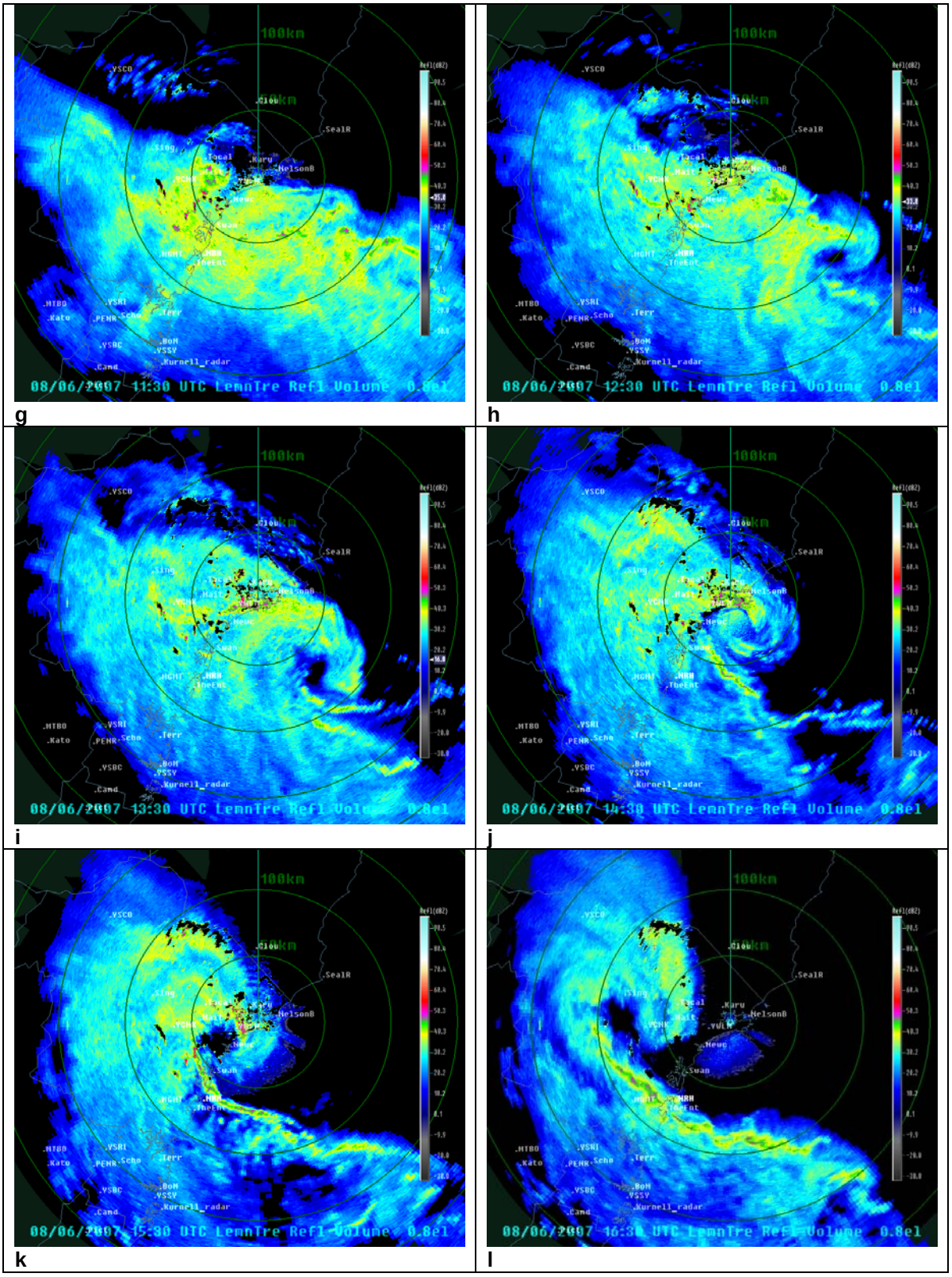

Fig. 9 g-l. Newcastle radar imagery at hourly intervals from 1130 to 1630 UTC 8 June 2007.

4 LARGE-SCALE UPPER TROUGH/RIDGE PATTERNS

4.1 The Pasha Bulker Storm

All conceptual and synoptic models of extra-tropical cyclogenesis link surface low development to upper wave/jet structures via baroclinic instability arguments (e.g. Shapiro and Gronas 1999). It was particularly evident in medium-range global NWP forecasts leading up to the event that a major upper-tropospheric cut-off low was forecast to form over eastern Australia prior to the development of the Pasha Bulker east coast low. Figure 10 shows the 300 hPa geopotential and wind speed patterns at 2-day intervals leading up to the 12 hours during which the most rapid surface cyclogenesis occurred. At the first time there is a major trough through the Indian Ocean, a ridge south of Australia, and a trough oriented almost east-west over Victoria and the South Australian coastline. In the subsequent two panels a classic Rossby wave downstream amplification process is seen. First the ridge south of Australia amplifies, and then the trough over southeastern Australia extends equatorward, cuts off, and becomes less positively tilted with a strong northwesterly jet on its eastern side – a classic cyclogenesis pattern (Bell and Keyser 1993).

We now focus on the development of the upper-tropospheric cut-off low over southeastern Australia, and how its evolving structure leads to the explosive surface development. In this discussion, a series of chart-sets will be presented, first at 24-hour intervals from 0000 UTC 6 June till 0000 UTC 8 June, and then at 6-hourly intervals through 0000 UTC 9 June. Using the LAPS analyses, Figs 11a-g show for each of these times, a MSLP/near surface wind plot, a 400 hPa wind/IPV plot, a 300 hPa wind/IPV plot with overlain WV imagery from the MTSAT geostationary satellite, and a cross-section to show some aspects of the vertical structure of the developing system. The IPV advection concepts of Hoskins et al. (1985) are used to provide a conceptual model by which the cyclogenesis is discussed, and in order to highlight the areas of strongest forcing, the pseudo-potential vorticity form of the forcing function in the quasi-geosptrophic (q-g) height tendency equation (Bluestein, 1992, pp372-373) is computed and areas of larger height-fall forcing (hereafter q-g forcing) are shaded on the 400 hPa IPV/wind plots. The strength of the pseudo-potential vorticity is that its variation on pressure surfaces is similar to the variation of IPV on isentropic surfaces (Bluestein 1992, Hoskins et al. 1985). The WV imagery is used to provide some qualitative corroboration of the IPV patterns (see Weldon and Holmes 1991, Mansfield 1997).

At the initial time, 0000 UTC 6 June 2007, an easterly dip is present at the surface over central Queensland and NSW (Fig. 11a). In the upper troposphere there is a broad, moderately cyclonically curved jet across the northern half of Australia, an impressive anticyclone south of the Bight, and a cut-off low, with a southeasterly jet streak on its western flank, near the South Australia (SA)/NSW border. There is an elliptical IPV maximum associated with the cut-off low, seen in the cross-section as a marked cold core in the lower troposphere and tropopause depression in the upper troposphere. A second elongated IPV maximum lies on the cyclonic side of the major jet stream through Western Australia and into SA. The correspondence between the dark areas in the WV imagery and the 300 hPa IPV pattern is very striking, with marked dark bands and elongated IPV patterns associated with the cyclonic shear sides of the jet streams. Interestingly, the cross-section shows the tropopause fold to be more marked on the southwest than the northeast side of the cut-off low. At this time there is little focussed q-g height fall forcing, but the scattering of small centres over Queensland (Qld) and northern

NSW, largely on the anticyclonic side of the northwesterly jet, are consistent with the area of the surface pressure trough in that region. Hopkins (1997) also noted that in the early stages of the August 1990 east coast low event one of the low centres was on the anticyclonic side of the jet stream.

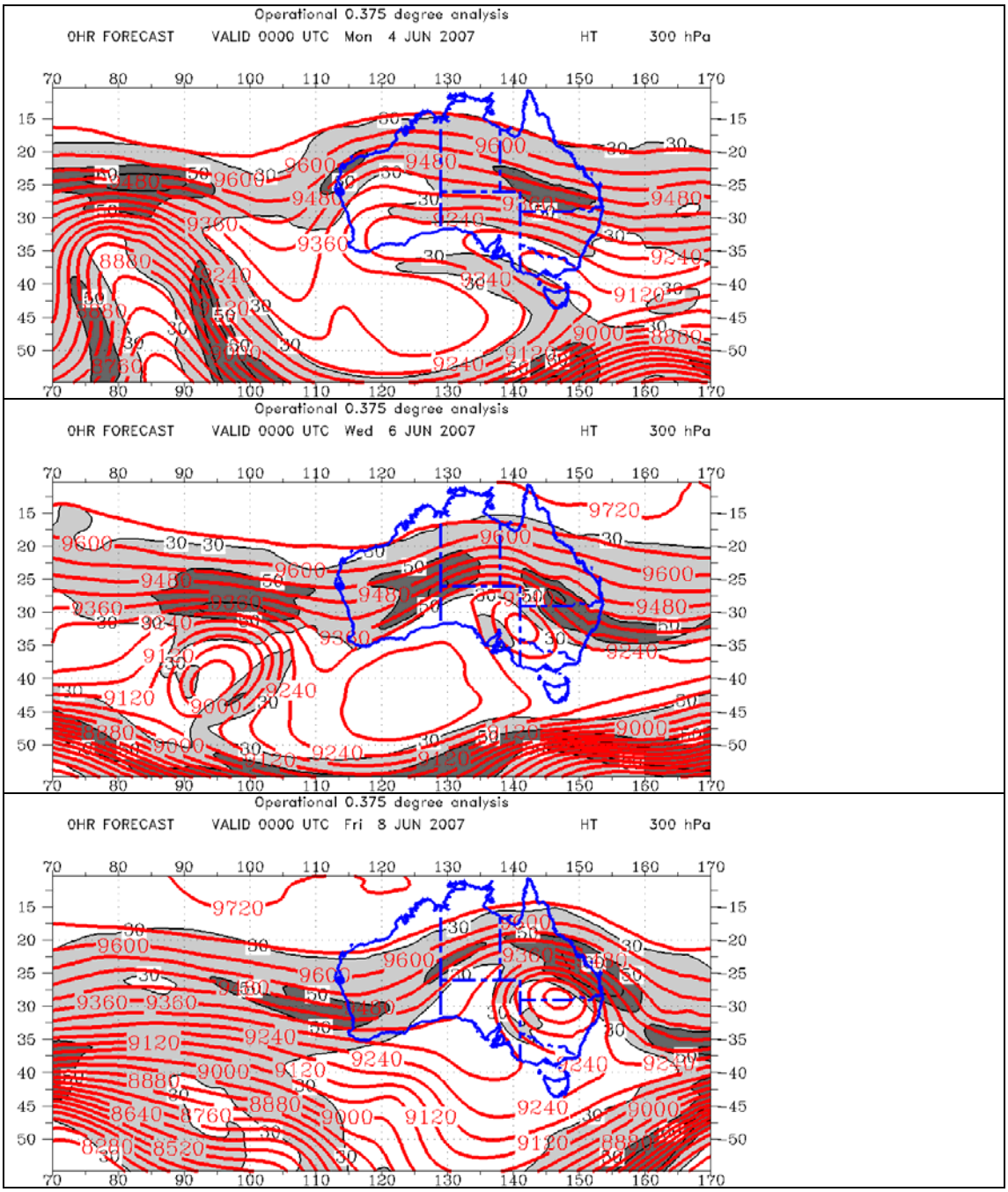

Fig. 10 LAPS 300 hPa geopotential height/wind speed analyses at 48-hour intervals leading up to the development of the east coast low on 8 June 2007. Isotachs have light shading between 30 and 50 m s^{-1}, and darker shading for speeds greater than 50 m s^{-1}.

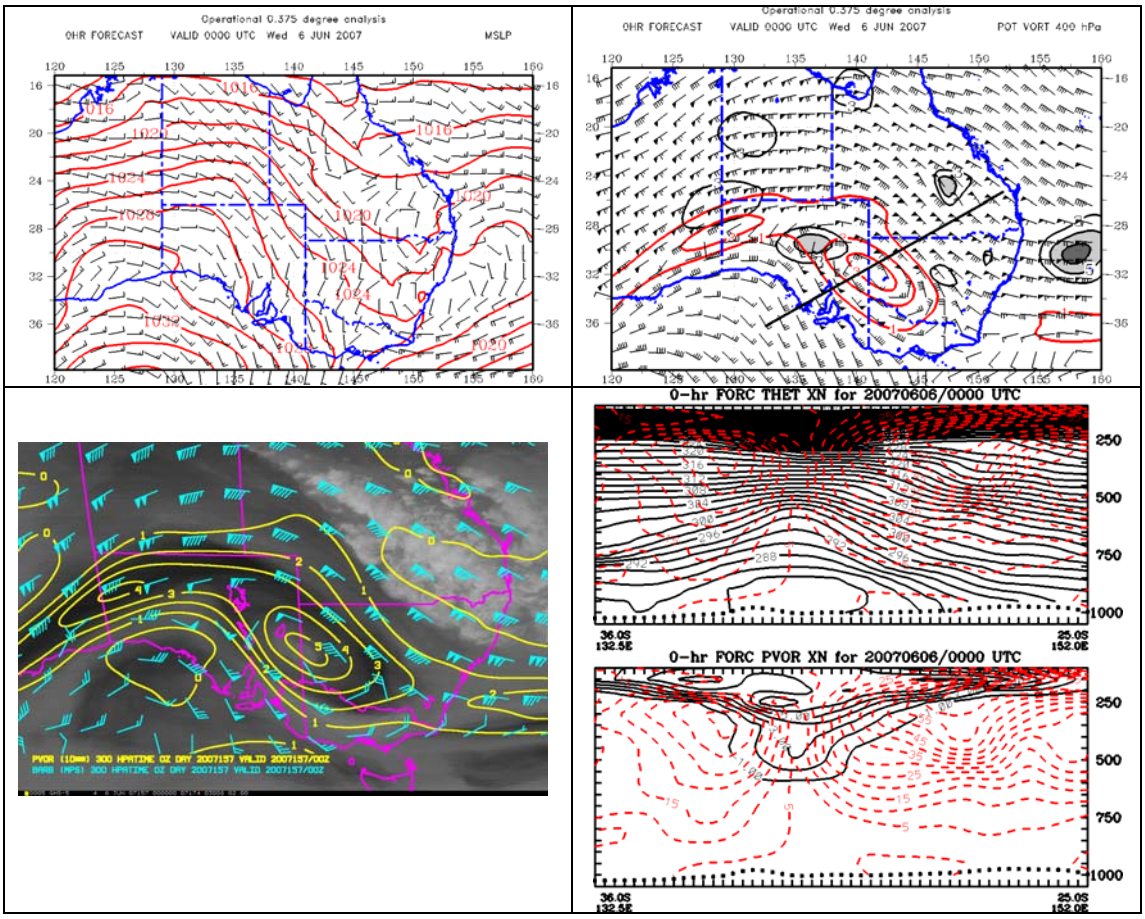

Fig. 11a LAPS analysis fields valid at 0000 UTC 6 June 2007. Top left shows the MSLP field with near-surface wind barbs overlaid. Top right panel shows (contoured) 400 hPa IPV with the 400 hPa wind barbs overlaid. The shaded regions indicate the magnitude of the 400 hPa pseudo-potential vorticity forcing term in the quasi-geostrophic height tendency equation (s^{-3} x 10^{-12}). The lower left panel shows the 300 hPa IPV field and 300 wind barbs overlaid on the satellite Water Vapour Channel imagery. The lower right panel shows cross-sections along the line shown in the upper-right panel: the upper cross section shows potential temperature (black, K) and wind speed (red, m s^{-1}), while the lower section shows IPV (black) and wind speed (red, m s^{-1}). All IPV values have the negative sign omitted.

Twenty-four hours later, at 0000 UTC 7 June 2007 (Fig. 11b), the upper-tropospheric flow had become considerably more meridional, the centre of the cut-off low had moved northwards to be over the western end of the Queensland/NSW border, and there is a complex pattern of IPV filaments associated with the jet streaks moving around the main IPV (cut-off low) centre . At 400 hPa there is a distinctly separate IPV lobe east of the main centre and over northeast NSW, while the filaments west of the low centre are more clearly seen in the 300 hPa pattern. All these features have corresponding dark (dry) bands in the WV imagery, lending credibility to these structures. A deep tropopause fold (see cross-section) has developed on the northeastern side of the cut-off low, with the 1 IPV unit contour descending to below 600 hPa. The formation of a surface low off the northern NSW coastline appears associated with the forcing of height falls over the coast near the Qld/NSW border, while another, focussed forcing of height falls inland from the northern NSW ranges appears associated with the development of a short-wavelength surface pressure trough connected to the offshore low at this time. Higher resolution analysis may well show a distinct low centre in this region.

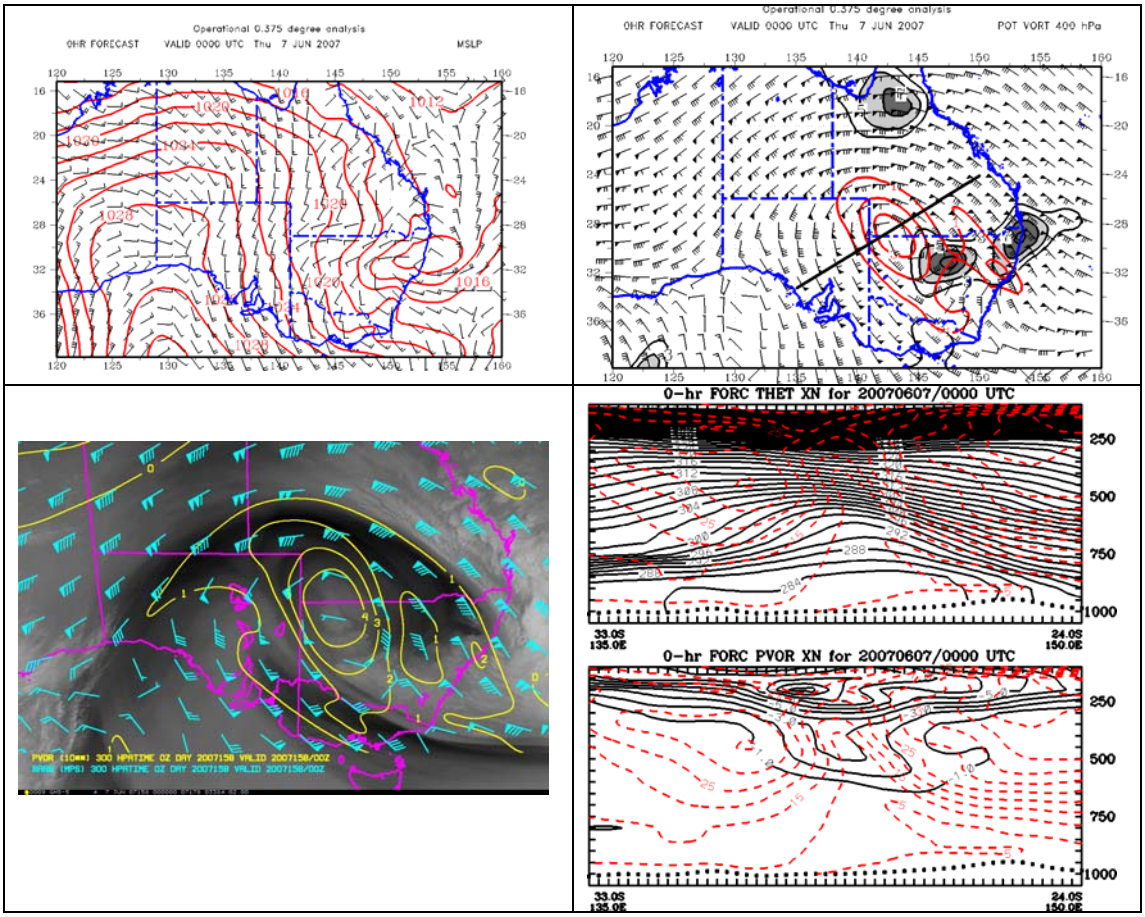

Fig. 11b As Fig. 11a for the LAPS analysis fields valid at 0000 UTC 7 June 2007.

During the following 24-hours the upper-low moved eastwards, and the filaments of shear IPV (see Bell and Keyser 1993) continued to rotate around and interact with the IPV centre marking the deep tropopause depression at the centre of the cut-off low. By 0000 UTC 8 June 2007 (Fig. 11c), the highly asymmetric shape, with multiple lobes, of the 300 hPa and 400 hPa IPV patterns reflect the strong effects of shear vorticity. A deep tropopause depression, with stronger tropopause folding now on the northeast side, is seen in the cross-sections. The q-g forcing of height falls is now focussed, and shows greater amplitude, over the far northeast of NSW, just northwest of the surface low. This low had deepened some 4 hPa off the northern NSW coastline over the previous 24 hours, while slowly moving southwards. The combined effects of the decreasing central pressure, the southward movement of the low, and the rising pressures over eastern Victoria and the far south coast of NSW had significantly strengthened the pressure gradient on the southern side of the low and a broad region of winds well above gale force are analysed over the Tasman Sea south of the low.

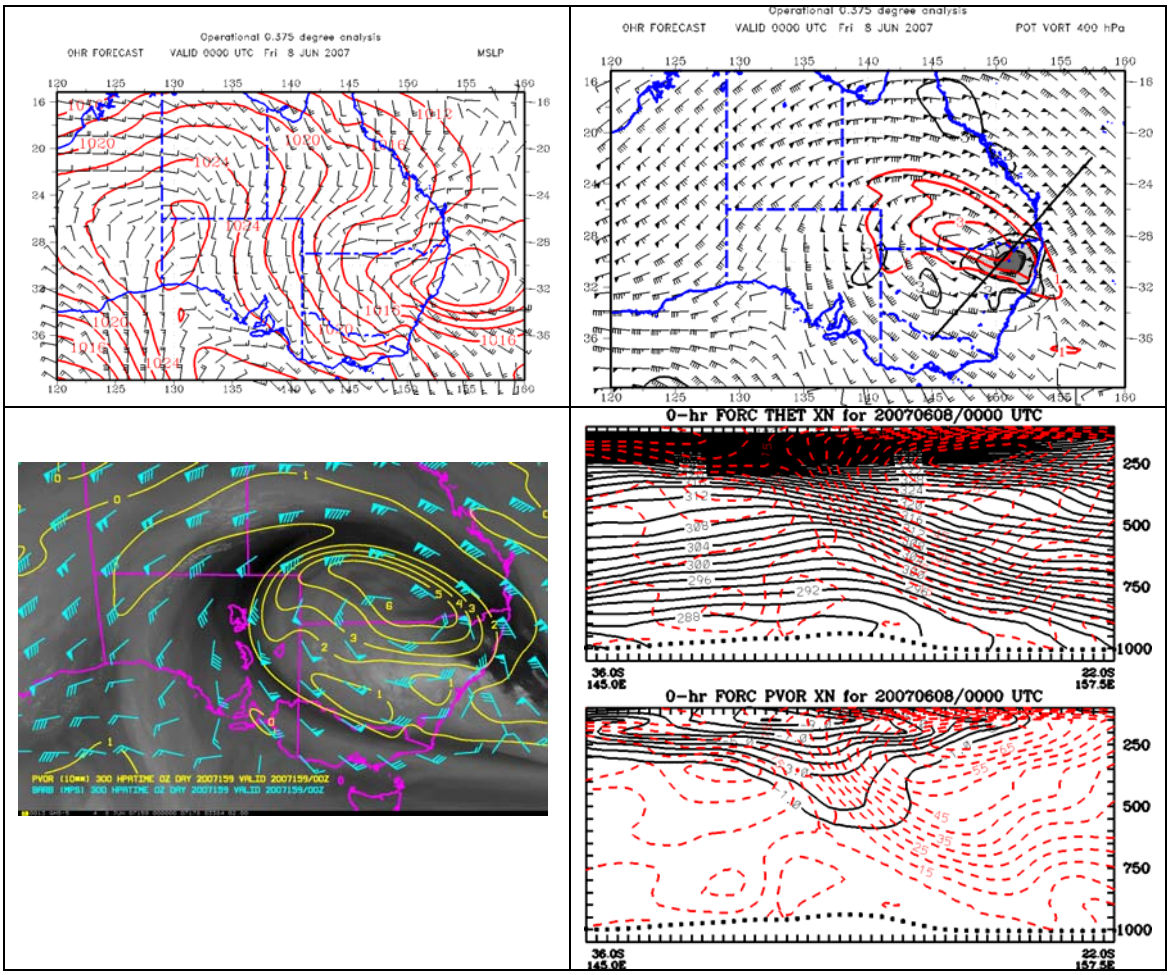

Fig. 11c As Fig. 11a for the LAPS analysis fields valid at 0000 UTC 8 June 2007.

The following four sets of plots are at 6-hour intervals to cover the period of major weather impact on the coastal regions of NSW. At 0600 UTC 8 June (Fig. 11d) the IPV maximum, still highly elongated, extends southeast across the coastline, with a focussed q-g height fall forcing centre directly above the deepening low on the NSW coastline. The dark areas in the WV imagery align with this IPV band, and suggest that the mid- to upper-tropospheric dry air is over-running the band of moist (cloudy) air aligned with the band of gale-force low-level easterly winds. The cross-section indicates that the tropopause depression had lowered to nearly 700 hPa. The forcing of height falls focussed near the coast and over the surface low centre can be qualitatively explained by the advection of IPV to the southwest as the upper winds turn sharply cyclonically from northwesterly to southeasterly, crossing the IPV contours. At this stage the centre of the upper circulation, which is still over the Qld/NSW border, is well northwest of the surface low pressure system. Also apparent is the very strong gradient in low-level wind speed approximately aligned with the 1006 hPa isobar, with very strong east-southeasterly winds to the south, and much weaker northwesterly winds to the north of this line. This demarcation is consistent with the very abrupt changes in wind speed at Mangrove Mountain, Nobbys Head, Norah Head, and Williamtown shown in Figs 4 and 5, and also with the lower wind speeds experienced throughout 8 and 9 June at stations further north along the coast (Tocal, Forster, and Port Macquarie, not shown). This aspect of the low's structure will be discussed further in Section 5 of this paper.

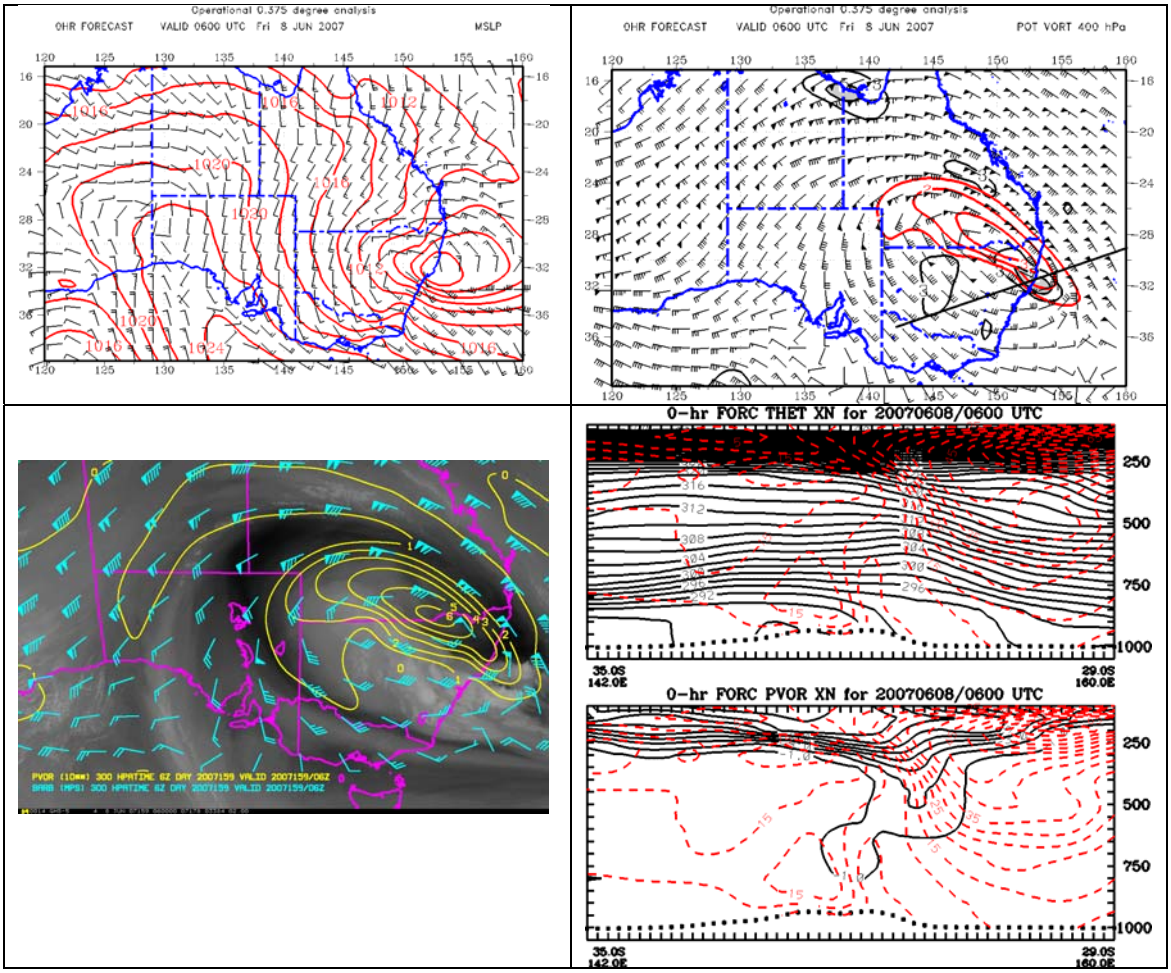

Fig. 11d As Fig. 11a for the LAPS analysis fields valid at 0600 UTC 8 June 2007.

At 1200 UTC (Fig. 11e) the broad-scale surface analysis shows an low pressure system elongated east-west off the central NSW coastline, and some waves can be seen in the WV image on the edge of the moist band off the NSW coast (see also Fig. 8j). At this time the circulation centre of the upper low is still northwest of the surface low, but the distance between the two has decreased considerably in only 6 hours. By 1800 UTC (Fig. 11f) the upper low circulation centre had moved offshore, and the surface low was located just to its southwest, and quite close to the western centre of q-g height fall forcing. Particularly notable from the weather forecast perspective is the extreme asymmetry of the pressure gradient around the low, with consequent asymmetric distribution of wind, cloud, and precipitation. In the cross-section the tropopause undulation shows a downward slope towards the east-northeast, but another small IPV maximum is seen in the lower troposphere on the cyclonic flank of the southeasterly low-level jet.

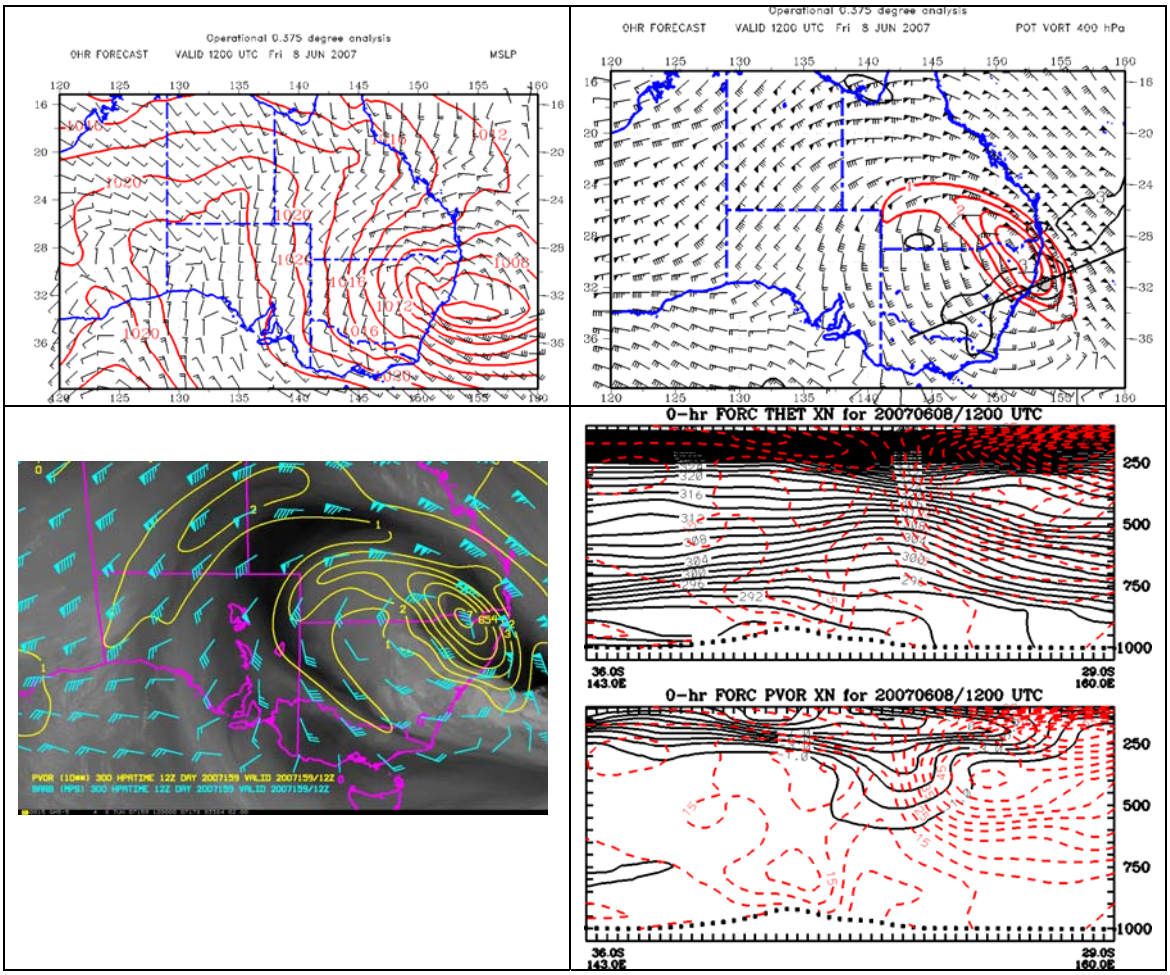

Fig. 11e As Fig. 11a for the LAPS analysis fields valid at 1200 UTC 8 June 2007.

In the final set of panels, valid at 0000 UTC 9 June 2009 (Fig. 11g), the upper low is moving southeastwards, with forcing of height falls ahead of it, and the surface low is again showing multiple structures. The coastal low west of the upper circulation centre is weakening and moving northwards, while a new centre of low pressure is developing to the southeast in the Tasman Sea, under the influence of the upper forcing maximum there.

The later stages of this development are very similar to the evolution of the Sydney-Hobart yacht race low which developed in eastern Bass Strait, and ultimately was at its most intense when just west of the centre of the upper low (Mills 2001).

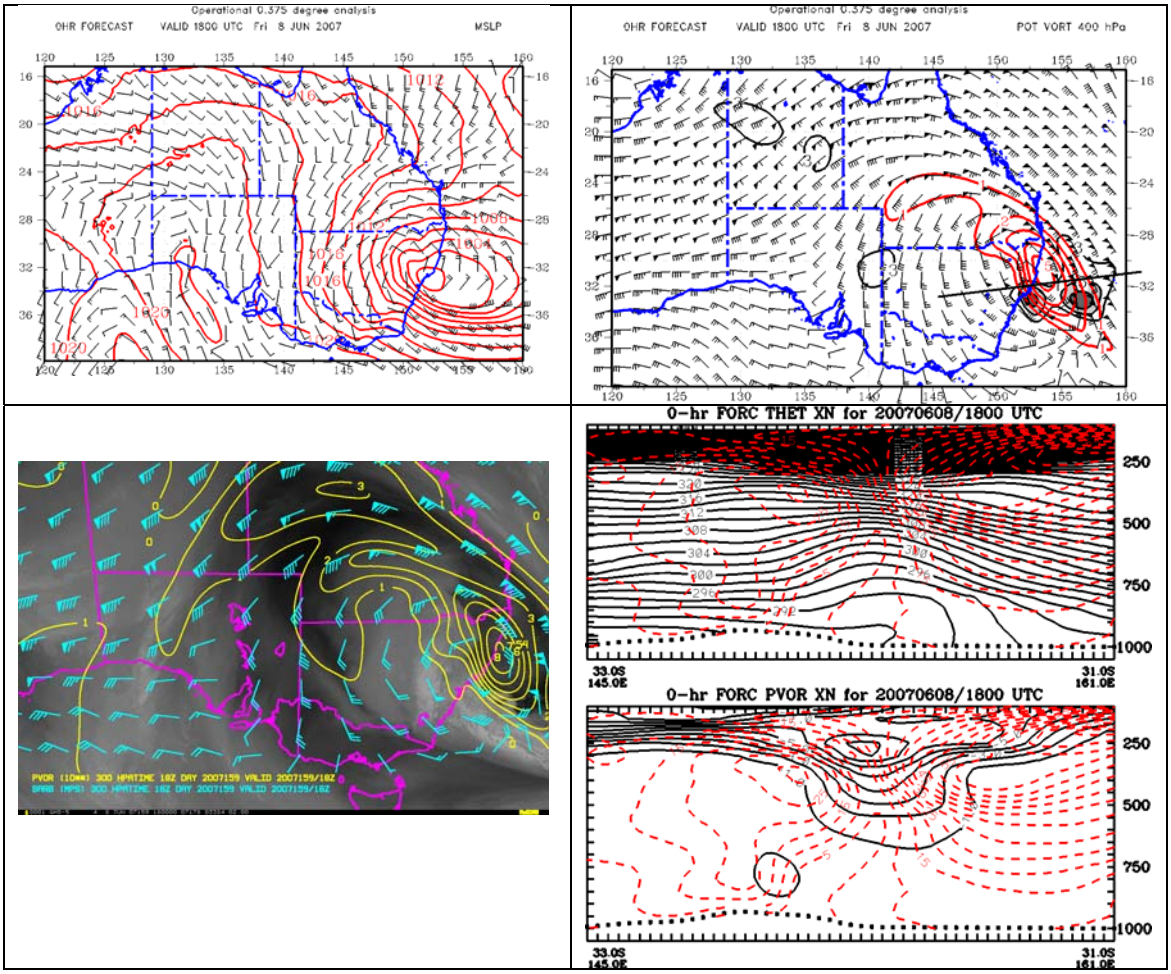

Fig. 11f As Fig. 11a for the LAPS analysis fields valid at 1800 UTC 8 June 2007.

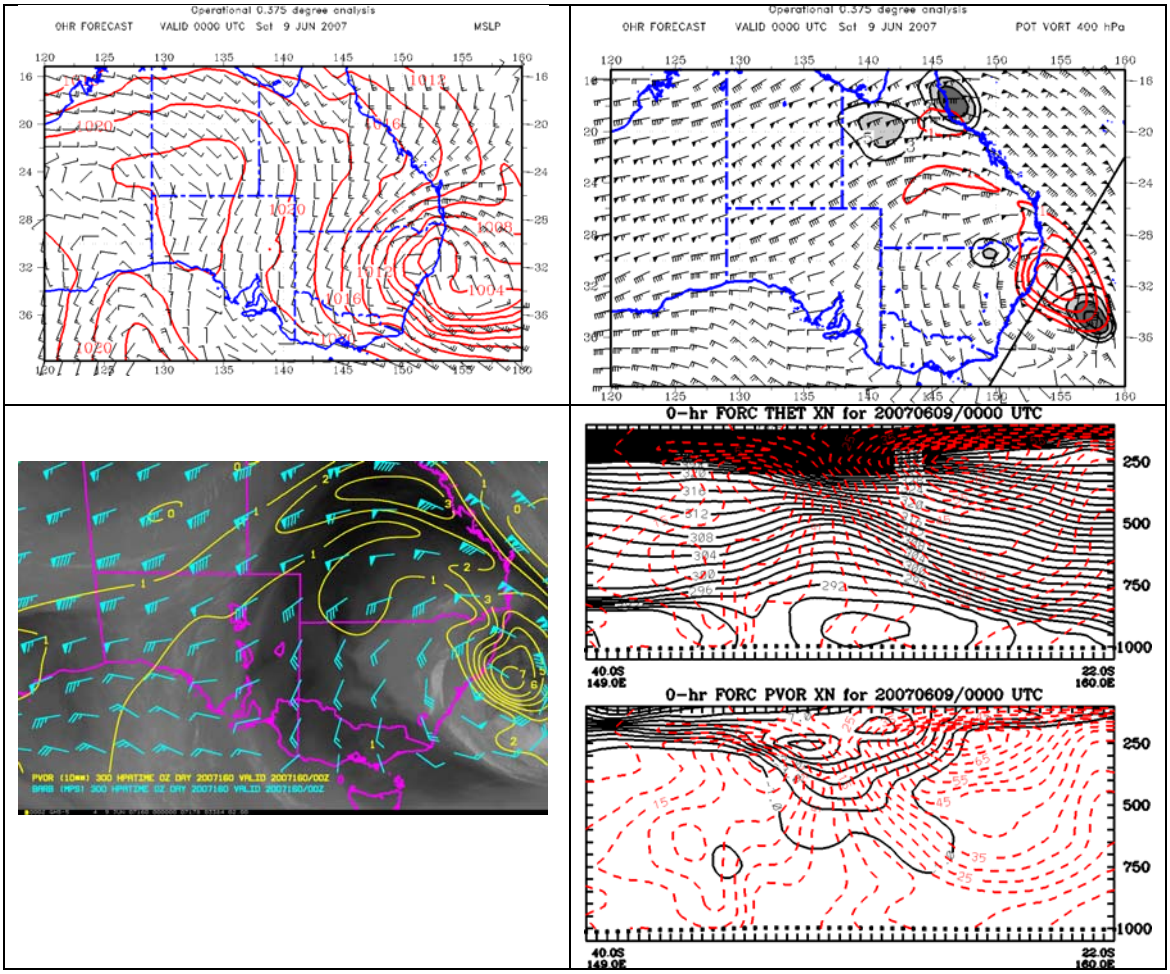

Fig. 11g As Fig. 11a for the LAPS analysis fields valid at 0000 UTC 9 June 2007.

4.2 Other major east coast cyclones

The very marked upper cut-off low (Fig. 10) development prior to the major intensification of the surface low pressure system suggests the interesting question of whether this is a normal or a necessary part of east coast low life-cycles.

In this section figures similar to Fig. 10 are presented for a number of notable (high impact) east coast low events gleaned either from the literature or from the Bureau's web-site. http://reg.bom.gov.au/weather/nsw/sevwx/facts/ecl.shtml#hist. For each event, three upper-tropospheric geopotential height/wind and MSLP analyses are shown, at either 24- or 36-hour intervals ending near the time of minimum surface pressure. The events chosen are:

- The "Sygna" storm (Bridgeman 1986) of 26 May 1974, when the Sygna was driven ashore near Newcastle, and wind gusts of nearly 90 knots were recorded at Nobbys Head (Fig. 12).

- The three east coast lows in July 1984 described by Holland et al. (1987) (Figs 13-15).

- The 5 August 1986 low, during which rainfalls exceeding 300 mm in the Sydney region led to major flooding in the Nepean-Hawkesbury and the Georges River systems (Fig. 16).

- The two east coast lows in early August 1990 described by Hopkins (1997) (Figs 17,18).

- The 31 August 1996 low that produced a rainfall of 386 mm at Darkes Forest and wind gusts above 60 knots at Wollongong (Fig. 19).

- The 7-8 August 1998 storm during which many stations in the Sydney and Illawarra areas recorded greater than 300 mm of rainfall (Fig. 20).

- The 9 July 2005 low that developed on the southern NSW coastline and led to heavy precipitation on the coastal side of the ranges in southern NSW and eastern Victoria (Fig. 21).

- The 21 May 2009 low that formed off the southern Qld coastline and affected the coastline from Brisbane to northern NSW, and caused massive coastal erosion and major flooding of the Clarence River (Fig. 22).

The upper-tropospheric evolution during these cases is remarkably similar to that preceding the Pasha Bulker storm, with the common pattern being;

- 48 to 72 hours prior to the explosive development, an upper-tropospheric split-jet, or blocking pattern, with a positively tilted trough or cut-off low over southeastern Australia.

- Amplification of the upstream trough over the Indian Ocean followed by downstream amplification of the ridge south of Australia.

- The next stage of this energy-dispersion process is the development of a southerly jet streak on the western side of the positively tilted trough over eastern Australia.

- As this southerly jet streak propagates towards the apex (lower latitudes) of the trough, the trough/cut-off low deepens and begins to negatively (towards the northeast) tilt and move towards the coast.

- The northwesterly jet on the northeast flank of the upper cut-off strengthens, becomes highly focussed, and the region of strong cyclonic shear near its exit becomes located very close to the centre of the upper cut-off low. In this regard the pattern is very similar to that described by Riseby et al. (2009) for cut-off lows that lead to the heavier rainfall events over the cropping areas of southeastern Australia. The consequence of this evolution is a focussing of IPV advection on the northeast side of the cut-off low, which forces pressure falls at the surface.

- If/where low-level ingredients (baroclinicity/lesser static stability/more rapid growth rates etc) are suitable, explosive development (i.e. rapid intensification) of an east coast low occurs.

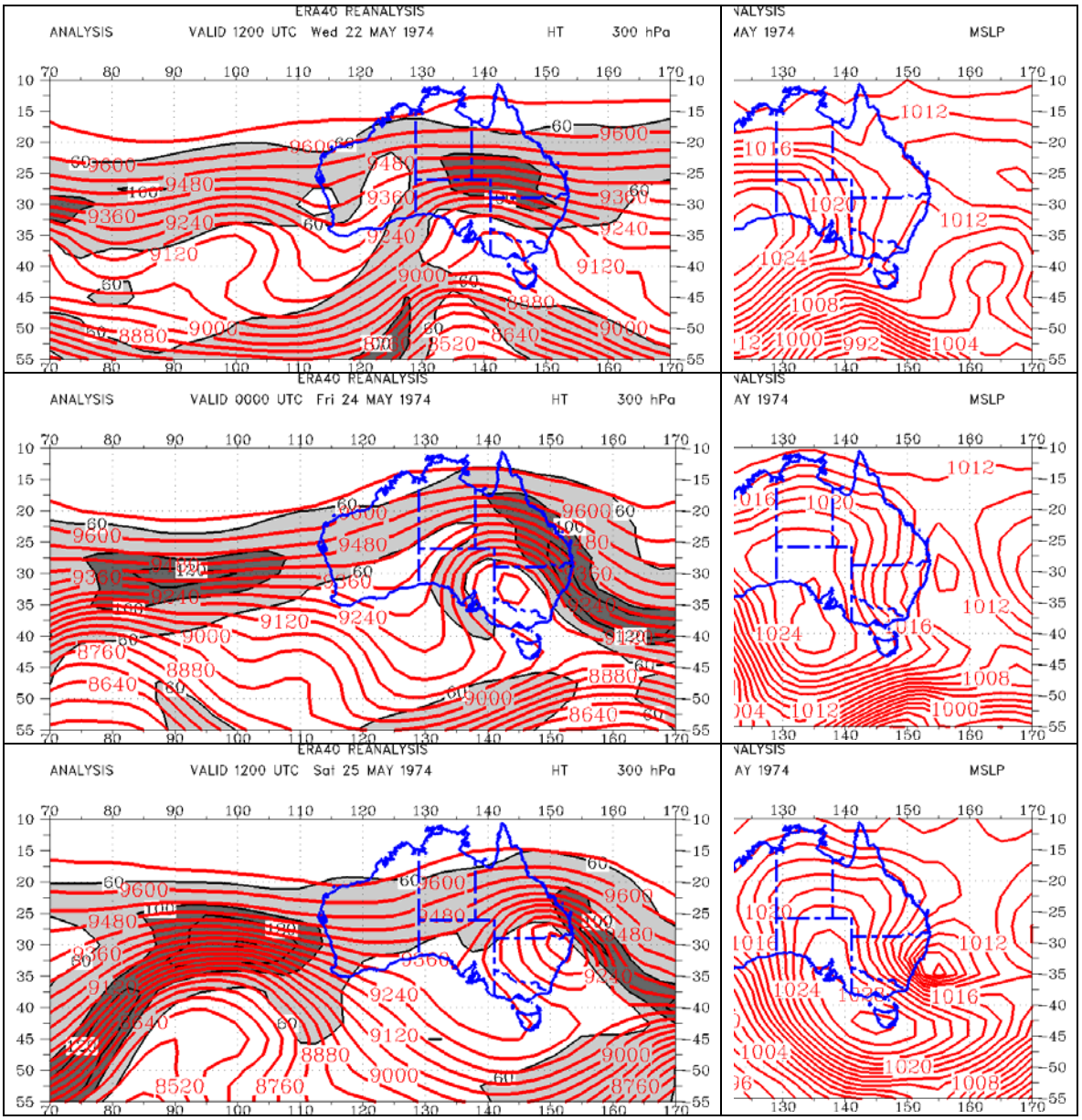

Fig. 12 ERA40 reanalysis fields of 300 hPa geopotential height and wind speed (left) and MSLP (right) at 36-hour intervals leading up to the development of the May 1974 “Sygna” east coast low. The 300 hPa wind speeds have light shading above 60 knots, and dark shading above 100 knots. The MSLP analyses have been cropped to focus on the eastern Australian sector.

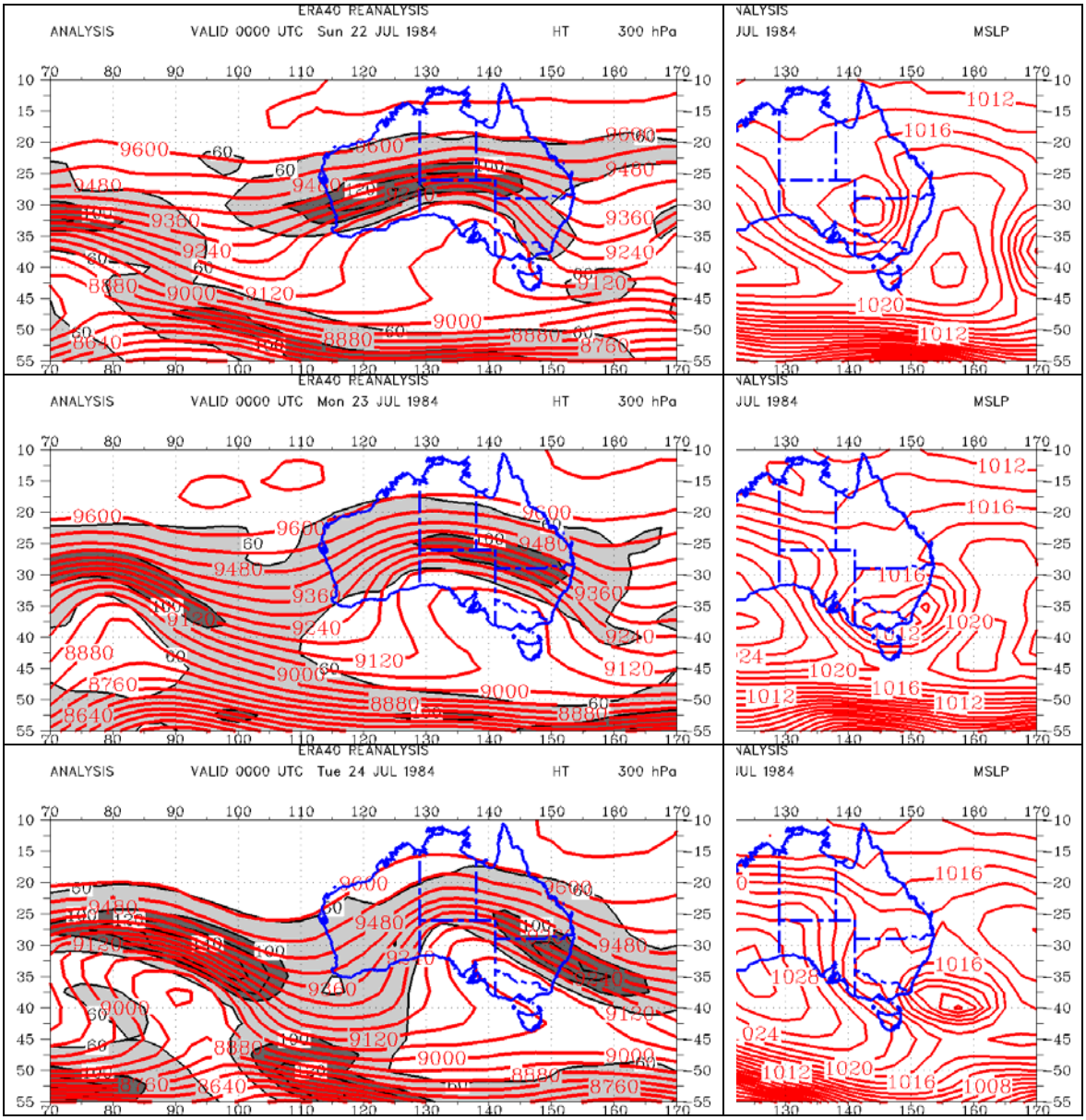

Fig. 13 ERA40 reanalysis fields of 300 hPa geopotential height and wind speed (left) and MSLP (right) at 24-hour intervals leading up to the development of the first of the July 1984 east coast lows reported by Holland et al. (1987). The 300 hPa wind speeds have light shading above 60 knots, and dark shading above 100 knots. The MSLP analyses have been cropped to focus on the eastern Australian sector.

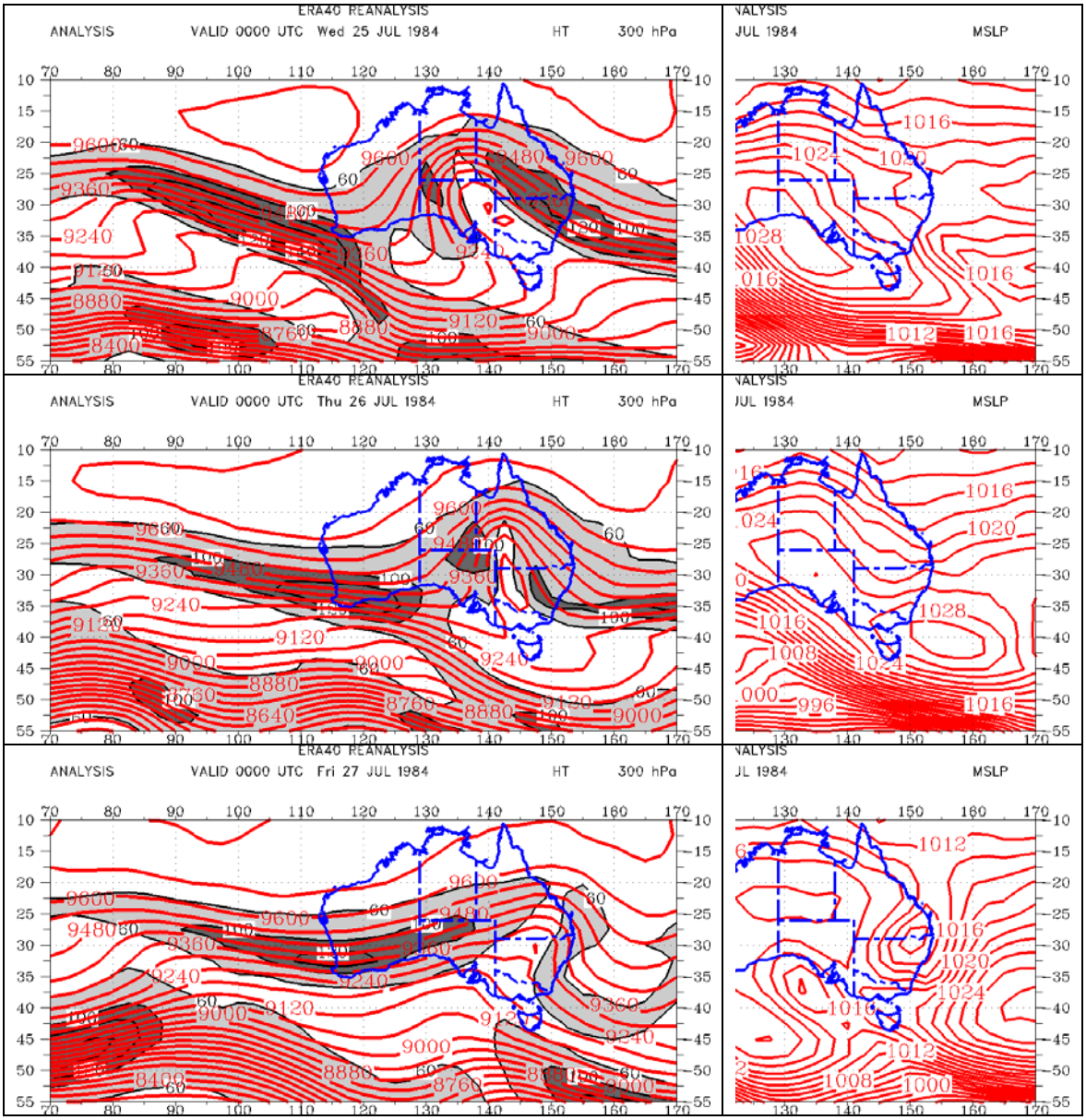

Fig. 14 ERA40 reanalysis fields of 300 hPa geopotential height and wind speed (left) and MSLP (right) at 24-hour intervals leading up to the development of the second of the July 1984 east coast lows reported by Holland et al. (1987). The 300 hPa wind speeds have light shading above 60 knots, and dark shading above 100 knots. The MSLP analyses have been cropped to focus on the eastern Australian sector.

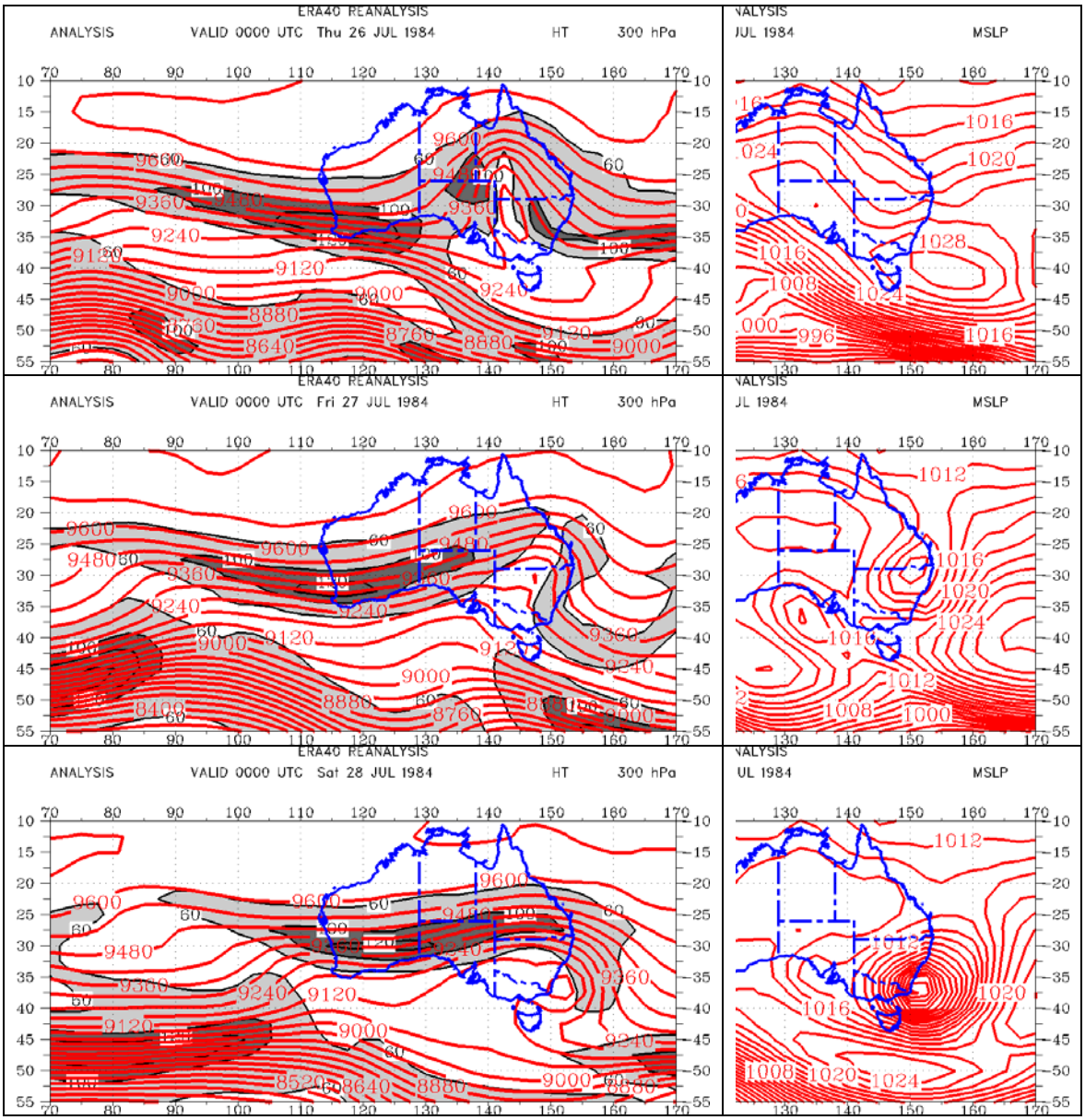

Fig. 15 ERA40 reanalysis fields of 300 hPa geopotential height and wind speed (left) and MSLP (right) at 24-hour intervals leading up to the development of the third of the July 1984 east coast lows reported by Holland et al. (1987). The 300 hPa wind speeds have light shading above 60 knots, and dark shading above 100 knots. The MSLP analyses have been cropped to focus on the eastern Australian sector.

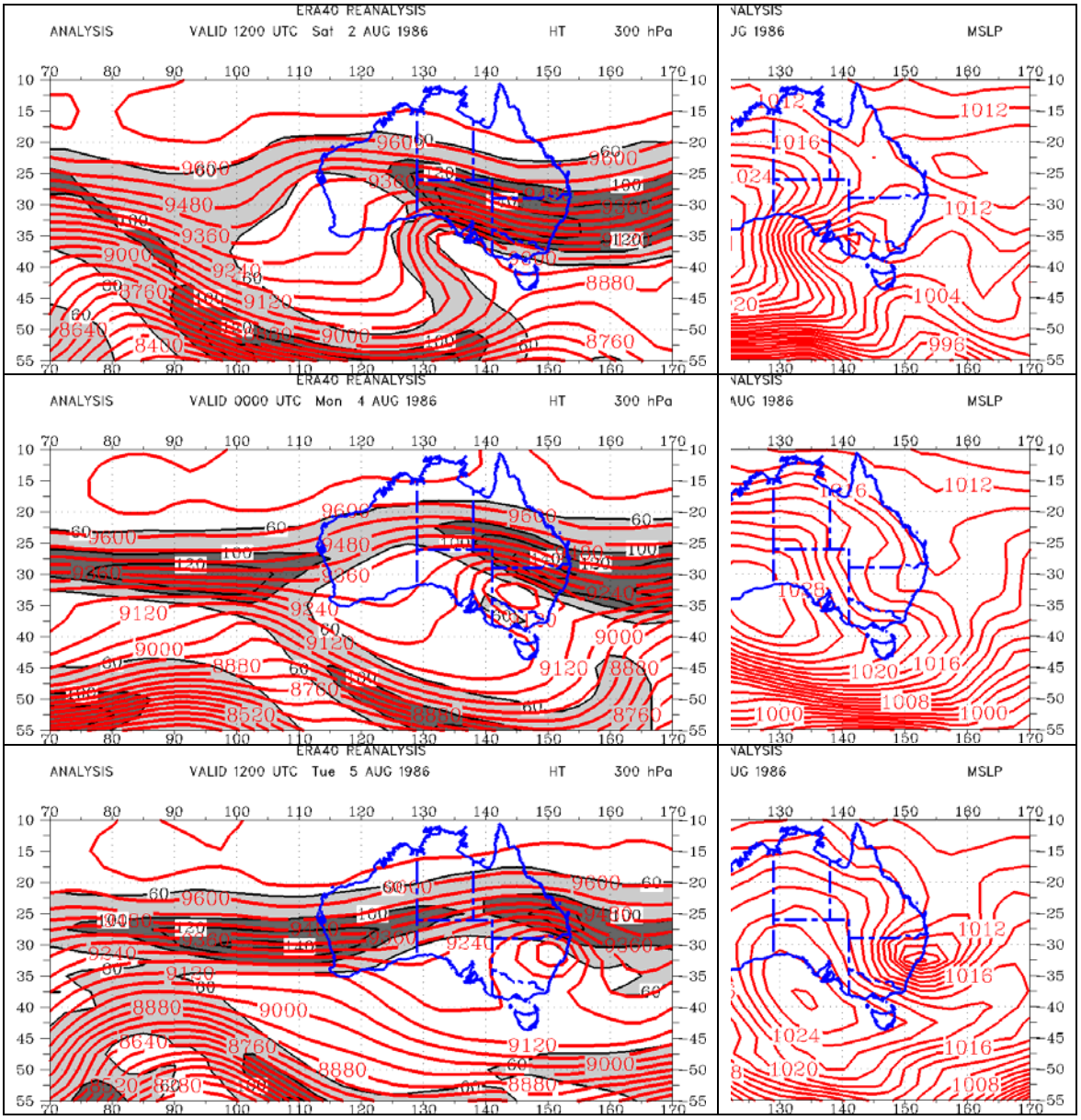

Fig. 16 ERA40 reanalysis fields of 300 hPa geopotential height and wind speed (left) and MSLP (right) at 36-hour intervals leading up to the development of the August 1986 east coast low. The 300 hPa wind speeds have light shading above 60 knots, and dark shading above 100 knots. The MSLP analyses have been cropped to focus on the eastern Australian sector.

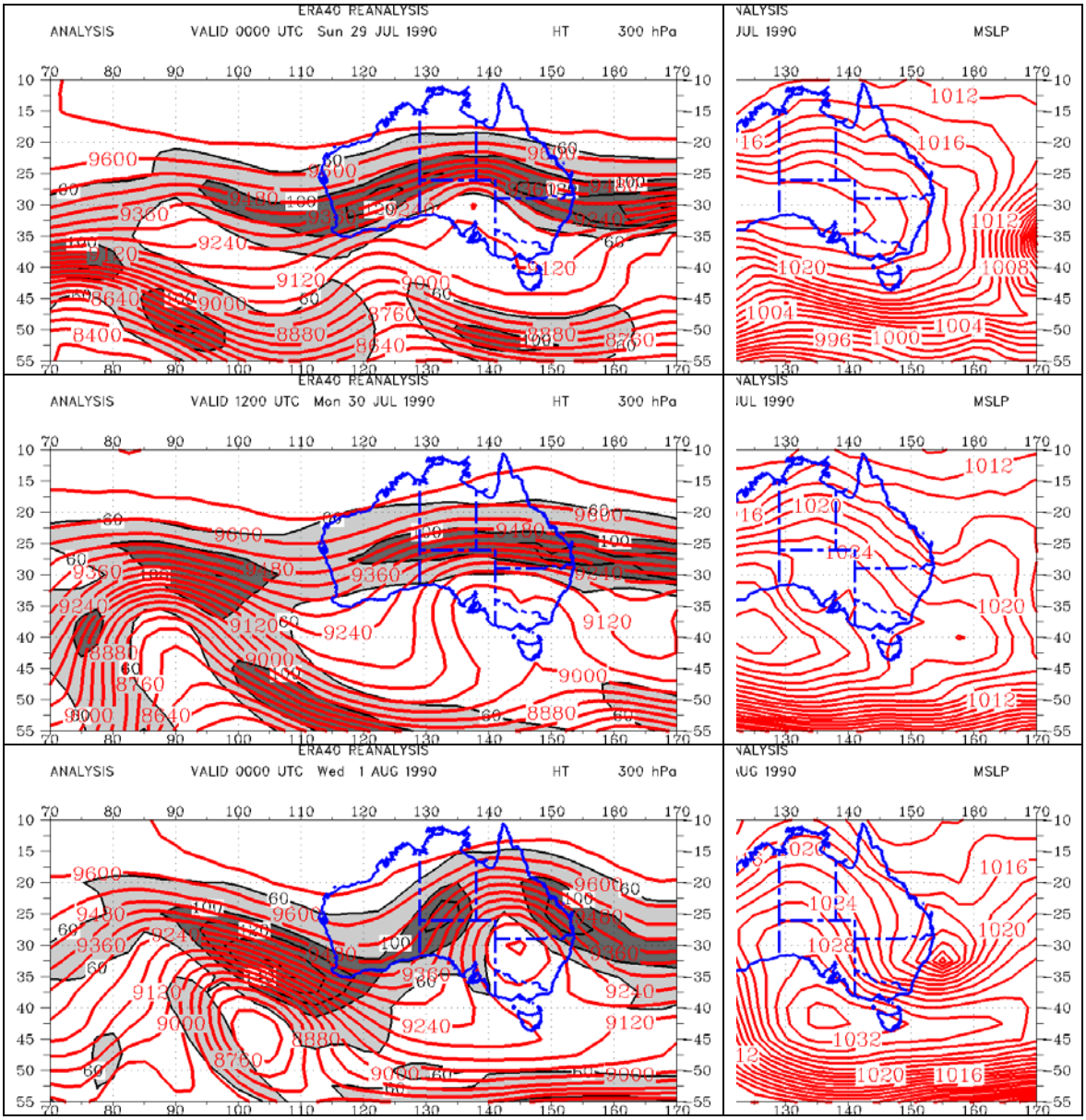

Fig. 17 ERA40 reanalysis fields of 300 hPa geopotential height and wind speed (left) and MSLP (right) at 36-hour intervals leading up to the development of the first of the “August 1990” east coast lows. The 300 hPa wind speeds have light shading above 60 knots, and dark shading above 100 knots. The MSLP analyses have been cropped to focus on the eastern Australian sector.

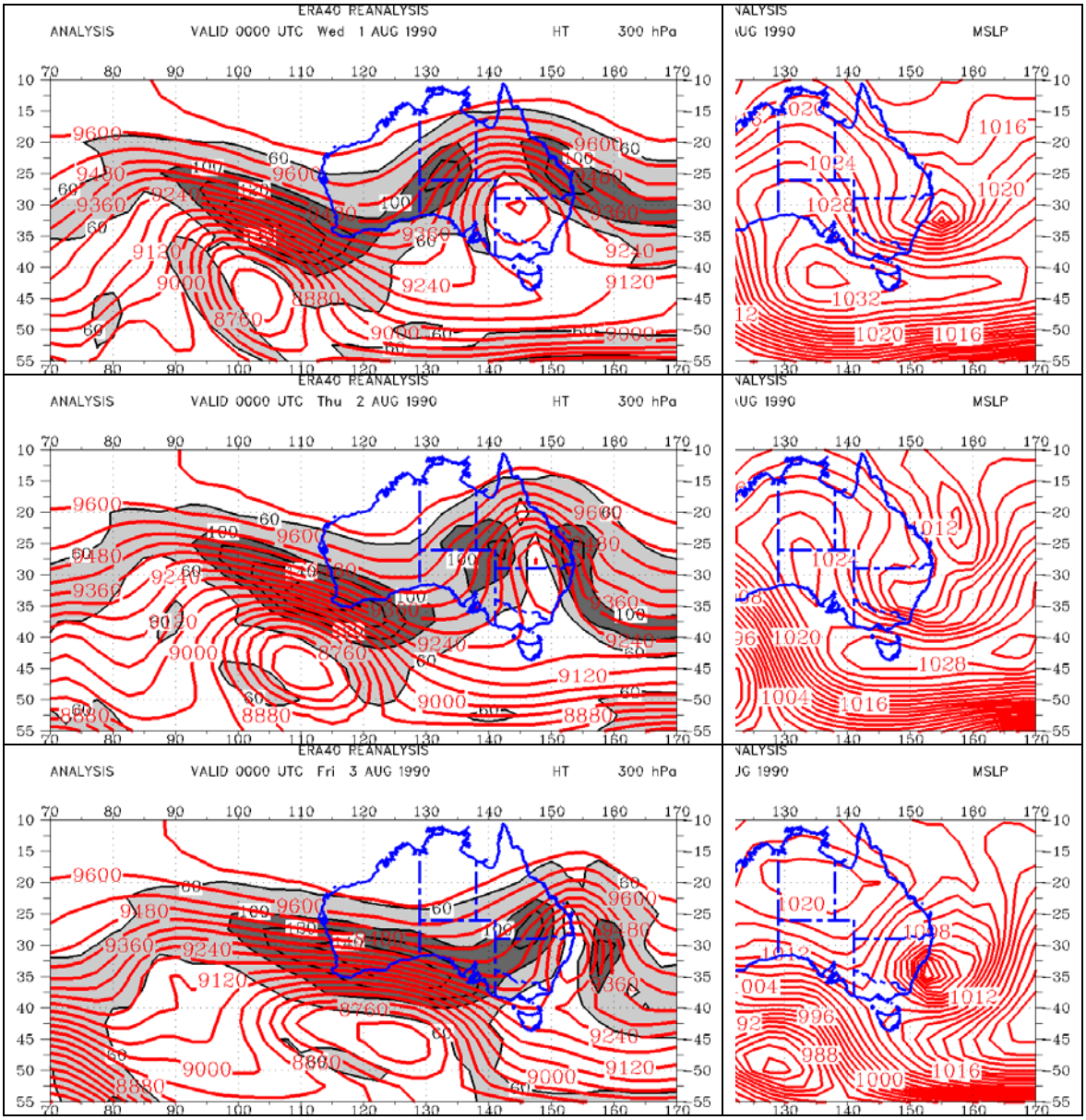

Fig. 18 ERA40 reanalysis fields of 300 hPa geopotential height and wind speed (left) and MSLP (right) at 24-hour intervals leading up to the development of the second of the “August 1990” east coast lows. The 300 hPa wind speeds have light shading above 60 knots, and dark shading above 100 knots. The MSLP analyses have been cropped to focus on the eastern Australian sector.

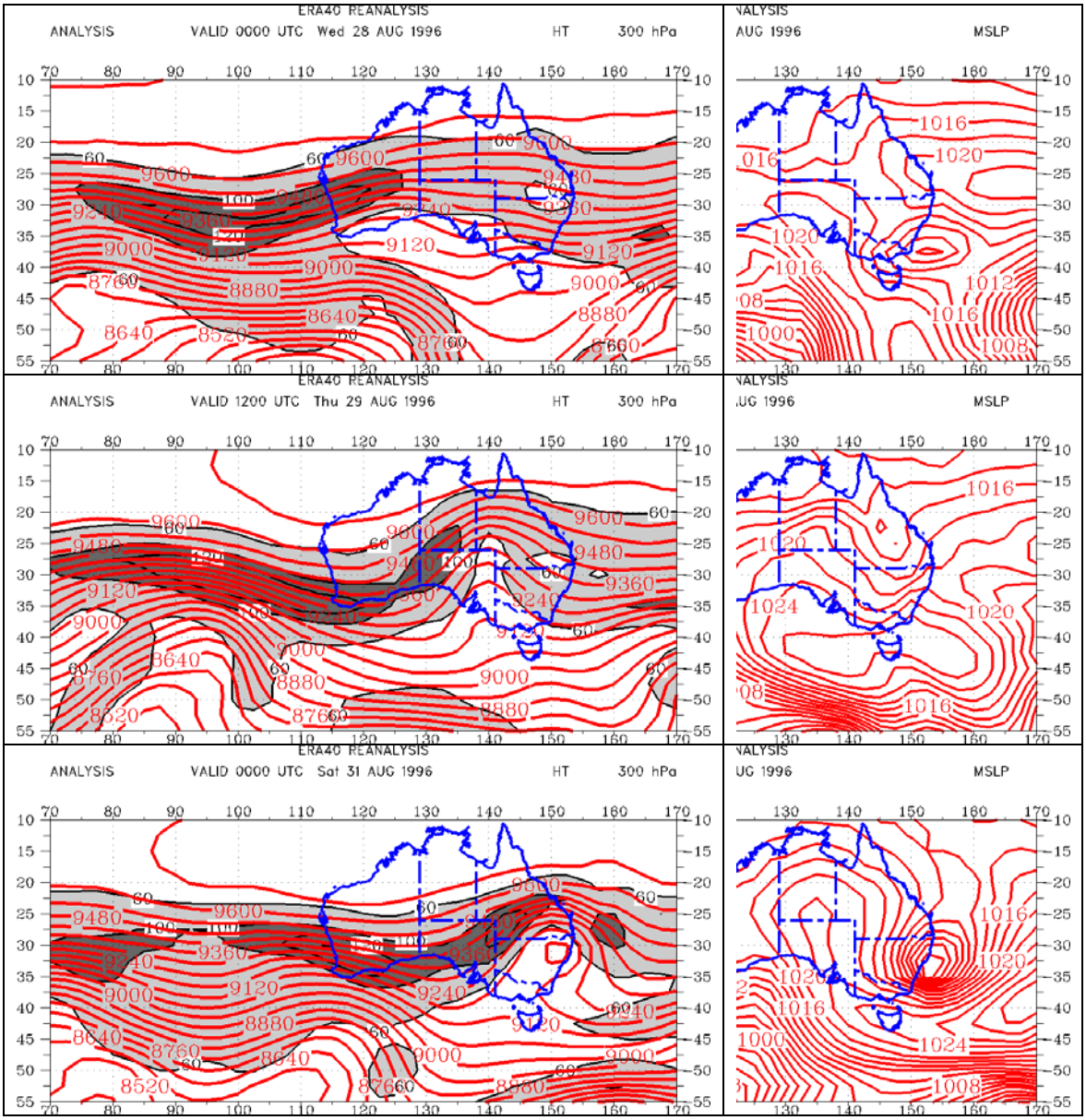

Fig. 19 ERA40 reanalysis fields of 300 hPa geopotential height and wind speed (left) and MSLP (right) at 36-hour intervals leading up to the development of the August 1996 east coast low. The 300 hPa wind speeds have light shading above 60 knots, and dark shading above 100 knots. The MSLP analyses have been cropped to focus on the eastern Australian sector.

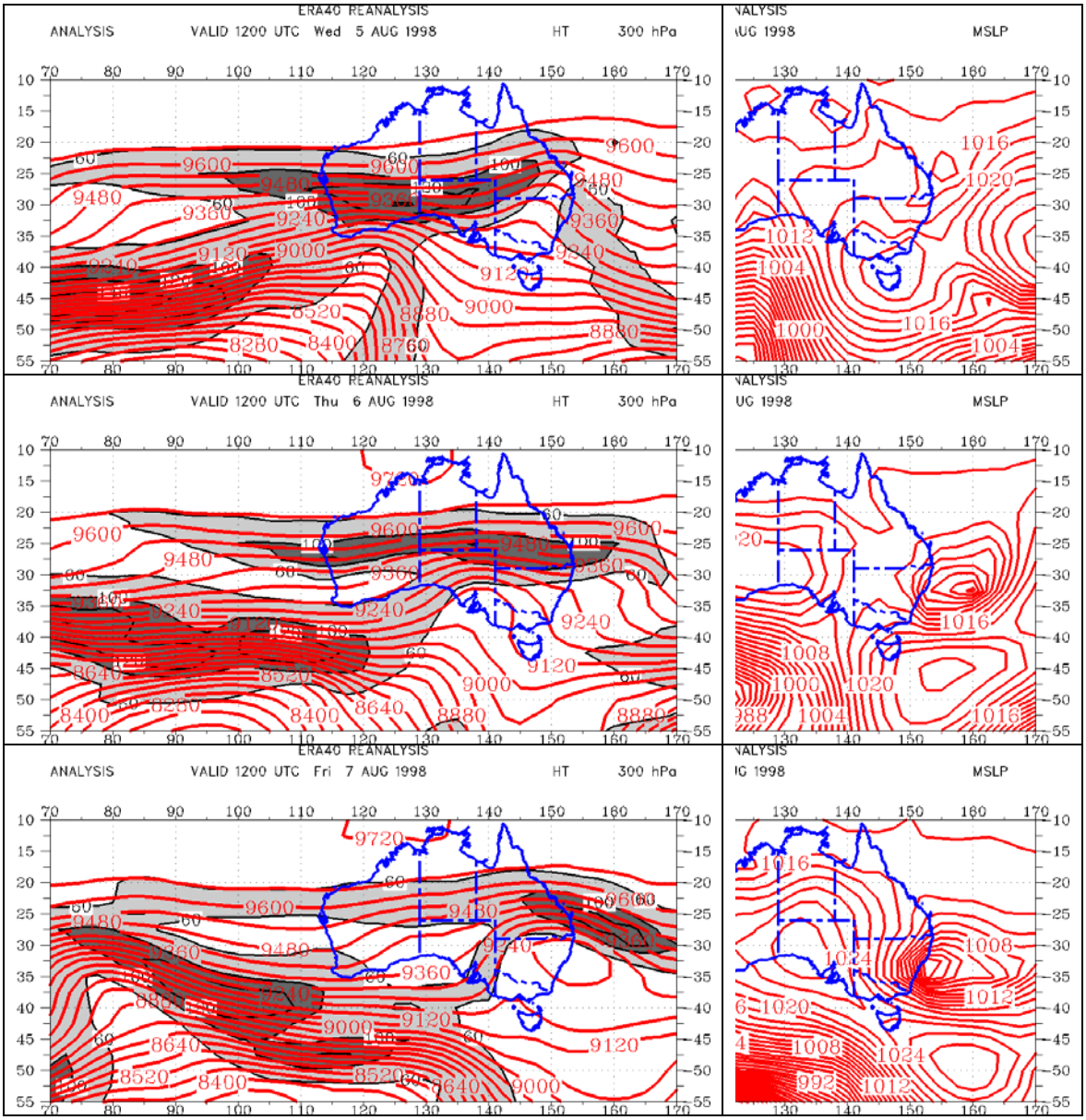

Fig. 20 ERA40 reanalysis fields of 300 hPa geopotential height and wind speed (left) and MSLP (right) at 24-hour intervals leading up to the development of the August 1998 east coast low. The 300 hPa wind speeds have light shading above 60 knots, and dark shading above 100 knots. The MSLP analyses have been cropped to focus on the eastern Australian sector.

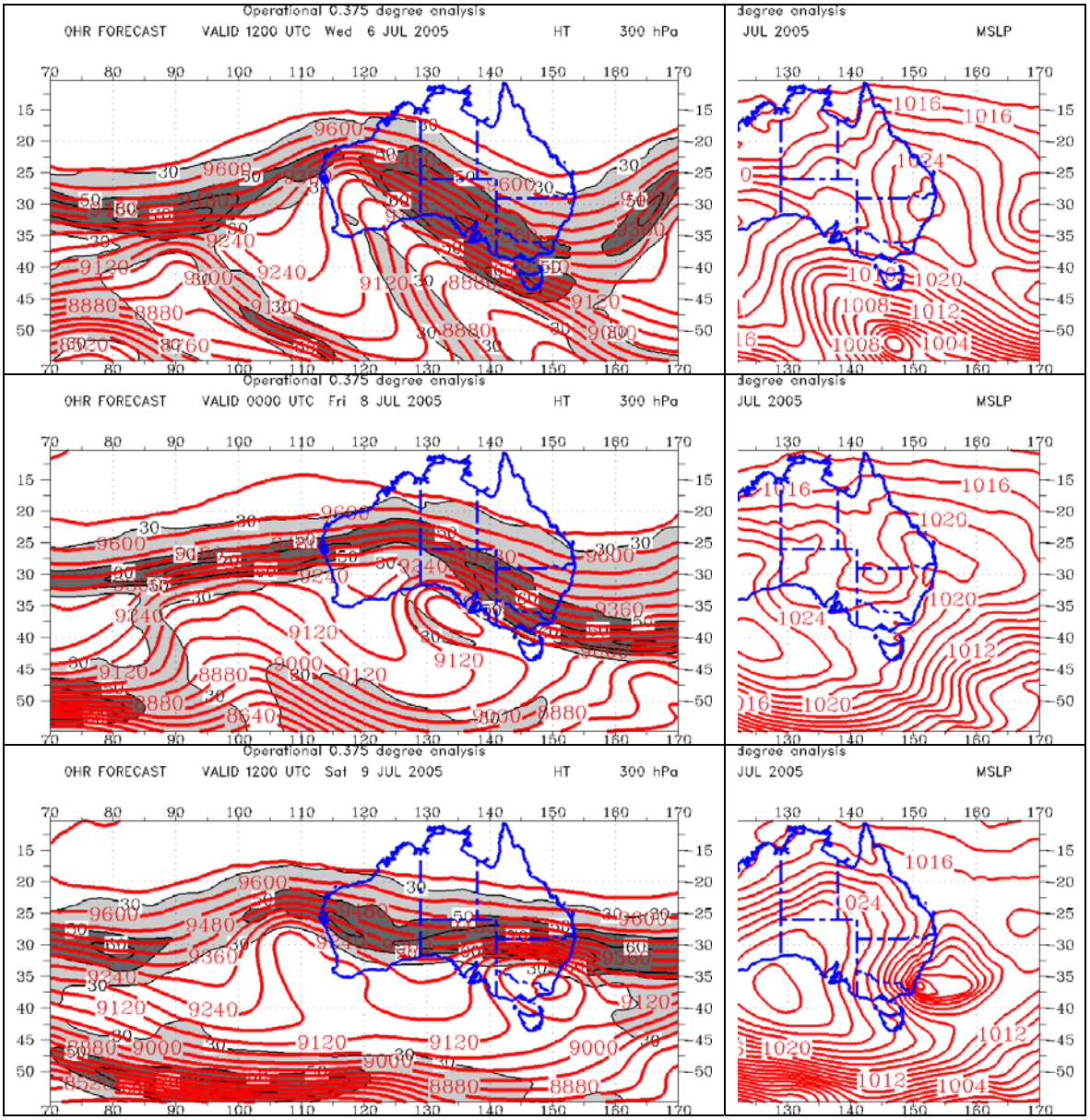

Fig. 21 LAPS analysis fields of 300 hPa geopotential height and wind speed (left) and MSLP (right) at 36-hour intervals leading up to the development of the July 2005 east coast low. The 300 hPa wind speeds have light shading above 30 m s^{-1}, and dark shading above 50 m s^{-1}. The MSLP analyses have been cropped to focus on the eastern Australian sector.

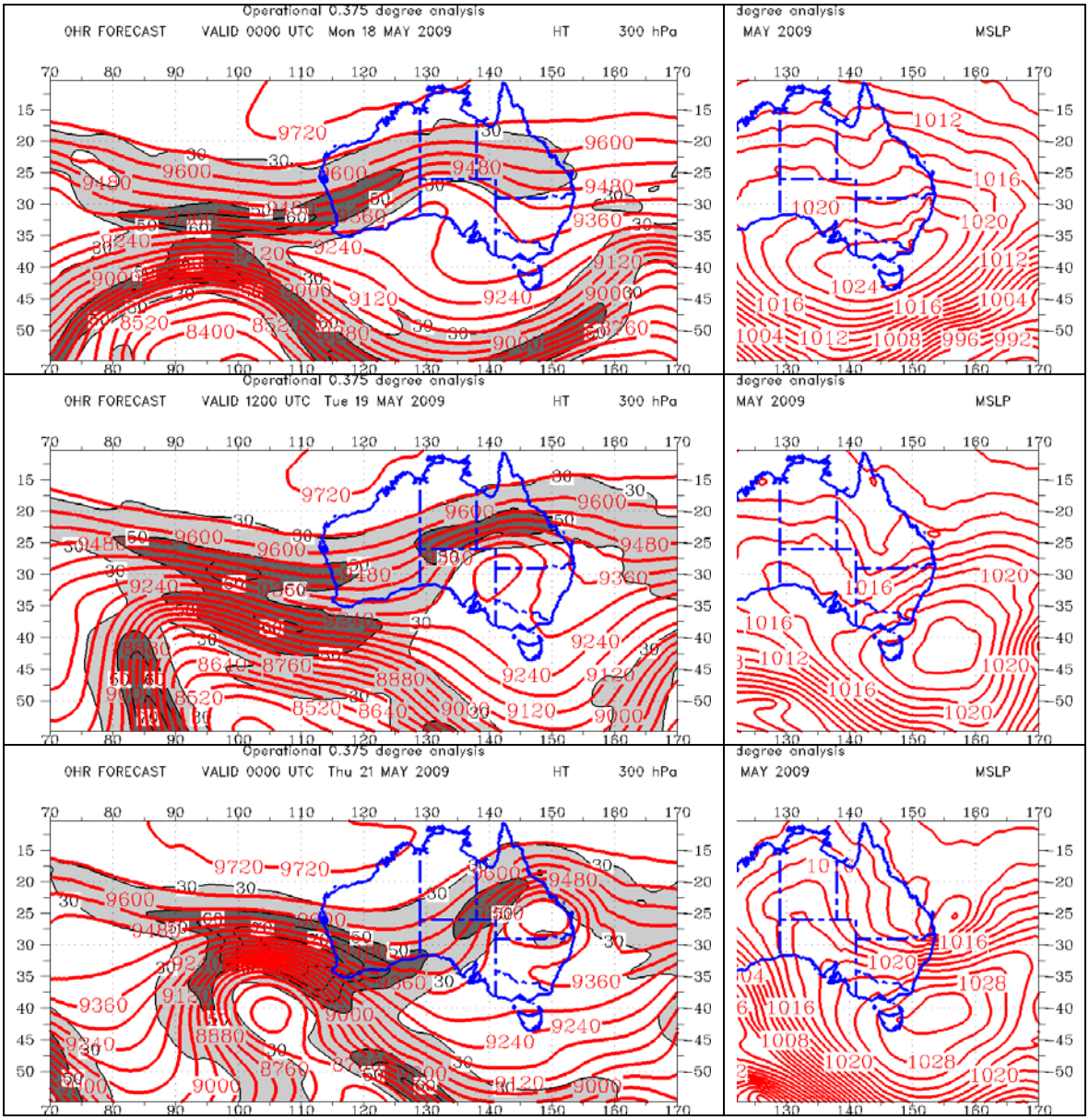

Fig. 22 LAPS analysis fields of 300 hPa geopotential height and wind speed (left) and MSLP (right) at 36-hour intervals leading up to the development of the May 2009 east coast low. The 300 hPa wind speeds have light shading above 30 m s^{-1}, and dark shading above 50 m s^{-1}. The MSLP analyses have been cropped to focus on the eastern Australian sector.

The surface patterns also show some interesting features. While the developed east coast lows are generally located on the cyclonic side of the jet stream, in a number of cases there is trough or low pressure development on the anticyclonic side of the jet in the earlier part of the synoptic evolution (Figs 12, 17, 18, 20, and 21). Hopkins (1997) noted this in the case of the August 1990 storm. This does not necessarily indicate that the final explosively developing low has ”passed beneath” the jet stream during its evolution. It can equally be argued that these are separate low pressure system developments. Another feature is the number of surface lows that reach their major intensity with the upper low either above, or to the *east*, of the position of the surface low (Figs 11f, 15, Fig. 18, Fig. 19, Fig. 20). This is very similar to the development of the Sydney-Hobart yacht race low (Mills 2001), and suggests that many of these lows may

develop in this way. This has consequences for the morphology of the low-level wind field, as will be discussed in Section 5.

The number of these major events that show high amplitude, large-scale upper tropospheric waves in the early stages of their life-cycle suggests the hypothesis that a large-scale upper tropospheric cut-off low, or at least a large amplitude trough, is a necessary condition for explosive east coast low development. The inverse to this hypothesis is, of course, how often do large-scale upper-tropospheric wave structures cross the coastline without causing major cyclogenesis? If it can be shown that the development of the upper low is necessary for subsequent explosive lower tropospheric cyclogenesis, then this type of analysis could be applied to GCM simulations of future climates to determine indications of trends in frequencies of east coast lows in the future, with implications for both water resource planning and disaster mitigation. These questions are the subject of on-going research using reanalysis data sets (Dowdy et al. 2010).

5 LOW LEVEL WIND AND THERMAL STRUCTURE

It was seen in Figs 11a-g that the strongest winds were concentrated to the south of the main low centre, associated with a highly asymmetric (relative to the low centre) pressure gradient. There was also a very strong cyclonic shear on the northern flank of this low-level jet. This structure is supported by scatterometer wind fields (not shown, but available from http://manati.orbit.nesdis.noaa.gov/cgi-bin/windsat_day_wdsp-1.pl), and implied by the abrupt changes in wind speed associated with sharp direction shifts seen in Figs 4 and 5, and by the much weaker wind strengths observed at AWS sites north of Williamtown.

The asymmetric structure of this low-level jet is very similar to that of the wind fields around the Sydney-Hobart yacht race low, and in that study Mills (2001) attributed this asymmetry of the low-level jet to the asymmetry of the low-level temperature field, this being produced by differential rotation of the isotherms bringing warmer tropical air south of the low. The circulation associated with this strong wind band/warm tongue also drives the cloud-band/rain-band that is so clearly seen in Fig. 8. As these several factors are critical weather elements in real-time forecasting and warning, and in terms of impact, this section describes the 3-dimensional structure of the low and how this evolving structure leads to this particular low-level wind and thermal distribution.

Figure 23 shows the 950 hPa wind fields from the LAPS analysis at 1200 UTC 8 June 2007, overlaid on the MSLP field and, separately, on the 950 hPa potential temperature field. The pressure field around the low (Fig. 23a) is highly asymmetric, with the strongest pressure gradient, and consequently strongest low level wind speeds, south of the low centre. The low-level jet has a very strong cyclonic shear on its northern side, and is closely associated with the cloudband. The thermal pattern (Fig. 23b) shows a warm tongue extending from the northeast and overlaying the elongated pressure minimum, and bears considerable similarity to the pattern that evolves by differential advection when a zonal temperature gradient is subjected to an imposed cyclonic vortex (Schultz et al. 1998). There is strong cold-air advection offshore north of the low pressure centre, and the strongest warm-air advection is where the southeasterly low-level jet crosses the coast. Finally, in the lower panel of Fig. 23, the 850 hPa vertical motion field is shown, and not surprisingly there is an elongated band of ascent aligned with the cloud band, and sharp ascent and descent bands associated with flow across the Great Dividing Range.

The pronounced asymmetry of the wind distribution around the low has significant implications for the issuing of warnings, with the bulk of the wind impacts well south of the low centre. Mills (2001) argued that the asymmetry in the low level thermal field led to the asymmetry of the pressure field, resulting in the strongest winds being on the southeast side and well away from the low centre, while winds (pressure gradients) were weaker near and north of the low centre. This can be demonstrated using hydrostatic arguments similar to those used by Hirschberg and Fritsch (1991a,b), who presented conceptual models of low-level pressure falls based on the changes in integrated temperature of the atmospheric column below a lower stratospheric "level of insignificant displacement". Each panel in Fig. 24 shows cross sections from southwest (left) to northeast (right) parallel to the NSW coastline, and more or less normal to the low-level jet. The upper panel (Fig. 24a) shows vertical cross-sections of IPV and overlaid wind speed (PVOR XN) and the potential temperature and overlaid vertical motion (THET XN). The thermal patterns are relatively complex, and it is not intuitively obvious where the vertically integrated cooler or warmer atmospheric columns are, particularly given the logarithmic dependence on pressure. The cross sections show a deep tropopause depression, with a very strong (> 60 m s^{-1}) jet on its northern side. There is a strong low-level jet south of the tropopause depression, with a peak speed > 30 m s^{-1}. The isentropes show a strongly descending band below the upper jet, a raised cold core in the lower troposphere below the IPV maximum, and a frontal structure associated with the low-level jet.

To demonstrate how the combined upper and lower tropospheric temperature anomalies generate the observed low-level pressure gradients, Fig. 24b shows the 100 hPa geopotential height profile (blue) and the 100-650 hPa thickness profile (magenta), and Fig. 24c shows the 650 hPa geopotential height profile (blue), the 650-1000 hPa thickness profile (magenta) and the 1000 hPa height profile (yellow). The 100 hPa height profile (Fig. 24b, blue), shows a monotonic increase from south to north, with a slowly increasing gradient, implying a strengthening westerly geostrophic wind with decreasing latitude. The 100-650 hPa thickness shows a maximum to the right of centre of the section, a result of the upper tropospheric warm anomaly associated with the steeply descending isentropes on the equatorward side of the IPV maximum, and on the cyclonic shear side of the jet stream.

The net result of the profiles in Fig. 24b (subtracting the 100-650 hPa thickness from the 100 hPa height) is a marked low at 650 hPa (Fig. 24c, blue line), with a stronger meridional gradient on the northern side of the low. The 650-1000 hPa thickness (Fig. 24c, magenta) profile along the plane of the section shows a maximum left (south) of centre of the cross-section, and a relative minimum right (north) of centre of the cross-section. The thickness minimum is a result of the raised isentropes below the upper tropospheric warm anomaly (the "cold core" of the cut-off, as seen in Fig. 1.140 of Bluestein 1992). This raising of the isentropes can be explained conceptually using either IPV thinking (Hoskins et al. 1985) or hydrostatic arguments (Hirschberg and Fritsch 1991a,b) to be a result of the lower-tropospheric vertical motion response to the advance of the upper-tropospheric warm anomaly (tropopause depression). That response leads to a reasonably symmetric cold lower tropospheric thermal anomaly in Bluestein's figure. However, the induced low-level cyclonic circulation also distorts the thermal pattern to wrap a lower-tropospheric warm tongue, which can ultimately become a warm seclusion (Shapiro and Keyser 1990), around the poleward side of the cyclonic circulation. This process has been demonstrated in idealised studies by Schultz et al. (1998) (their Fig. 14), and examples in the Australian context for the Sydney-Hobart yacht race low are in Mills (2001) and for the Pasha-Bulker storm in Fig. 23 of this report. The effects are manifest in the 650-1000 hPa thickness maximum to the left of centre of the section in Fig. 24c. Arrows link the

cool and warm anomalies in Fig. 24a with the resulting thickness maxima and minima in Figs 24b,c. Subtracting the 650 -1000 hPa thickness from the 650 hPa height in Fig 24c leads to the yellow 1000 hPa height profile, where the near-surface low centre is displaced well south of the mid-tropospheric low centre and, importantly, with a much stronger pressure gradient on its southern side. The net effect is that the strongest winds are concentrated in the easterly/southeasterly flow on the southern or southwestern side, and away from the centre of circulation, of the low, as is seen by the low-level jet in the upper panel (right hand arrows), and in the plan views in Fig. 23.

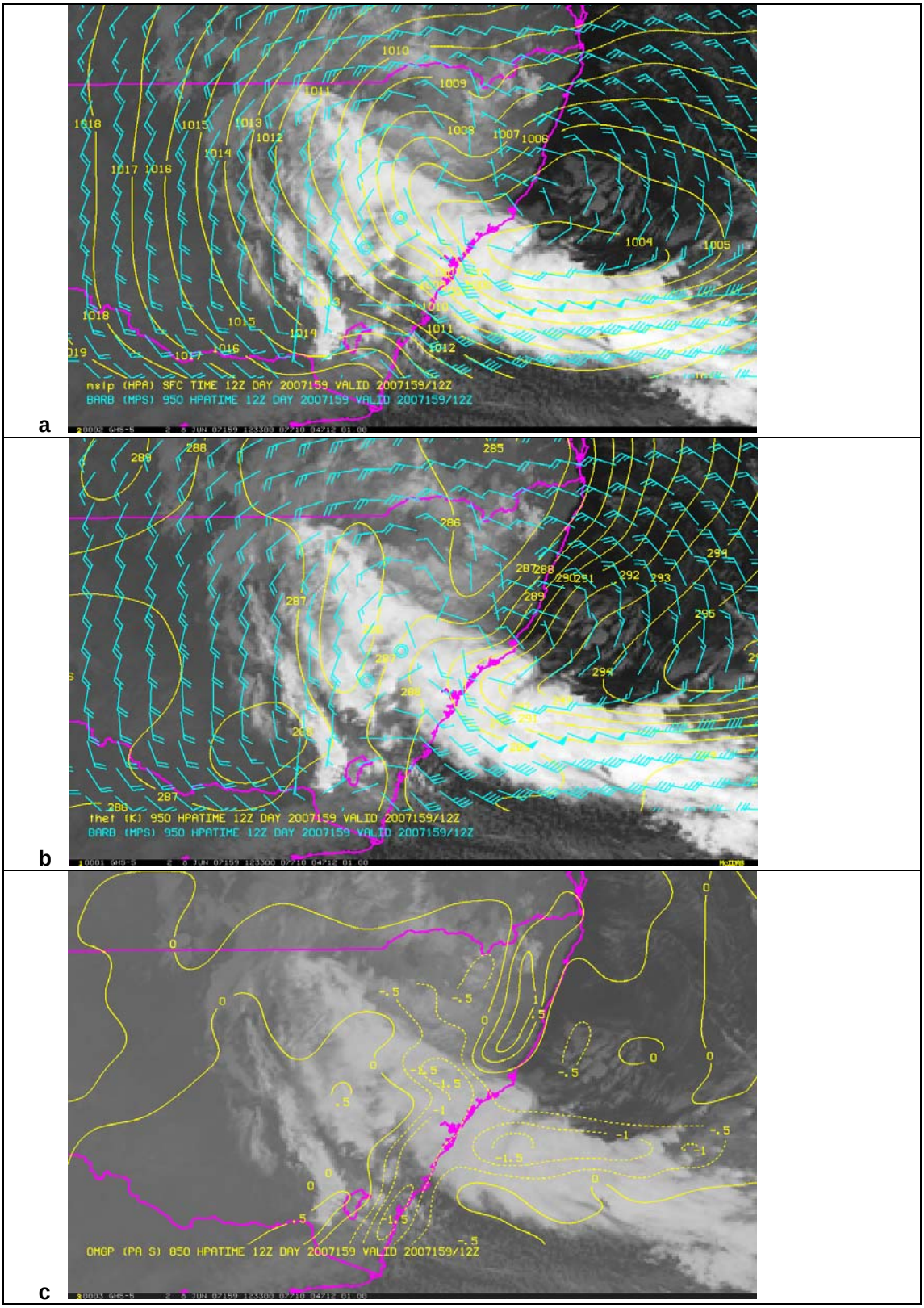

Fig. 23 LAPS analyses based at 1200 UTC 8 June 2007, each overlayed on the infra-red satellite image for the same time. Upper panel: MSLP and 950 hPa wind barbs. Middle panel: 950 hPa potential temperature and wind barbs. Lower panel: 850 hPa vertical motion field, with negative values (ascent) dashed.

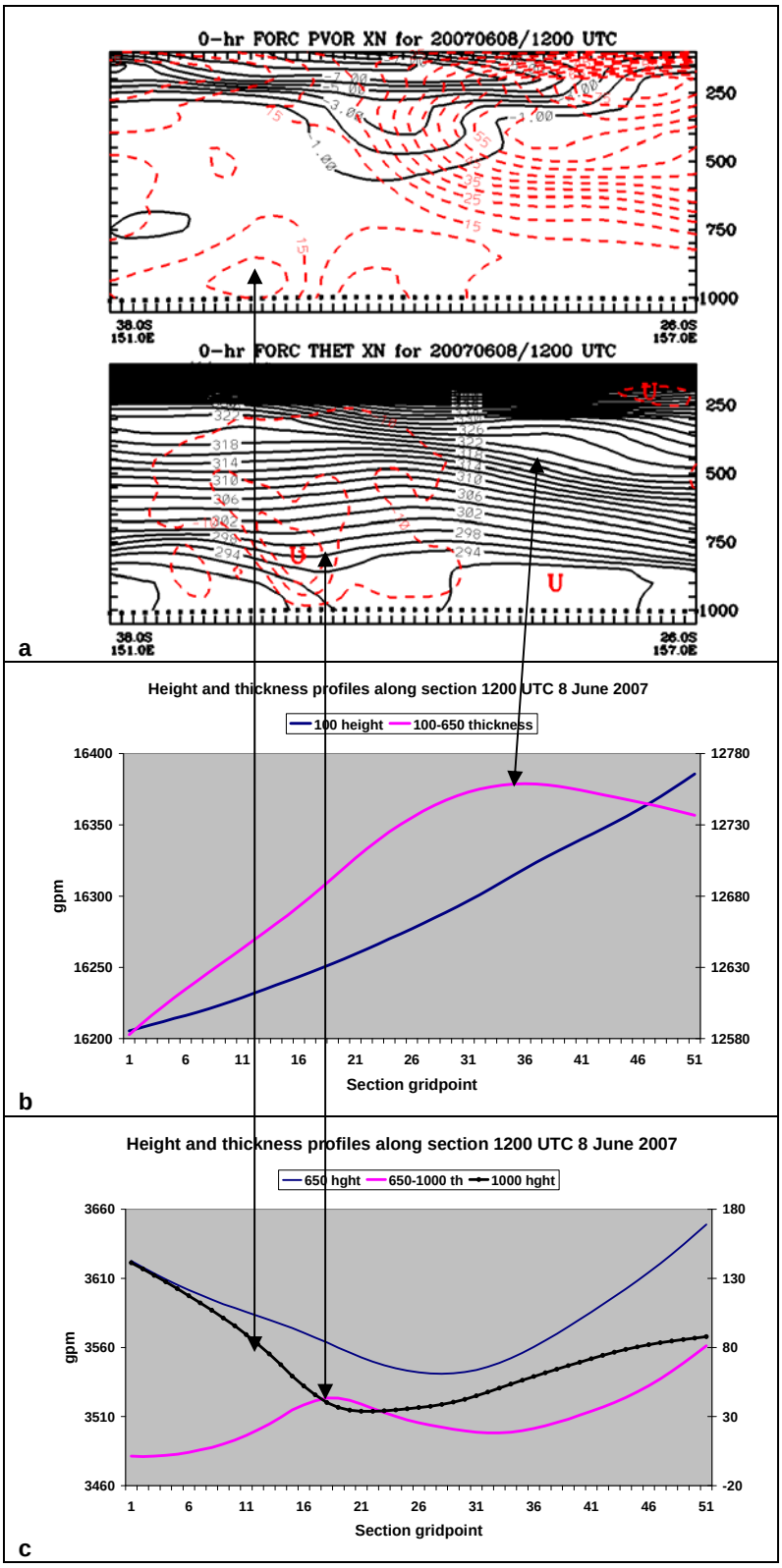

Fig. 24 LAPS analysis based at 1200 UTC 8 June 2007. Upper panel: vertical cross-sections of IPV (black) and wind speed (red, m s^{-1}) and of potential temperature (black) and vertical motion (red, hPa hr^{-1} negative values dashed). Middle panel: profiles of 100 hPa geopotential height (blue) and 100-650 hPa geopotential thickness (magenta). Lower panel: profiles of 650 hPa geopotential height (blue), 650-1000 hPa geopotential thickness (magenta), and 1000 hPa geopotential height (black).

6 THE CLOUDBAND FROM THE NORTH

The convective cloud mass that developed over and offshore of the northern NSW coastline was described in Section 3. As this moved southward it expanded (see Figs 8c, e) before merging with the main cloud/rainband that was impinging on the NSW coastline. As this cloud feature merged with the main cloudband radar imagery indicated there was a marked change in the convective nature of the rainfall (Fig. 9), and also in the observed rain rate (Fig 7). Prior to merger forecasters noted the development and southward movement of this cloud band, but were unsure about the processes that were driving it, and were thus unsure of the ramifications when it reached the main "frontal" cloudband, and thus how (or if) short-range forecasts should be amended.

Figure 25a-d shows 3-hourly sequences of 500 hPa vertical motion and of 300 hPa geopotential height/wind fields from the 0.05^{o} re-assimilated meso-LAPS hindcast simulation of the event. Both fields are overlaid on the infra-red satellite imagery, and with the model fields 1.5 hours ahead of the satellite imagery to best match the features with the satellite imagery sequence which begins at 2330 UTC 7 June 2007. This time offset is based on the premise that the model is providing a credible simulation of the event, but contains a small timing error. Another hypothesis might be that the model is correct, but that the clouds are responding to the ascent and so appear with some time lag. During the 9 hours shown the upper low moves southeastwards from northern NSW. There is a strong northwesterly jet on its eastern flank, and this jet splits into an anticyclonically curving branch into the Tasman Sea, and a cyclonic branch that curves south of the low and links to the southeasterly speed maximum southwest of the low centre.

While the vertical motion fields are highly structured, a consequence of the high model resolution and the very active precipitation processes occurring in the model, one east-west oriented ascent maximum is seen associated with the main precipitation band. This ascent maximum is clearly seen at 850 hPa (Fig. 23) in the LAPS analysis, and was shown in the cross-section in Fig. 24 to be associated with a front-like structure, although the front is essentially stationary. The northern cloud band is barely discernable at 2330 UTC, and then only with hindsight, but is clearly identifiable at 0230, 0530 and 0830 UTC in Fig. 25, and at these three latter times there is a clear and amplifying vertical ascent maximum associated with this cloud feature. After 0830 UTC the cloud features, and also the two vertical motion maxima, have essentially merged.

The northern vertical motion maximum can be conceptually understood in a variety of ways. Using IPV advection concepts (Hoskins et al. 1985), where ascent is forced by the differential advection of upper-level cyclonic IPV, it is clear from Fig. 11c,d that the northern ascent maximum is immediately downstream of the maximum in q-g forcing, and qualitatively also seen to be at the leading edge of the WV image dry area (also Fig. 11c,d) that has been associated with the IPV maximum. Griffiths et al. (2000) have discussed how such forcing of ascent can lead to convective destabilisation at the leading edge of an IPV maximum/dry slot.

An alternative conceptual model by which to interpret the forcing of the northern ascent maximum is the concept of jet exit circulations (Velden and Mills 1990). There is marked ageostrophic flow associated with the deceleration of the northwesterly jet, clearly indicated in the 300 hPa wind fields in the right-hand panels of Fig. 25, by the strong cross-contour orientation of the wind barbs in the circled areas above the developing cloud area and ascent

maximum. These wind vectors are directed from lower to higher geopotential heights, and thus the northern ascent maximum can be interpreted as the ascending branch of a transverse jet exit circulation. Either conceptual model can be used to "explain" the circulations leading to the development of the cloud mass over and off the northern NSW coastline during 8 June, but perhaps these two used in concert, combining as they do NWP model and remote sensing sources, would provide greater forecaster understanding and confidence.

As the southern ascent maximum was primarily associated with the lower-tropospheric thermal gradients, while the northern maximum was primarily associated with upper-tropospheric ageostrophic circulations / IPV advection, once the northern maximum moved southwards to overlay the southern ascent maximum a deep atmospheric circulation developed, which then had its feedback effects on the forecast precipitation. The net effect can be seen in the forecast rainfall forecast shown in Fig. 26. The upper panel shows the 24-hour forecast rainfall from the 0.05^{o} meso-LAPS hindcast, while the lower panel shows the cumulative and the hourly forecast rain-rate over a 0.75^{o}x1.0^{o} area (see rectangle) centred over Newcastle. The hourly rainfall rate increases after 0800 UTC, reaches a maximum at around 1200 UTC, and then decreases sharply after 1500 UTC. These transitions agree quite well with the qualitative interpretation of the satellite and radar imagery, and also with the forecaster impressions on the day.

While there is some qualitative agreement between these variations in rainfall amount simulated by the model and the observations presented earlier, there are sampling issues that should be addressed when making these assessments. The 72 and 24-hour totals in Figs 3 and 6 show the integrated result over a long period, while the individual station time-series (Figs 4, 5, 7) do not necessarily represent wide areas, particularly in highly convective rainfall events. Radar rainfall estimates provide another way of making space-time measurements of precipitation. Using reflectivity data from the Sydney and Newcastle radars, the STEPS system (Seed, 2005) was used to estimate hourly rainfall during the event, and histograms of hourly rainfall, and standard deviation of that rainfall, over the NWP box in Fig. 26 are shown in Fig. 27. While there are some unfortunate gaps in the radar data, these data show an increase in rain-rate around 0200 UTC 8 June, a decrease around 0500 UTC, and then a steady increase (allowing for the gap in the time-series) thereafter. After 1500 UTC there is a marked decrease in rainfall rate, and also its variance, indicating a transition to a more stratiform precipitation regime.

Figure 28 shows the spatial patterns of these STEPS rainfall estimates at three stages during this period, with, in the blank panel (Fig. 28a), the "rainfall box" shown. In the hour to 0200 UTC (Fig. 28b) there are quite wide areas of rainfall accumulation of some 10 mm hr^{-1} , with smaller areas > 20 mm hr^{-1}. The hourly accumulation 6 hours later, to 0800 UTC and during the phase of increased rainfall rate and increasing variance (Fig. 28c) shows a narrow focussing of an east-west zone of increased rainfall intensity over Newcastle. This band remained close to that position, with individual cells moving onshore, for at least 3 hours. Later again, in the hour to 1500 UTC (Fig. 28c) the "eye" can be seen in the rainfall accumulation, and the rain rate, while still significant, is more evenly distributed and without the centres of intense precipitation.

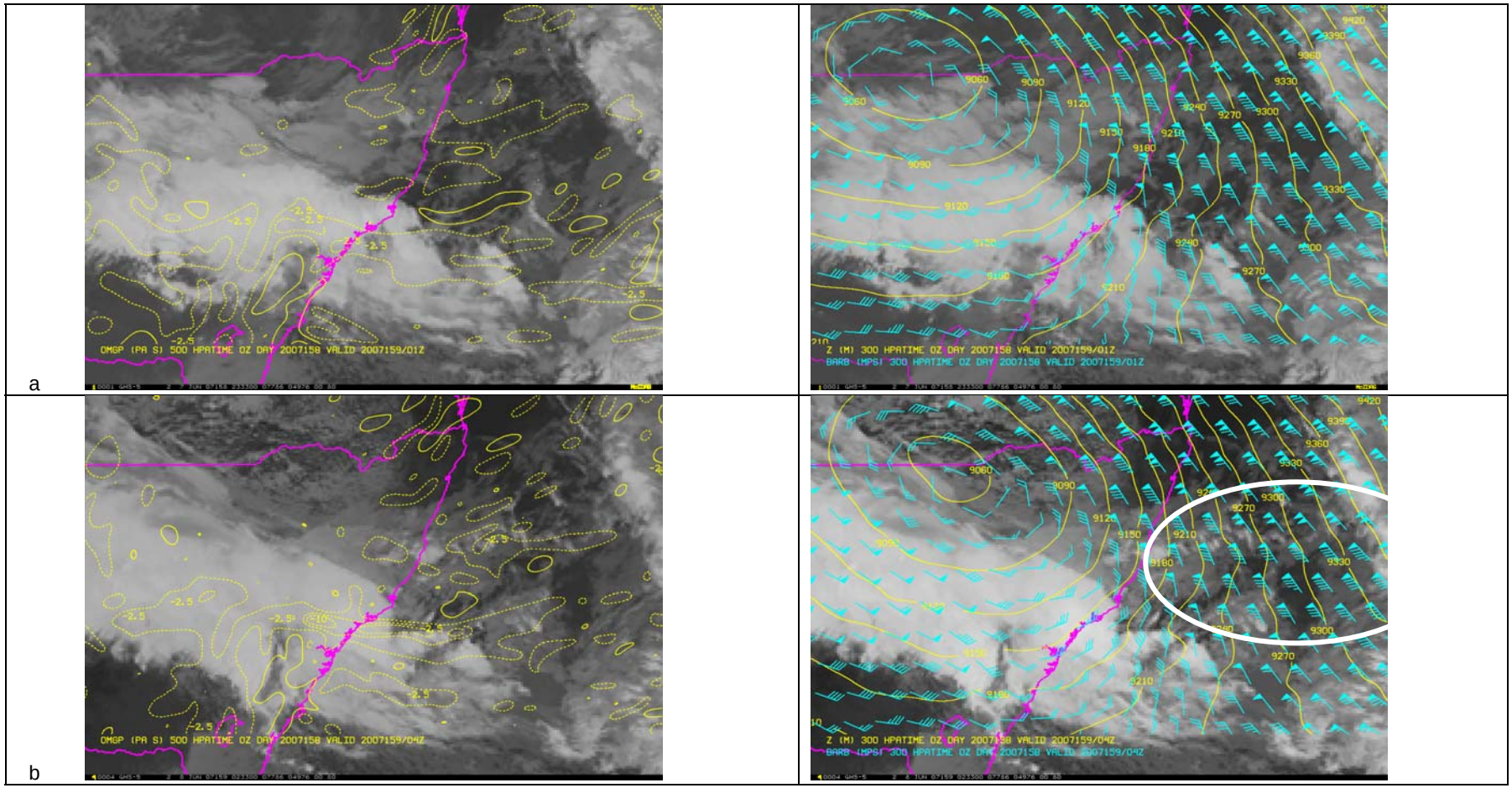

Fig. 25 a-b. Left panels show 500 hPa vertical motion (Pa s^{-1}, negative contours dashed) from the 0.05^{o} meso-LAPS hindcast. Right panels show 300 hPa geopotential height and wind fields. All panels overlaid on infra-red satellite imagery. Top row valid 0100 UTC, lower row valid 0400 UTC 8 June 2007.

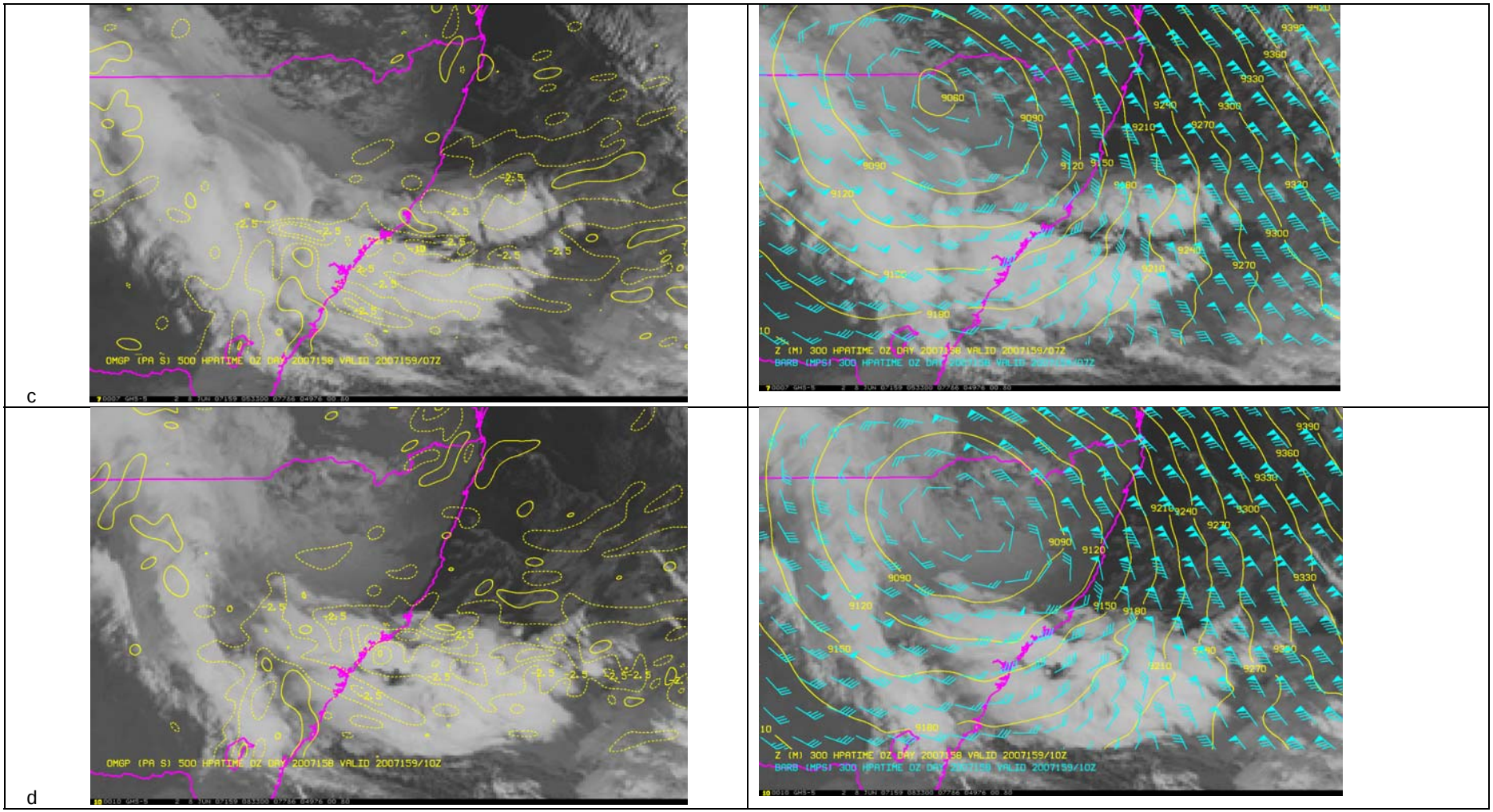

Fig. 25c-d. Left panels show 500 hPa vertical motion (Pa s^{-1}, negative contours dashed) from the 0.05^{o} meso-LAPS hindcast. Right panels show 300 hPa geopotential height and wind fields. All panels overlaid on infra-red satellite imagery. Top row valid 0700 UTC, lower row valid 1000 UTC 8 June 2007.

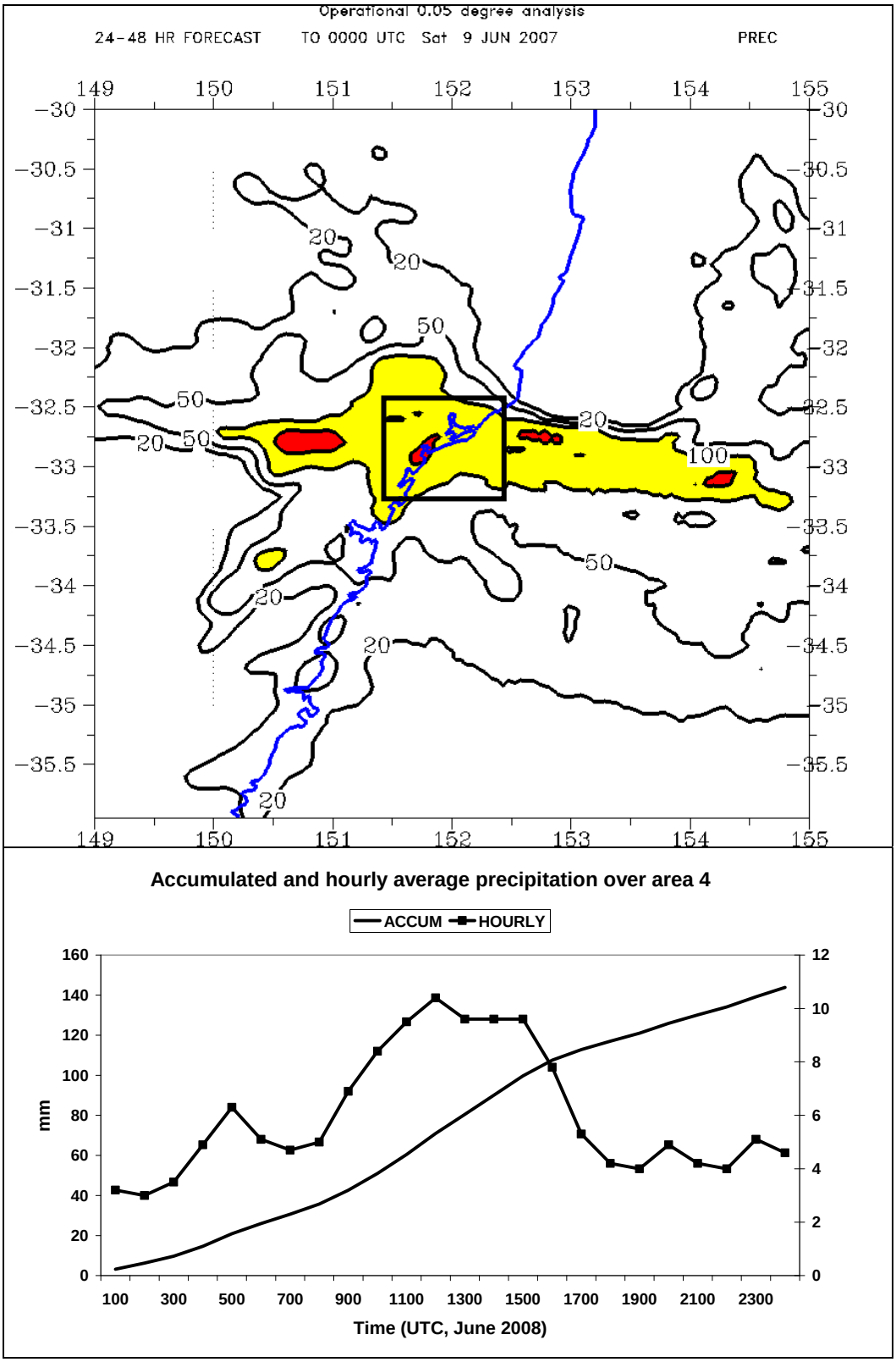

Fig. 26 Upper panel shows the 24-hour rainfall simulated by the 0.05° meso-LAPS hindcast. Isohyets are at 20, 50, 100, and 200 mm, with yellow and red shading for values above the latter two contour levels. In the lower panel the accumulated and hourly rainfalls from this model run, over the area from 33.25°S to 32.5°S, 151.5°E to 152.5°E (see box in upper panel) are shown. Nobbys Head is almost at centre of square.

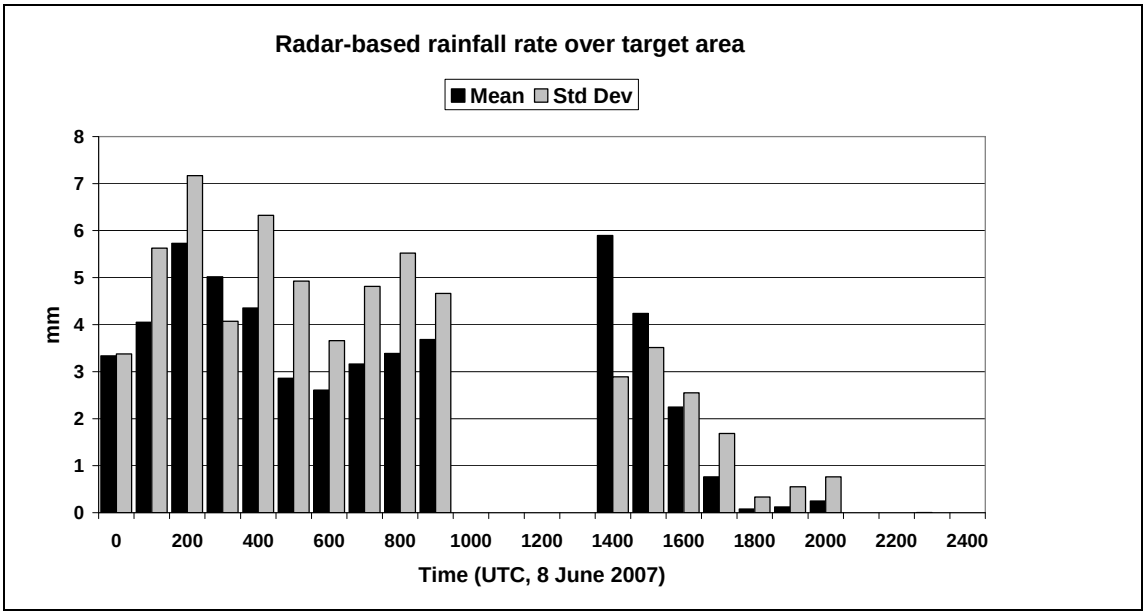

Fig. 27 Radar-derived estimates of hourly mean and standard deviation of rainfall over the sub-area shown in Fig. 26. Data is missing between 1000 and 1300 UTC.

While the effects of advection at the leading edge of the IPV maximum can lead to convective destabilisation, the fact that the IPV maximum is associated with depressed isentropes – that is, a warm anomaly – means that once the warm anomaly moves over the rainfall area there is a tendency to a stabilisation of the atmosphere. Thus after a period of increased convective activity, the movement of the IPV maximum over the rainfall area leads to a transition to a lower level of convective activity, and thus a lessening of rainfall rate, as is seen in the time series of rainfall observations in Figs 4 and 5, and qualitatively seen in the satellite and radar imagery as the cloud and precipitation patterns become more indicative of stratiform cloud/rainfall.

The NWP time series of simulated precipitation (Fig. 26) shows a remarkably close agreement to the radar estimates of integrated rainfall over the same period (Fig. 27). The model fields provide a narrative diagnosis that is consistent with independent (remotely sensed) observations and with the evolution of the observed rainfall over the Newcastle coastline on the evening of 8 June. This provides considerable support for the conclusions drawn from the diagnosess of presented in this report.

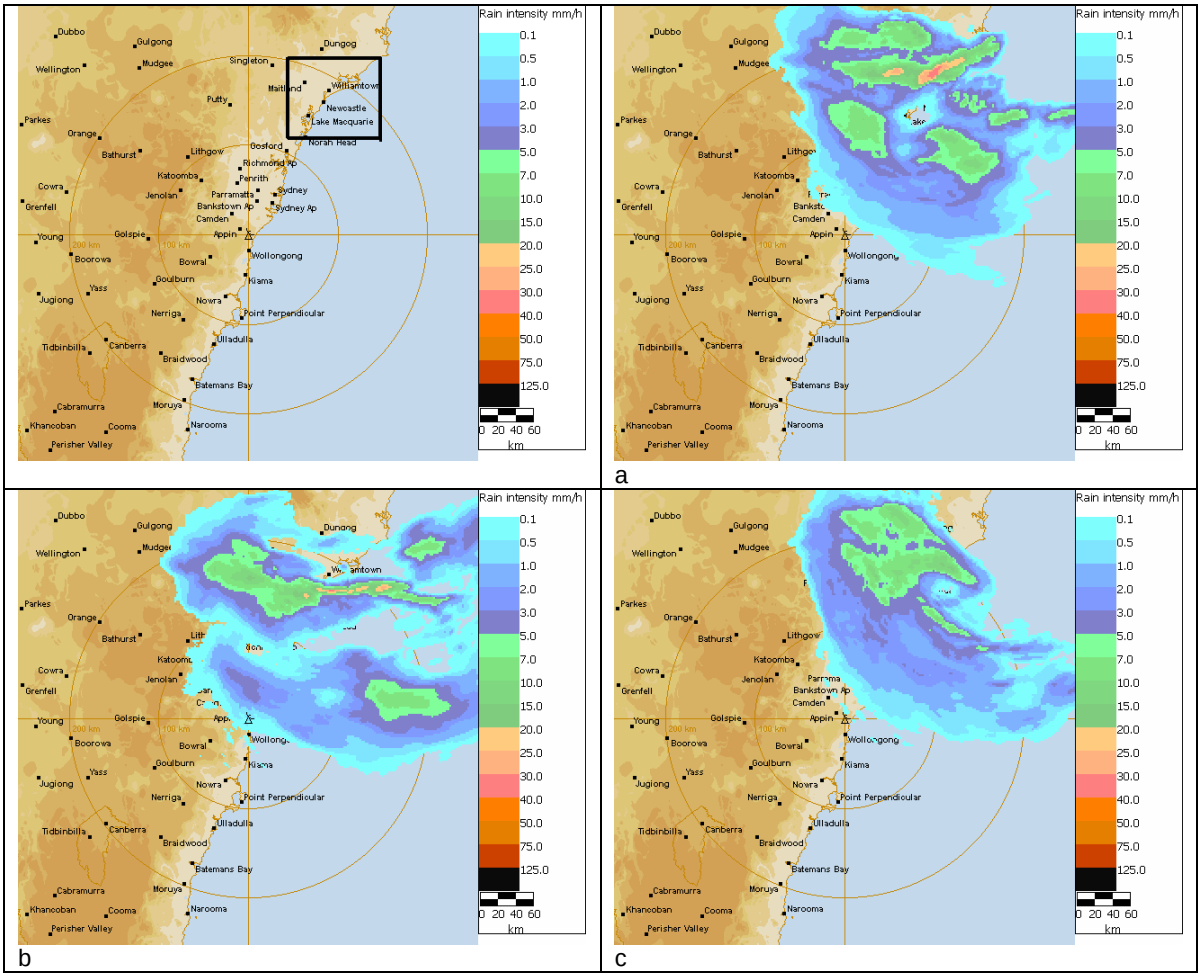

Fig. 28 Radar derived hourly rainfall fields (a) to 0200 UTC, (b) to 0800 UTC (c) to 1500 UTC 8 June 2007. The blank map in the upper left shows the area over which the statistics in Fig. 27 were calculated.

7 WAVES IN RADAR IMAGERY AND MESOSCALE NWP

The development of waves on the northern edge of the main rainband were quite spectacular in the radar imagery (Fig. 9), and were also evident in the satellite imagery (Fig. 8). These waves culminated in an apparently eye-like vortex crossing the Newcastle coastline at around 1500 UTC (Figs 9j,k) and a sharp pressure drop and recovery of some 5 hPa over a period of some 3 hours observed at Norah Head (Fig. 5h) and a slightly greater pressure fall and rise a little later at Williamtown (Fig. 5d).

The 0.05^o meso-LAPS MSLP/low-level wind hindcasts are shown at hourly intervals from 1200 UTC to 1900 UTC 8 June in the left-hand panels of Fig. 29. The two fascinating features of these forecasts are, first, the extraordinarily marked horizontal shear between the storm-force (and veering with time) band of southeasterly winds associated with the low-level jet/major rainband, and the lighter westerly winds near the low's centre, and second, the development of a series of small low centres that are simulated to form on the shear line and move northwestwards, sequentially crossing the coast near Newcastle. While the resolution of this model should not be expected to resolve the structures seen in the radar imagery, there does appear to be some indication that the model is capable at this resolution of at least hinting at the likelihood of a series of low pressure centres being generated along the shear line. These lows are also associated with some variations in wind speed, with an indication that local smaller-scale speed maxima within the low-level jet are associated with the southern or southwestern flanks of these secondary low centres. This is particularly well-marked in forecasts valid in the period around 1700 UTC (Figs 29e-g) when areas of greater than 50 kt winds are simulated southwest of the two simulated low centres that move onshore during that time.

The vertical structure of the strong shear line in these hindcasts is shown in Fig. 30. The important features here are the very strong cyclonic IPV column in the lower troposphere, co-located with the strong meridional wind shear on the northern flank of the low-level jet, and the ascent maximum in the lower troposphere associated with the baroclinic zone. This strong meridional gradient in wind shear on the northern flank of the low-level jet provides the necessary conditions for barotropic instability (Pedlosky 1987, page 575), and the series of modelled low-pressure systems, and the waves/vortices seen in the radar imagery are most probably a result of this instability, although given the rainfall rates, and the fact that the modelled atmosphere is not barotropic (see the cross-section in Fig. 30), other (convective, baroclinic) instabilities are also likely to be interacting during the development of these waves.

The the modelled variations in the flow field due to the development of these instabilities can be visualised more clearly using the Okubo-Weiss parameter (Okubo 1970, Weiss 1991) defined as

$$Q = S^2 - \zeta^2$$

which quantifies the respective magnitudes of the strain (S) and the relative vorticity ζ. Coherent meso-vortices survive in regions where relative vorticity dominates ($Q<0$), and fluctuations in convective activity, associated with variations in Q have been discussed in the tropical cyclone context by Rozoff (2006), Montgomery et al. (2006), and Wang (2008). The fields of Q diagnosed from the 0.05^o meso-LAPS hindcast are shown in the right-hand panels of Fig. 29, and a series of alternating positive and negative centres, organised along the shear line, is seen, and with some correspondence between major negative centres in Q and the secondary low pressure centres seen in the MSLP patterns in the left-hand column of that figure. There

appears to be some, albeit not complete, coherence of these positive and negative centres from hour to hour (see the lines joining centres in Fig. 29), with the centres propagating westwards at around 0.4-0.5 degrees of longitude per hour (~ 40 km hr^{-1}), which is of a similar order to the movement that can be inferred from the radar imagery in Fig. 6, given the image-to-image uncertainty in the "position" of a circulation centre.

A series of internally-nested simulations using the non-hydrostatic model, RAMS (Cotton et al. 1988), with a finest mesh of 1 km, showed in its finest (1 km grid) mesh simulation wave/vortex structures in the wind field and in the rainfall rates which show a very similar character to the radar imagery in Fig. 9. An example is shown in Fig. 31, where the 30-minute precipitation pattern shows a hook-shape (arrowed) that has very similar form to some of the radar images (e.g. Fig. 9g), and the wind field shows considerable degree of variation in speed along the northern flank of the strong wind band, and with the minima in wind speed associated with the stronger 30-minute precipitation centres. Further examples from this model run were presented by Abbs (2009).

It was argued in an earlier section that strong asymmetric wind flows on the southern side of these subtropical lows are a natural consequence of the life cycle of these cyclones, and that very strong wind shear on their northern side is also part of the normal structure of these lows. Thus it might be expected that instabilities, with accompanying rapid fluctuations in wind speed and direction and variations in rainfall rate and convective activity should also be expected on the northern edge of these cloud bands/low-level jets. Indeed, Bannister (2009) documents another example at Ballina (northern NSW) during a major east coast low in May 2009.

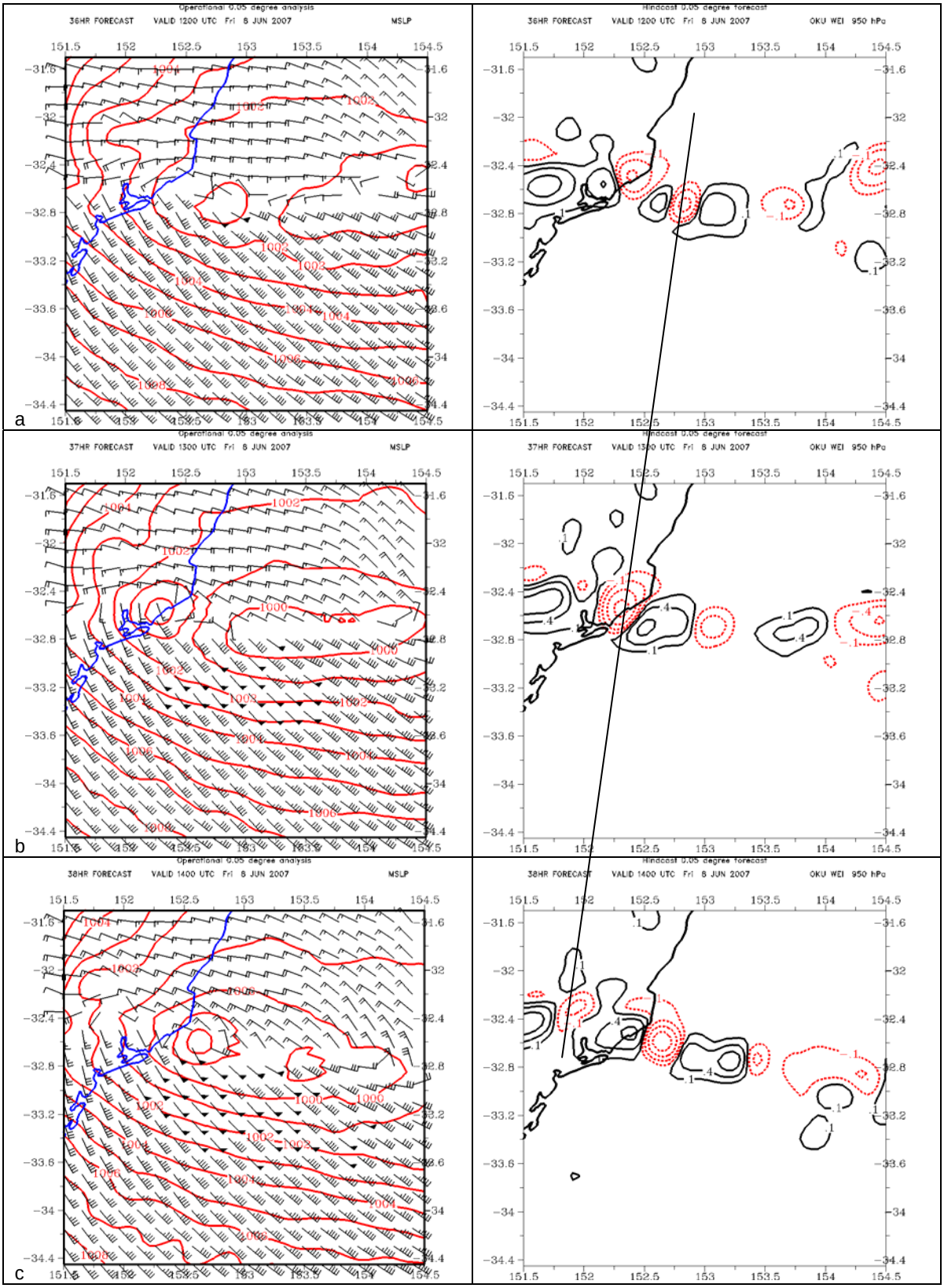

Fig. 29 a-c. Forecasts from the 0.05° meso-LAPS hindcast. Left column shows MSLP and low-level wind fields at 1200, 1300, and 1400 UTC 8 June 2007. Right panels show the Okubo-Weiss parameter (s^{-2} x 10^{-12}) at the same times, with the negative values red dashed. The line shows the westward propagation of an individual centre.

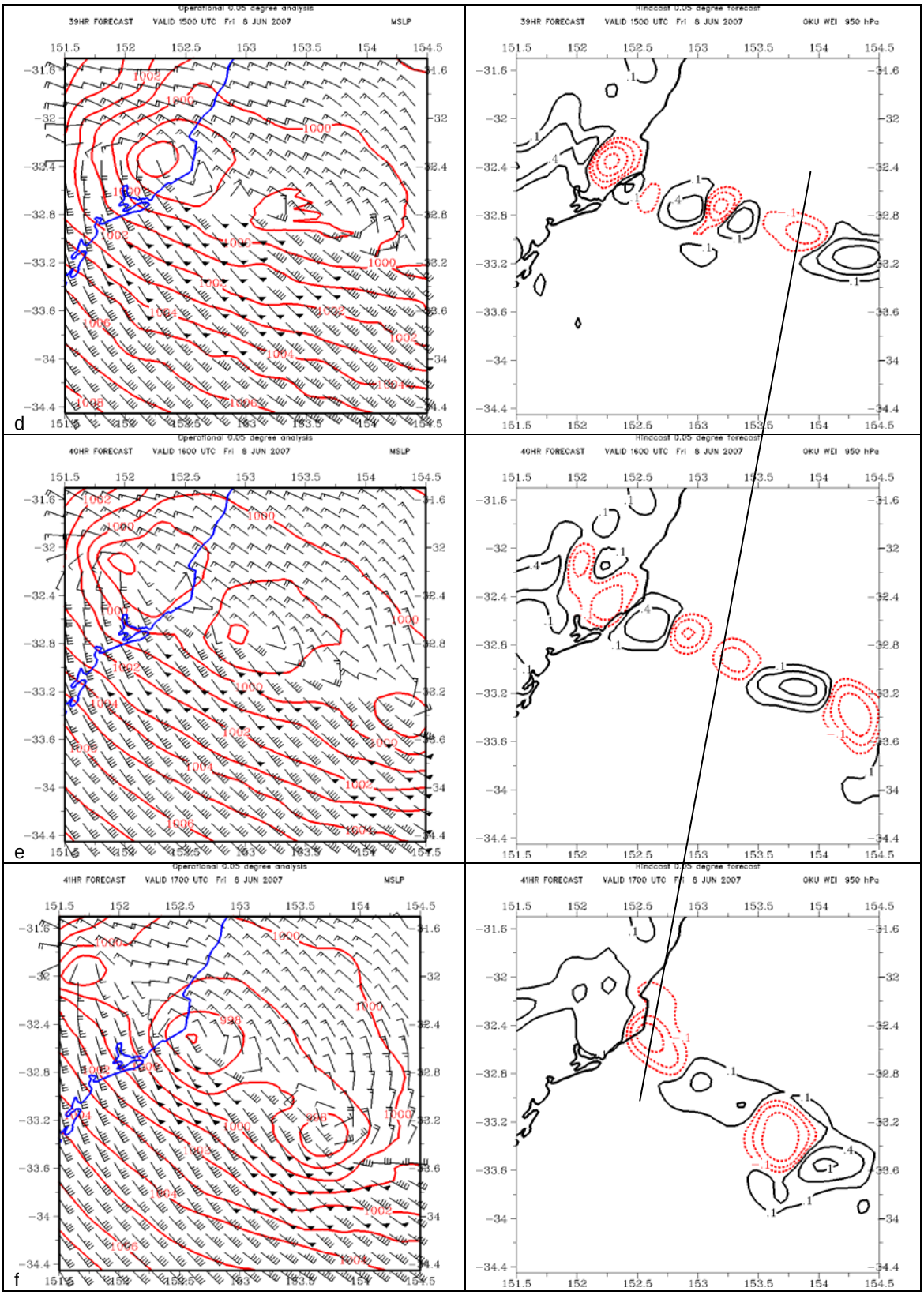

Fig. 29 d-f. Forecasts from the 0.05° meso-LAPS hindcast. Left column shows MSLP and low-level wind fields at 1500, 1600, and 1700 UTC 8 June 2007. Right panels show the Okubo-Weiss parameter (s^{-2} x 10^{-12}) at the same times, with the negative values red dashed. The line shows the westward propagation of an individual centre.

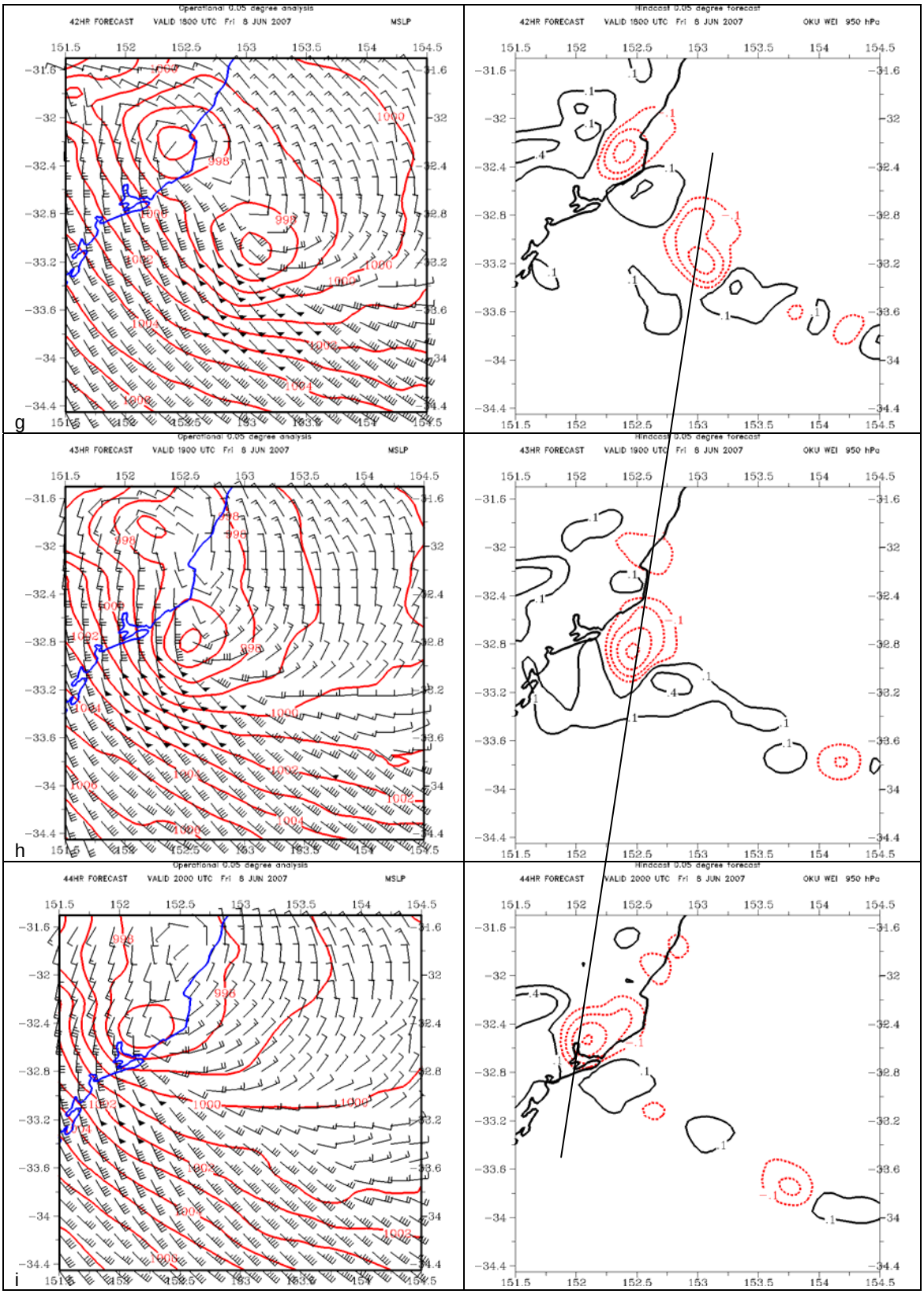

Fig. 29 g-i. Forecasts from the 0.05° meso-LAPS hindcast. Left column shows MSLP and low-level wind fields at 1800, 1900, and 2000 UTC 8 June 2007. Right panels show the Okubo-Weiss parameter (s^{-2} x 10^{-12}) at the same times, with the negative values red dashed. The line shows the westward propagation of an individual centre.

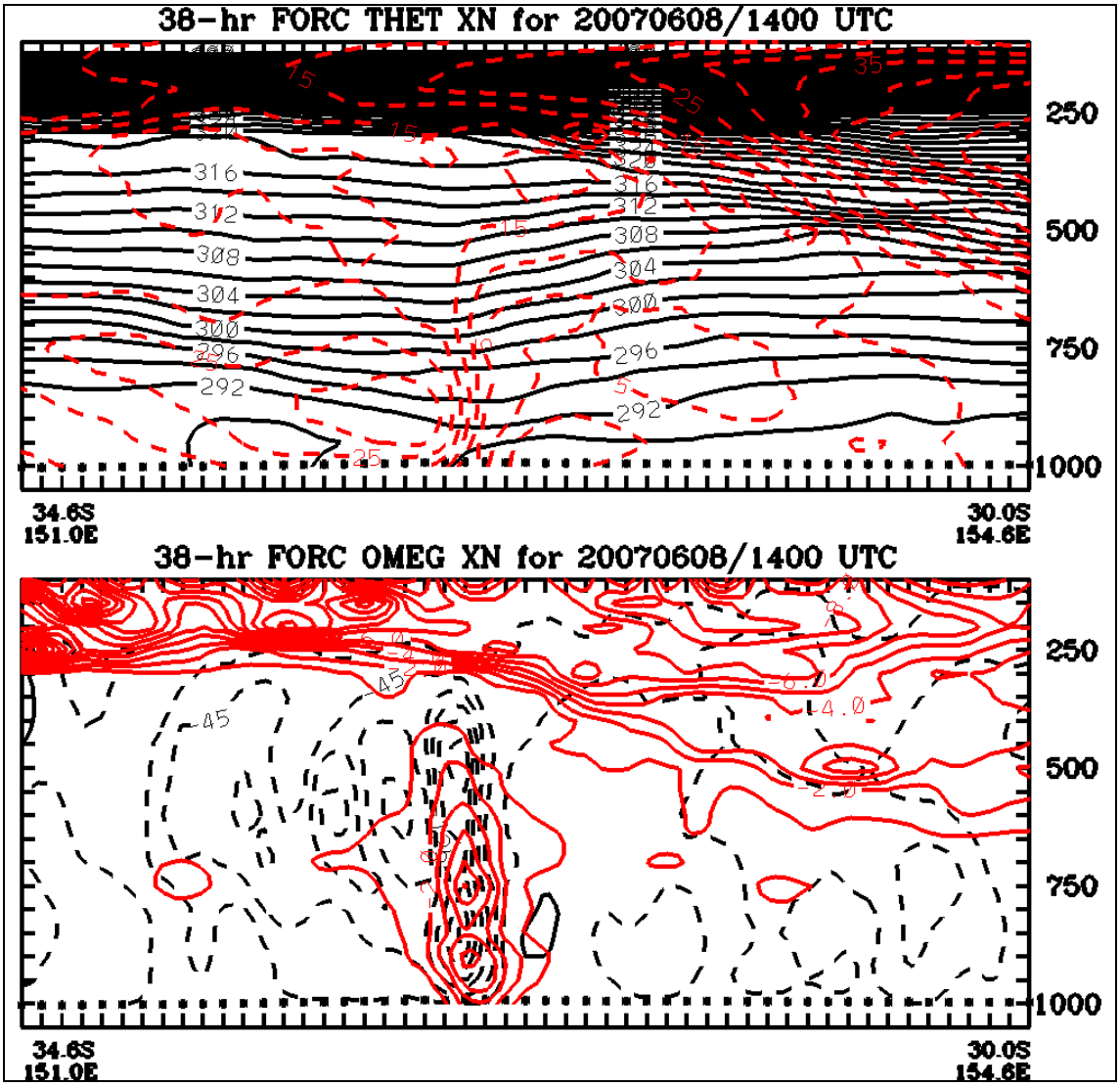

Fig. 30 Cross-section along a line roughly parallel to the NSW coastline, from the 0.05° meso-LAPS hindcast valid at 1400 UTC 8 June 2007. Upper panel shows the potential temperature (black) and wind speed (red, m s^{-1}). Lower section shows the IPV (red, IPV units) and vertical motion (black, hPa hr^{-1}) with ascent values dashed.

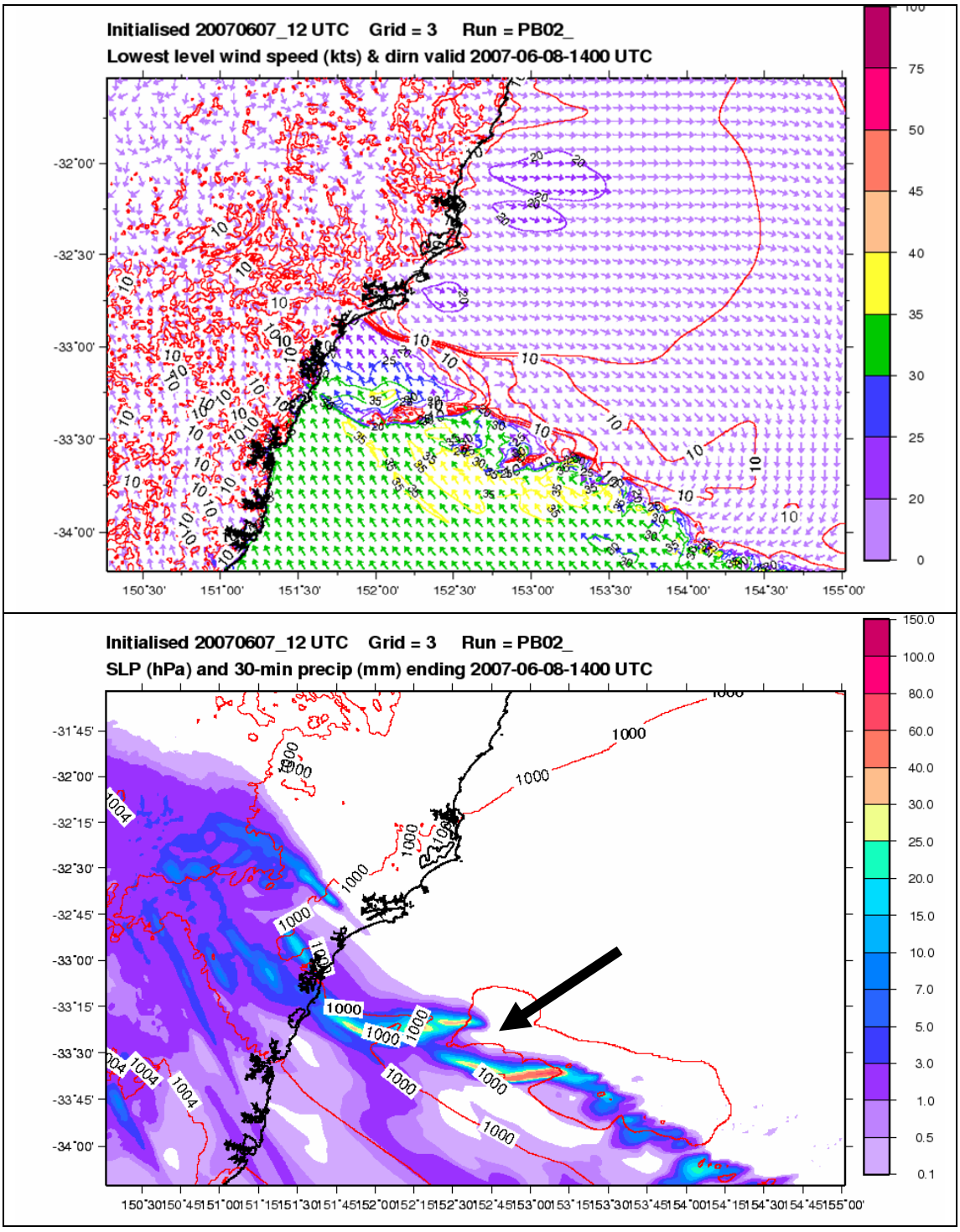

Fig. 31 Forecast valid at 1400 UTC 8 June 2007 from the 1km grid mesh RAMS simulation. Upper panel shows low-level wind vectors (colour coded for speed), while the lower panel shows 30-minute precipitation accumulation to 1400 UTC and the MSLP contours.

8 DISCUSSION

The Pasha Bulker east coast low developed primarily as a result of large-scale baroclinic forcing associated with hemispheric-scale Rossby wave amplification and downstream development. These processes are relatively well forecast by global medium range NWP models, and this event was well forecast several days in advance by these global models. However, at those ranges, and given the scale of the response and impacts, the use of ensembles is vital in defining those areas likely to be adversely affected by strong winds and heavy rainfall. As lead-times in the forecasts become less, it was shown that satellite WV channel imagery complements the NWP model forecasts of IPV, as has been widely discussed in many publications (e.g. Mansfield 1997), enhancing the conceptual understanding of any developing system.

It was shown that a number of other notable east coast lows were accompanied by similar precursor behaviour, and this suggests two complementary questions. First, do all east coast lows develop following the development of an upper cut-off low over eastern Australia? If not, what proportion do, and what is the particular structure and movement of those upper lows that do lead to explosive surface development? Second, do all cut-off lows over eastern Australia lead to east coast low development? These questions are being addressed in on-going research projects (Dowdy et al. 2010), but are dependent on the definition of an east coast low that is used. Certainly similar upper-level systems a little further west lead to many of the more significant rainfall events in the cropping areas of northwestern Victoria (Riseby et al. 2009) and have been associated with major flooding events over NSW (e.g. Mills and Russell 1992). While McInnes et al. (1992) differentiated between these two types of systems, it might be hypothesised that they are different only in the low-level response to similar upper forcing due to the differering lower-tropospheric static stabilities and surface temperatures over land and sea respectively. This hypothesis too is worthy of further investigation. Deeper understanding of these large-scale processes and their small-scale responses will have considerable application to climate change assessments of east coast low frequency and severity.

The near-surface structure of the mature Pasha Bulker storm was similar to that of the classic sub-tropical cyclone (Simpson 1952, Otkin and Martin 2004), with a strong (easterly) wind band on its southern side associated with the major rainband, and a weaker pressure gradient near the centre of the storm. This orientation means the strongest winds and rainfall are directed onshore, and with the orientation of the coastal orography, rainfall effects will be enhanced. It was further demonstrated that the way these subtropical lows develop a highly asymmetric thermal pattern means there is a low-level warm anomaly to the south of the circulation centre, and this has the effect of intensifying the low level jet to reach storm force strength. While this low-level warm anomaly might be interpreted as a “warm core”, it should not be interpreted as a warm core in the tropical cyclone context (Holland et al. 1987, McInnes et al. 1992), but rather as a warm core in the context of the Shapiro and Keyser (1990) warm seclusion. The net result is, though, that for these subtropical cyclone-like east coast lows, the normal wind structure is for the strongest winds (which may be of storm to hurricane force) to occur on the south or southwest side of the low, and at some distance from its centre.

There were considerable fluctuations in rain-rate and changes in convective morphology during the 12 hours of heaviest rainfall over Newcastle, and some of these changes were attributed first to deeper organised vertical circulations induced by the approaching IPV anomaly destabilising the atmospheric column, and then later due to stabilisation of the atmosphere as the tropopause

depression moved over the low-level cloudband. Again while each east coast low is likely to be different in detail, these processes are likely to be operating during some phases of the life cycles of many of these systems, and an understanding of them will likely lead to greater conceptual awareness during real-time operations.

The very strong cyclonic wind shear on the northern flank of the low-level jet provides a forecast challenge in that wind speeds may vary by >50 kt over a very short distance, and the users of forecasts should be aware of this, as well as the possibility that this transition zone may be moving along the coastline. As well, this cyclonic shear provides the necessary conditions for barotropic instability, and wave/vortex structures generated by these instabilities (probably compounded by baroclinic and convective processes) were seen clearly in the radar imagery, hinted at in the 0.05^{o} grid NWP hindcast and quite well resolved in the 1 km grid RAMS hindcast. Associated with these waves were marked fluctuations in rainfall rate, wind speed and direction, and negative pressure perturbations of some 3-5 hPa at coastal stations. Given that the same large scale environments are likely to exist in similar storms, again it is highly likely that such wave/vortex systems will form on the northern edge of similar cloudbands, and that forecasters and forecast users should be aware of this possibility. Such waves have also been documented on the northern NSW coastline for the May 2009 storm.

It is highly encouraging that NWP systems are capable of resolving so many of the features seen in this case study, ranging from the medium range hemispheric Rossby-wave scale down to 1 km grid spacing mesoscale NWP scales, and that these modelled circulations can be so closely related to remotely sensed cloud and reflectivity structures. As operational NWP systems develop, and resolutions increase, further improvements are likely to be realised.

9 ACKNOWLEDGMENTS

The enthusiasm of the Regional Director of the Bureau's NSW Regional Office, Barry Hanstrum, and his staff in encouraging the August 2008 workshop was an important impetus to this work, as were the contributions of all the workshop participants. Hunter Water are thanked for allowing us to present the data in Figures 6 and 7. Perry Wiles, Andrew Dowdy, and Tony Bannister are thanked for their thorough reviews of this report.

10 REFERENCES

Abbs, D. 2009. Modelling of convective events for climate change applications. Paper presented at the Third CAWCR Modelling Workshop – "Modelling and understanding high impact weather". Available at: http://www.cawcr.gov.au/events/modelling_workshops/workshop_2009/presentations/ABBS_2DEC.pdf .

Bannister, A. 2009. What is an event? Paper presented at "Beyond PML: Frequency vs severity" *Proceedings of a conference sponsored by Aon Benfield Australia Limited*.

Bell, G.D. and Keyser, D. 1993. Shear and curvature vorticity and potential vorticity interchanges: interpretation and application to a cut-off cyclone event. *Mon. Wea. Rev.* **121**, 76-102.

Bluestein, H.B. 1992. *Synoptic-Dynamic Meteorology in Midlatitudes*, V1. New York, Oxford University Press.

Bridgeman, H.A. 1986. The Sygna storm at Newcastle-12 years later. *Meteorol. Aust*., **3**(5), 10-16.

Cotton, W.R., Tremback, C.J. and Walko, R.L. 1988. CSU-RAMS – a cloud model goes regional. *Proc. NCAR Workshop on Limited-Area Modelling Intercomparison.* NCAR, Boulder, Colorado. Pp 202-11.

Davidson, N.E. and Weber, H.C. 2000. The BMRC High-Resolution Tropical Cyclone Prediction System: TC-LAPS. *Mon. Wea. Rev.*, **128**, 1245-65.

Dowdy, A.J., Mills, G.A. and Timbal, B. 2010. Diagnosing indicators of large-scale forcing of east coast cyclogenesis. *Proceedings, AMOS 2010 Conference*, Canberra, ACT. Australian Meteorological and Oceanographic Society.

Griffiths, M., Thorpe, A.J. and Browning, K.A. 2000. Convective destabilisation by a tropopause fold diagnosed using potential vorticity inversion. *Quart. J. Roy. Meteor. Soc.* **126**, 125-44.

Hirschberg, P.A. and Fritsch, J.M. 1991a. Tropopause undulations and the development of extratropical cyclones. Part I: overview and observations of a cyclone event. *Mon. Wea. Rev.* **119**, 496-517.

Hirschberg, P.A. and Fritsch, J.M. 1991b. Tropopause undulations and the development of extratropical cyclones. Part II: diagnostic analysis and conceptual model. *Mon. Wea. Rev.* **119**, 496-517.

Holland, G.J., Leslie, L.M. and. Lynch, A.H. 1987. Australian east-coast cyclones. Part I: synoptic overview and case study. *Mon. Wea. Rev*. **115**, 3024-36.

Hopkins, L.C. 1997. Australian east coast cyclones and potential vorticity interactions. PhD Thesis, Monash University, Melbourne, Australia. 170pp.

Hoskins, B.J., McIntyre, M.E. and Robertson, A.W. 1985. On the use and significance of isentropic potential vorticity maps. *Quart. J. Roy. Meteor. Soc.* **111**, 877-946.

Jones, D.A., Wang, W. and Fawcett, R. 2009. High quality spatial climate data-sets for Australia. *Aust. Meteor. Mag.* **58**, 233-48.

Kallberg, P., Berrisford, P., Hoskins, B. et al., 2005. ERA-40 Atlas, *ERA-40 Project Report Series*, No. 19. European Centre for Medium Range Weather Forecasting.

McInnes, K.L., Leslie, L.M. and McBride, J.L. 1992. Numerical simulation of cut-off lows on the Australian east coast: sensitivity to sea surface temperature. *Int. J. Climatol.* **12**, 783-95.

Mansfield, D.A. 1997. The use of PV and WV imagery to validate NWP. *Meteorol. Appl*. **4**, 305-9.

Mills, G.A. and Russell, I. 1992. The April 1990 floods over eastern Australia : synoptic description and assessment of regional NWP guidance. *Wea. and Forecasting.* **7**, 636-68.

Mills, G.A. 2001. Mesoscale cyclogenesis in reversed shear – the 1998 Sydney-Hobart yacht race storm. *Aust. Meteor. Mag.* **50**, 29-52.

Montgomery, M.T., Nicholls, M.E., Cram, T.A. and Saunders, A.B. 2006. A vortical hot tower route to tropical cyclogenesis. *J.Atmos. Sci*. **63**, 355-86.

Okubo, A. 1970. Horizontal dispersion of floatable particles in the vicinity of velocity singularity such as convergences. *Deep Sea Res*., **17**, 445-54.

Otkin, J.A. and Martin, J.E. 2004. A synoptic climatology of the subtropical Kona storm. *Mon. Wea. Rev*. **132**, 1502-17.

Pedlosky, J. 1987. *Geophysical Fluid Dynamics,* Second Edition. Springer-Verlag, New York. 710pp.

Puri, K., Dietachmayer, G.D., Mills, G.A., Davidson, N.E., Logan, L. and Bowen, R. 1998. The new BMRC limited area prediction system, LAPS, *Aust. Meteor. Mag.*, **47**, 203 – 23.

Riseby, J.S., Pook, M.J., McIntosh, P.C., Ummenhofer, C. and Meyers, G. 2009. Characteristics and variability of synoptic features associated with cool season rainfall in southeastern Australia. *Int. J. Climatol.* **29**, 1595-613.

Rozoff, C.M., Schubert, W.H. and McNoldy, B.D. 2006. Rapid filamentation zones in intense tropical cyclones. *J.Atmos. Sci*. **63**, 355-86.

Schultz, D.M., Keyser, D. and Bosart, L.F. 1998. The effect of large-scale flow on low-level frontal structure and evolution in mid-latitude cyclones. *Mon. Wea. Rev.* **126**, 1767-91.

Seed, A. 2005. STEPS: an empirical treatment of forecast uncertainty. *BMRC Research Report No 111*, A.J. Hollis, Ed. Pp 131-7.

Shapiro, M.A. and Gronas, S. 1999. The life cycles of extratropical cyclones. *American Meteorological Society*, Boston, Mass. 359pp.

Shapiro, M.A. and Keyser, D. 1990. Fronts, jet streams and the tropopause. *Extratropical Cyclones.* The Erik Palmen Memorial Volume, C.W. Newton and E.O. Holopainen, Eds. *American Meteorological Society*, 167-91.

Simpson, R.H. 1952. Evolution of the Kona storm a subtropical cyclone. *J. Atmos. Sci.*, **9**, 24-35.

Velden, C.S. and Mills, G.A. 1990. Diagnosis of upper-level processes influencing an unusually intense extra-tropical cyclone over southeast Australia. *Wea. and Forecasting* **5**, 449-82.

Vincent, C.L., Bourke, W., Kepert, J.D., Chattopadhyay, M., Ma, Y., Steinle, P.J. and Tingwell, C.W. 2008. Verification of a high resolution NWP system. *Aust. Meteor. Mag.* **57**, 213-33.

Wang, Y. 2008. Rapid filamentation zone in a numerically simulated tropical cyclone. *J. Atmos. Sci.* **65**, 1158-81.

Weiss, J. 1991. The dynamics of enstrophy transfer in two dimensional hydrodynamics. *Physica D*, **48**, 273-94.

Weldon, R.B. and Holmes, S.J. 1991. Water vapour imagery. Interpretation and applications to weather analysis and forecasting. *NOAA Technical Report NESDIS 57*. 213pp.

The Centre for Australian Weather and Climate Research is a partnership between CSIRO and the Bureau of Meteorology.